Theoretische Physik

Phase Transitions from Bose-Einstein Condensates to Active Soft Matter Systems

Inaugural-Dissertation
zur Erlangung des Doktorgrades
der Naturwissenschaften im Fachbereich Physik
der Mathematisch-Naturwissenschaftlichen Fakutlät
der Universität Münster

2024

Vorgelegt von
Alina Barbara Steinberg
aus Bochum

institut für
theoretische physik

Dekan: Prof. Dr. R. Bratschitsch
Erstbetreuer: Prof. Dr. U. Thiele
Zweitgutachter: Prof. Dr. F. Maucher
Abgabedatum: 28. Oktober 2024

Kurzzusammenfassung

Ziel dieser Arbeit ist es, den Zusammenhang zwischen lokalisierten Zuständen und Phasenübergängen in einer Vielzahl unterschiedlicher physikalischer Systeme zu verstehen, die von passiv zu aktiv und von der klassischen bis hin zur Quantenebene reichen.

Zu diesem Zweck werden zum einen verschiedene Näherungen eines Modells der klassischen Dichtefunktionaltheorie, dem GEM-4-Modell, betrachtet, mit dem Ziel, das Snakingverhalten von Ästen lokalisierter Zustände zu testen. Dabei stellt sich heraus, dass dieses normalerweise weder Teil des Originalsystems, noch der besseren Näherungen ist, sondern nur auftritt, wenn quadratischen und kubischen Termen andere als die natürlich resultierenden Gewichte zugewiesen werden.

Für den aktiven Fall liegt der Fokus auf Phasengrenzen in einem erweiterten aktiven Phasenfeldkristallmodell. Die Arbeit kommt zu dem Schluss, dass kristalline Lösungen des passiven Grenzfalls, die durch das Hinzufügen einer konstanten Aktivität zerstört werden, durch das Hinzufügen einer dichteabhängigen Aktivität wieder hergestellt werden können. Darüber hinaus werden die Existenz und das Verhalten rotierender Kristalle und Zustände fernab des kritischen Punktes beschrieben.

Auf der Quantenebene wird ein Bose-Einstein-Kondensat auf die generelle Existenz lokalisierter Zustände getestet. Sie erscheinen ohne Snaking sowohl in einem Rydberg Testmodell mit lokaler und nichtlokaler Wechselwirkung, als auch in einem dipolaren Modell mit Röhrengeometrie in einer und drei Dimensionen. Insbesondere zeigt diese Arbeit die Möglichkeit, dass einige zuvor aufgrund der Primärbifurkation als zweiter Ordnung eingestufte Phasenübergänge durch die Existenz lokalisierter Zustände als Phasenübergänge erster Ordnung klassifiziert werden müssen.

Abstract

This thesis seeks to understand the relation between localized states and phase transitions in a variety of physical systems ranging from passive to active and from classical to quantum level.

To that end different approximations of a classical density functional theory model, the GEM-4 model, are examined with the aim of testing for snaking behavior in branches of localized states. This reveals that snaking is not usually a part of either the original system, or the better matching approximations, but rather appears once quadratic and cubic terms are given weights other than the naturally resulting ones.

For the active case the focus is on phase boundaries in an extended active phase-field crystal model. The thesis concludes that adding a density-dependent activity can reverse the destruction of patterned states occurring in the passive limit, which happens under the influence of a constant activity. In addition, the existence and behavior of rotating crystallites and states far from the critical point are detailed.

On the quantum level a Bose-Einstein condensate is tested for the general existence of localized states. They appear without snaking in both a Rydberg-dressed toy model with local and nonlocal interactions, as well as in a dipolar model with tube geometry in both one and three dimensions. Specifically, this thesis shows the possibility that some phase transitions previously identified as second order on account of the primary bifurcation have to be classified as first order due to the existence of localized states.

Contents

1 **Introduction** **1**

2 **Pattern Formation and Phase Transitions** **5**
- 2.1 Theoretical Preliminaries 5
- 2.2 Phase Coexistence and Maxwell Construction 11
- 2.3 Classical Nucleation Theory 12
- 2.4 Localized States and Coexistence at Finite Size 16
- 2.5 Numerical Analysis of Nonlinear Partial Differential Equations . . . 18

3 **Soft Matter Physics** **25**
- 3.1 Introduction to Soft Matter Physics and Models 25
- 3.2 The DDFT Model with GEM-4 Potential 27
- 3.3 DDFT Approximations and the PFC Model 31
- 3.4 Bifurcation Analysis and Localized State Behavior 33
- 3.5 Comparison to Classical Nucleation Theory 41

4 **Localized States in an Active Model** **46**
- 4.1 Motility-Induced Phenomena in Active Soft Matter Models 46
- 4.2 The Extended Active PFC Model 47
- 4.3 Bifurcations in One Dimension 53
- 4.4 Rotating Localized States in Two Dimensions 58

5 **Bose-Einstein Condensation** **63**
- 5.1 Bose-Einstein Condensation with Interactions 63
- 5.2 Phases, Transitions and Linear Stability 67
- 5.3 Hydrodynamic Formulation for Steady State Solutions 70
- 5.4 Simplified Nonlocal Model and its Local Approximations 72
- 5.5 Simplified Model with Higher-Order Nonlinearities 84
- 5.6 Dipolar BECs in an Infinite Tube 96

6 **Conclusion and Outlook** **104**

A **Appendix** **108**
- A.1 Spatial Stability and the Prediction of Localized States 108
- A.2 Rescaling of the DDFT Equation with GEM-4 Potential 114

A.3 GEM-4 Results in One Spatial Dimension 115
A.4 Localized State Interface in the PFC-γ Approximation 116
A.5 Stability of Localized States in the Nonlocal BEC 116

Bibliography **119**

1 Introduction

Any equilibrium system in nature seeks to reach a resting point with minimum energy. This expresses itself, e.g., in the commonly found states of water: fluid, solid and vapor, which differ in some inherent property such as the density. Disturbing a system, e.g., by raising the temperature, can push it from one state to another in a so-called phase transition (Ch. 2) [70, 132]. Of specific interest to this thesis are phase transitions towards non-uniform phases and states, e.g., crystallization.

Such phases and states also appear in non-equilibrium systems, where the interaction of individual microscopic parts can lead to self-organization into a macroscopic structure. The underlying driving force can be, e.g., physical, chemical, social or economical in nature [70, 51, 184, 74, 102, 88]. Often the resulting structure is a pattern, meaning the same elements reappear repeatedly, e.g., in form of stripes. Self-organization appears all throughout the cosmos on vastly different length scales (e.g., cells, galaxies) and time scales (e.g., laser pulses, heart beats, certain biorhythms) [70, 130, 192]. Some prominent examples are the patterns on animals [184, 87], swarming behavior [145] and weather phenomena [84]. Fig. 1.1 depicts more specific cases of these examples: a) dot pattern on a cheetah b) circular swarming behavior in a school of fish and c) stripe pattern in cirrocumulus undulatus clouds.

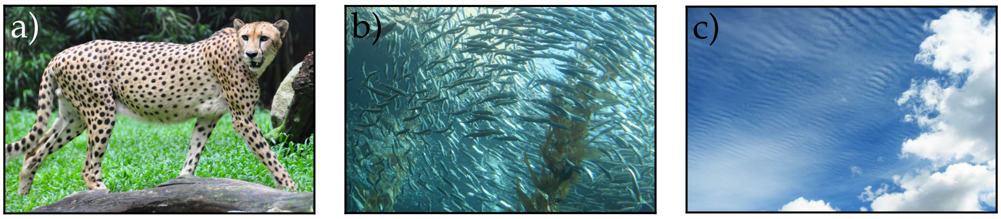

Fig. 1.1: Examples of self-organized structures: (a) dot pattern on a cheetah, cropped from [69] with permission, (b) circular swarming behavior in a school of fish, cropped from [127] with permission and (c) stripe pattern in cirrocumulus undulatus clouds, cropped from [163] with permission.

This thesis focuses specifically on systems where particle interactions are longranged or non-local and can be described by convolutions. To facilitate numerical simulations, approximations are often used to derive simpler partial differential equations from the original integro-differential equations.

In this thesis phase transitions are explored with a specific interest in a state which frequently accompanies it, the so-called localized state. In such a state a patterned phase and another (often uniform) phase exist simultaneously in the same domain, only separated by an interface region. Some examples of this can be found in Fig. 1.2, namely a) a localized seven peak structure in a ferrofluid, b) sunspots and c) localized patches of vegetation.

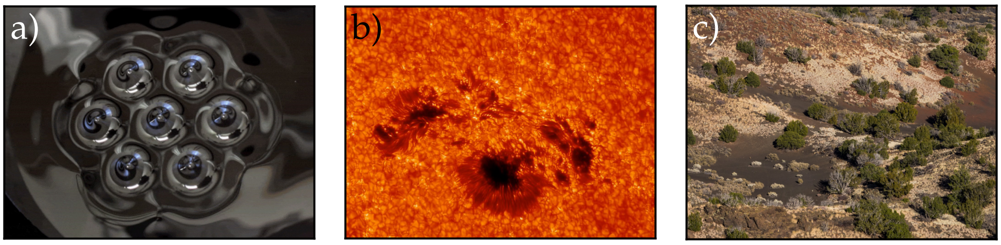

Fig. 1.2: Examples of localized states: (a) localized seven peak structure in a ferrofluid, cropped from [110] with permission, (b) sunspots, cropped from [129] with permission, (c) localized patches of vegetation, cropped from [42] with permission.

The emergence and behavior of localized states, as well as general information on phase transitions are examined for three different types of systems.

The first system is categorized as part of classical passive soft matter physics (see Ch. 3), which deal with materials with a large, nonlinear response to small stimuli. Examples include easily deformed polymer structures such as rubber, the soft properties of colloids such as paints or the optical properties of liquid crystals, easily influenced by electric fields [46]. The physical understanding of many of these effects is based on Brownian motion and consequently closely connected to statistical mechanics [198], but the actual concept of soft matter is built on the studies of de Gennes and Edwards in the 1960s and 70s, which united several fields of study into soft materials [198, 62]. From there the field spread in many different directions, though this thesis specifically focuses on colloidal systems, described by dynamical density functional theory, developed in 1999, which uses a density field to describe particle positions [119, 11].

In addition to the passive case, this thesis also takes a look into a higher order active soft matter model (Ch. 4). Matter is considered active if its constituents can absorb energy and convert it into motion [63, 118, 145]. Consequently, those types of systems are open to energy influx and do not move towards equilibrium states. Instead, the constituents may form a variety of potentially moving patterns, examples of which include clusters and swarms, such as in bacteria colonies or flocks of birds, and also extends to artificial self-propelled constituents [145]. Early interest in the topic was closely connected to the concept of life and consequently rather philosophical in nature [93, 145]. The renewed interest in the 1980s was still directed at the collective behavior of living beings [139], but self-driven particles [187], computer simulation [155] and physical models [183] soon followed. The modern use of the term active matter has only been used since 2006 [145, 153].

The last system considered in this thesis is quantum mechanical in nature. Specifically, this thesis looks at transitions between phases which are macroscopic manifestations of quantum effects (Ch. 5). One such phase is the superfluid, a state of matter which distinguishes itself through dissipationless flow in the liquid phase, most famously found in liquid Helium [91, 3, 111]. Another phase, the supersolid, (i.e., a state of matter which is both superfluid while simultaneously exhibiting the rigid structuring of a solid) was predicted to exist starting in the late 50s [68, 7, 103, 37]. While this state of matter could not (yet) be found for Helium [96], it has been realized in Bose-Einstein condensates (BECs) [26, 39, 177].

A BEC is a new state of matter and short hand for a dilute gas (4-6 orders of magnitude below air [141]) of massive bosons at very low temperatures (μ-nK [6, 44]), where a macroscopic amount of particles occupies the lowest-energy single-particle state [48]. The theory of BECs dates back to 1925 [25, 48], but experimental proof in form of an atomic BEC is as young as 1995 [6, 44] and owes its existence to advances in laser cooling, combined with magnetic traps and evaporative cooling (see, e.g., Ref. [126]). Those early BECs show superfluidity, but no supersolid phase. The latter was realized experimentally in 2017 by two groups using additional light fields [105, 106].

This thesis is structured as follows: Ch. 2 gives an overview over terminology surrounding patterns, phase transitions and bifurcation theory. It explains linear stability analysis, as well as particular features of phase transitions, i.e., nucleation and its connection to localized states. Finally, it details the numerical methods used to simulate results.

Ch. 3 introduces a soft matter system, the GEM-4 model, and proceeds to analyze the effects of different approximations on the existence and behavior of localized states.

Ch. 4 analyzes the effects of adding different types of activity to an extended phase-field crystal model, specifically on the different phase boundaries, and takes a look at the emergence of localized states in form of rotating crystallites, which includes two and three phase coexistence far from the critical point.

Ch. 5 is focused exclusively on the transition from superfluid to density modulated states such as supersolids, specifically the existence and stability of localized states as defined above. The chapter analyzes the transition for two different types of Bose-Einstein condensates: First, a Rydberg-dressed toy model both with and without approximation and second, a dipolar Bose-Einstein condensate with tubular geometry, both under dimensional reduction and in a full three-dimensional set-up. The former is treated with a full bifurcation analysis. A special focus is laid on whether localized states exist as a ground state and how higher-order nonlinearities affect the phase transition. The latter, as a more realistic set-up, is largely tested for the general existence of localized states.

Finally, Ch. 6 summarizes the results and gives an outlook for possible future research avenues for all systems.

2 Pattern Formation and Phase Transitions

2.1 Theoretical Preliminaries

This thesis focuses on self-organized patterns, which are spatio-temporal structures with recurring elements, found in complex systems consisting of many nonlinearly interacting often microscopic parts. Those parts collectively form the macroscopic pattern, which is not immediately apparent when looking at the forces governing the individual parts. The pattern is therefore self-organized, rather than imposed externally through the driving force [70, 88].

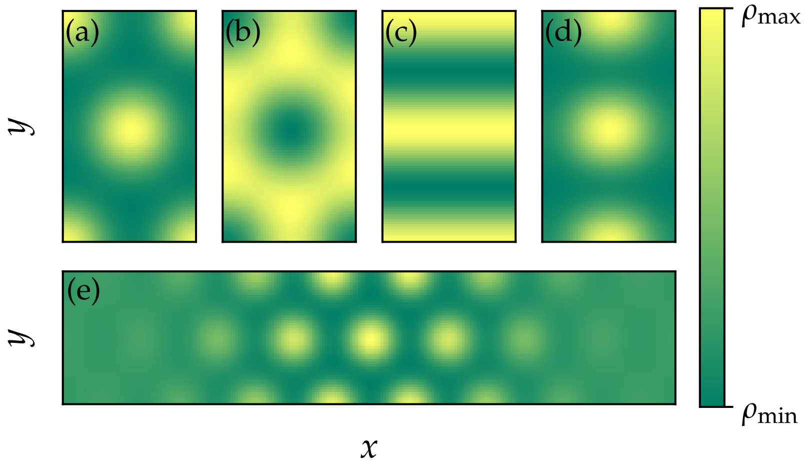

Fig. 2.1: Examples of common patterns in two-dimensional, spatially periodic systems: (a) hexagon, (b) honeycomb or down-hexagon, (c) stripe (d) rectangle and (e) localized state (see Sec. 2.4). The colors mark low or high values of an order parameter ρ and the domain sizes are (a)-(d) $2L_c/\sqrt{3} \times 2L_c$ and (e) $16L_c/\sqrt{3} \times 2L_c$ where L_c is the critical length scale of the pattern.

Here, the focus is placed on spatially extended patterns, which can take a variety of forms. Some of the more common two-dimensional patterns are depicted in Fig. 2.1 with the most prominent ones, hexagons, down-hexagons and stripes [85] shown in panels a), b) and c), respectively. The colors mark low or high values of a local density. The overall pattern is measured by an order parameter, a property of the system which changes with the appearance of the pattern (e.g., an amplitude) [88, 132].

A phase is a state of matter in which the macroscopic physical properties of the substance are uniform when considered over a macroscopic length scale (e.g., unit cell size for patterns). It depends on system specific macroscopic parameters such as the temperature [132]. In terms of patterns this means the whole domain is spanned by the same pattern.

A diagram which details the existing phases, spanned by those macroscopic parameters is called a phase diagram. Boundaries between phases are called phase boundaries and crossing them by changing parameters can lead to a phase transition. Such a transition can be detected by measuring an order parameter, as the materials characteristics change drastically. From a mathematical point of view a phase transition is characterized by the appearance of a singularity (e.g., a cusp, jump or divergence) in a physical quantity of the material [132].

Phase transitions can generally be divided into different categories. In this thesis there appear only continuous and discontinuous transitions with respect to the order parameter, which roughly correspond to second and first order transitions according to Ehrenfest's classification [113, 4].

To analyze complex systems with respect to phases and transitions between them it is useful to express them in form of an evolution equation. While more complicated equations are possible, a simple dynamical equation is sufficient to explain general principles:

$$\partial_t \mathbf{u} = \mathbf{G}(\mathbf{u})\,. \tag{2.1}$$

Here $\mathbf{u} = \mathbf{u}(t)$ is a state variable at time t. ∂_t represents an operator for partial temporal derivation, while $\mathbf{G}$ is a function of $\mathbf{u}$ [131].

The phase space of the system contains all possible states the system can reach in accordance with Eq. (2.1) starting from any possible initial condition $\mathbf{u}_0 = \mathbf{u}(t = 0)$. Solutions take the form of a flow $\phi(\mathbf{u}_0, t) = \mathbf{u}(t)$, which is a path, or more formally a trajectory through phase space depending entirely on the initial condition [85, 173].

Trajectories are unique outside of invariant manifolds, which include fixed points, i.e., states $\mathbf{u}_f(t) = \mathbf{u}_f$ for which $\partial_t \mathbf{u}_f = \mathbf{G}(\mathbf{u}_f) = 0$. Hence, there is no flow as $\phi(\mathbf{u}_f, t) = \mathbf{u}_f$. Another invariant manifold is the periodic orbit, a temporally reoccurring equivalent of the fixed point. It describes a trajectory in phase space which meets itself after a period T, i.e., for any state $\mathbf{u}_p$ on the periodic orbit it is $\phi(\mathbf{u}_p(t)) = \phi(\mathbf{u}_p(t+T))$. Equivalents for higher dimensions also exist [85, 173].

The temporal dynamics of a system is governed by those invariant manifolds and whether phase space trajectories move towards or away from them. If all trajectories in the immediate surroundings move towards the invariant manifold it is considered stable, if the reverse is true it is unstable. In case trajectories move both towards and away it is considered a saddle node [85].

Mathematically speaking, linear stability is determined by adding a perturbation to a fixed point

$$\mathbf{u} = \mathbf{u}_f + \delta\mathbf{u} \tag{2.2}$$

and inserting it into the governing equation (2.1). The resulting equation can then be linearized around $\mathbf{u}_f$. This leads to:

$$\partial_t \delta\mathbf{u} = \mathbf{G}(\mathbf{u}_f) + \delta\mathbf{u}\,\underline{\mathbf{J}}(\mathbf{u}_f) + \mathcal{O}(\delta\mathbf{u}^2)\,, \tag{2.3}$$

where $\underline{\mathbf{J}}$ represents the Jacobian matrix, with elements $J_{ij} = \partial G_i/\partial u_j$ where $u_j \in \mathbf{u}$. As $\mathbf{G}(\mathbf{u}_f) = 0$, Eq. (2.3) becomes a linear equation which can be solved by an exponential ansatz $\propto e^{\sigma t}$. The exponent, i.e., the eigenvalues σ of the Jacobian matrix, decide whether the perturbation shrinks or grows in time.

Here, stable directions of trajectories touching a fixed point are indicated by negative real parts of the eigenvalue σ, while positive real parts mark unstable directions. Imaginary parts are indicative of additional circular motion of the flow around the fixed point. Overall only fixed points with negative real parts for all their eigenvalues are considered stable [85].

A change in the stability and number of invariant manifolds in response to the change of parameters λ is called a bifurcation, with the exact bifurcation point given by λ_c. A bifurcation diagram details those changes by tracking those invariant manifolds in the form of branches in parameter space [85, 173, 166].

There are different ways of characterizing bifurcations. Local bifurcations only affect the flow directly around an invariant manifold, while global bifurcations affect the whole phase space. The codimension gives the number of parameters in λ which need to be varied in order to reach a bifurcation point[1]. Finally, stationary bifurcations appear when only real eigenvalues cross zero, as opposed to a dynamic bifurcation where the crossing eigenvalues are imaginary [85, 166].

---

[1] The codimension is determined here with regards to the normal form. Unfolding would of course lead to more parameters and the given definitions would therefore only hold under certain symmetries.

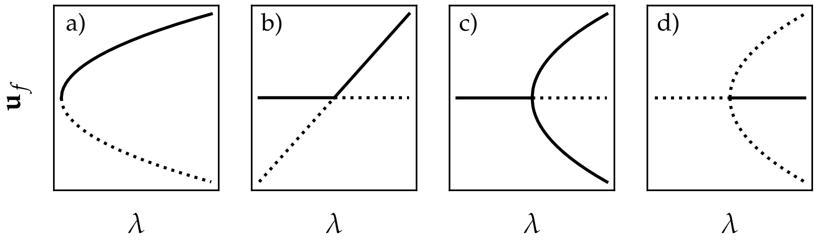

Fig. 2.2: Bifurcation diagrams which track fixed points $\mathbf{u}_f$ with respect to changes in parameter λ. a) fold (or saddle-node), b) transcritical, c) supercritical pitchfork and d) subcritical pitchfork, respectively. Solid lines represent stable solutions, while dotted lines represent unstable fixed points.

The bifurcations depicted in Fig. 2.2 are not an exhaustive list, but rather form reference points for bifurcations appearing in this thesis. Fig. 2.2 a) depicts a saddle-node or fold bifurcation, which is characterized through the collision and subsequent annihilation of two fixed points of opposite stability when moving towards smaller λ. It is a local codimension one bifurcation [173, 85].

Fig. 2.2 b) shows a transcritical bifurcation, which is also characterized through a meeting of a stable and unstable fixed point, but here they exchange their respective stability rather than annihilate. Again it is a local codimension one bifurcation [173, 85].

Fig. 2.2 c) and d) show super- and subcritical pitchfork bifurcations, respectively, which are common in (but not exclusive to) systems with symmetries such as left-right symmetry, i.e., where fixed points appear in pairs as no solution is more favorable than the other. With the emergence of new fixed points the original fixed point changes stability. If the change is from stable to unstable with the additional fixed points being stable it is a supercritical pitchfork. If the opposite is true it is a subcritical pitchfork. Both are steady and local codimension-one bifurcations [173, 85].

Another example of a bifurcation is the Hopf bifurcation (not shown). It resembles the pitchfork, but rather than two distinct fixed points, what emerges is a periodic orbit, rendering it a dynamic codimension-one bifurcation. It can can be sub- or supercritical, too [4, 166].

Some combination of bifurcations in a system may lead to parameter regions with multiple stable fixed points, called multistable regions. Depending on external conditions, the system may assume any stable solution and even jump between them. In an equilibrium system the solution with the lowest energy is both linearly and nonlinearly stable, while other stable solutions are metastable [173, 4].

Phase boundaries come in different forms depending on the underlying thermodynamic ensemble. Fig. 2.3 shows examples in a) the grand canonical (open to energy and particle exchange) and b) the canonical ensemble (open to energy exchange) for a phase boundary related to two uniform phases of different densities.

The phase diagram for the grand canonical ensemble is shown in the (T, μ)-plane with temperature T and chemical potential μ. The phase boundary is given by a black line, which ends in the critical point (black dot). Above the critical point the phases become indistinguishable, therefore no boundary exists.

The transition between two uniform phases in the canonical ensemble looks quite different. It is depicted in the (T, ρ)-plane, with temperature T and density ρ. Rather than a clearly defined boundary, there are several regions separating the two uniform phases below the critical point. The spinodal (solid line) is also called a linear stability boundary and is where the uniform phases become linearly unstable in favor of the phase-separated state. The binodals (dashed line) signal the onset of a multistable region, typically indicated by a saddle-node bifurcation. Spinodals and binodals are not limited to bordering phase-separated states, but may also appear for transitions towards patterns [46].

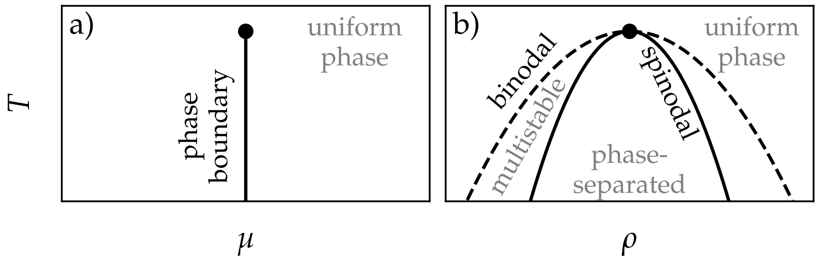

Fig. 2.3: Sketch of a phase diagram with phase boundaries in a) the grand canonical ensemble and b) the canonical ensemble, depicted in the (T, μ) and (T, ρ)-plane respectively. The former shows a simple phase boundary (black solid line), ending in the critical point (black dot). The latter shows both a spinodal (solid line) and a binodal (dashed line), meeting in the critical point. The spinodal is the border of linear stability between the uniform and phase-separated states. The binodal borders a region where both phase-separated and the respective uniform phase appear.

In terms of phase transitions any bifurcation (or combination of different bifurcations) which causes a multistable region is part of a first order transition. As these are accompanied by a binodal, any transition which passes a binodal before reaching the spinodal is of first order.

A naive assumption would be that one would find only the most energetically favorable solutions in an experiment. In reality finite size effects or having a limited time of observation means metastable or even unstable states may become important, e.g., as transient states [181].

In a non-equilibrium system with changing energy levels a solution will not come to rest in a free energy minimum, but change between possible states within the scope of the current level of energy (cf. Ch. 4).

For spatio-temporal systems Eq. (2.1) becomes a partial differential equation with field $\mathbf{u} = \mathbf{u}(\mathbf{x}, t)$, which now also depends on position $\mathbf{x}$, and operator $\mathbf{G}$. The latter contains spatial derivatives in the form of powers of the nabla operator ∇. The stability of a system becomes more complicated, as the perturbation $\delta\mathbf{u}$ needs to account for spatial patterns.

If an exact solution of the system is known, as is usually the case for uniform solutions (i.e., $\mathbf{u}_f(\mathbf{x}) = \bar{\mathbf{u}} = \text{const}$ with mean value $\bar{\mathbf{u}}$) linear stability can be determined by adding a small periodic perturbation, which takes the form of an exponential function:

$$\delta\mathbf{u} = \varepsilon e^{i\mathbf{k}\mathbf{x}+\sigma t}\,, \tag{2.4}$$

Here $\mathbf{k}$ is a wave vector while ε is a smallness parameter, so that $\delta\mathbf{u} \ll \bar{\mathbf{u}}$. Inserting the perturbation into the governing equation gives a dispersion relation of the form

$$\sigma(\mathbf{k}) = f(\mathbf{k}) + \mathcal{O}(\varepsilon)\,. \tag{2.5}$$

In this thesis only dispersion relations with $f(k)$ appear, i.e., σ has radial symmetry as it only depends on the absolute value k of the wave vector $\mathbf{k}$. The simplest example for f would be a polynomial in k^2.

Negative values of $\mathrm{Re}(\sigma)$ cause the perturbation to decrease with t, while positive values represent a growing perturbation. Hence, $\mathrm{Re}(\sigma) = 0$ represents the border of linear stability for the uniform ground state. This coincides with a maximum of $\mathrm{Re}(\sigma)$ with respect to k.

Depending on the form of σ there are different types of instabilities. For conserved dynamics as considered in this thesis $\mathrm{Re}(\sigma)(k = 0) = 0$ always applies. Furthermore passive systems show purely real σ, meaning the dispersion relation represents only the growth rate. Active systems (cf. Ch. 4) also show complex values of σ, which correspond to oscillations.

If $\mathrm{Im}(\sigma) = 0$, a maximum in $\mathrm{Re}(\sigma)$ growing next to $k = 0$ constitutes a large-scale (also long-wave), or Cahn-Hilliard instability [60]. A minimal example of such a dispersion relation would require powers of k^2 up to $\mathcal{O}(k^4)$.

If for $\mathrm{Im}(\sigma) = 0$ a maximum crosses zero at a critical wavenumber $k = k_c > 0$ this constitutes a small-scale (also short-wave) or conserved-Turing instability, leading to pattern formation with a length scale of $L_c = 2\pi/k_c$ [60]. A minimal example of such a dispersion relation would require powers of k^2 up to $\mathcal{O}(k^6)$.

If $\mathrm{Re}(\sigma) > 0$ and $\mathrm{Im}(\sigma) \neq 0$ the instability becomes oscillatory. The large-scale case is named conserved-Hopf instability, while the small-scale equivalent is called conserved-wave instability [60].

At any maximum with $\sigma = 0$, $\partial_k \sigma = 0$ also holds. Together the two equations allow for the determination of the critical wave vector k_c as well as critical model specific parameter values [85, 131, 70].

Alternatively, it is possible to test for spatial stability, i.e, add a purely spatial perturbation, where different types of eigenvalues correspond to different types of patterns. Explanations and applications of this can be found in App. A.1.

2.2 Phase Coexistence and Maxwell Construction

In layperson terms, phase coexistence can happen, when two phases A and B are equally favorable to the system, leading to both being present in the same domain, only separated by an interface. The Maxwell construction [31] gives a more formal explanation: The point of coexistence is characterized by two stable states, which have equal chemical potential μ and pressure p. As $p = -\Omega/V$, this is equivalent to equal grand potential Ω.[2]

Fig. 2.4 a) and b) show the Maxwell construction, specifically an isothermal (red) for phase A (dashed) and phase B (dotted) as well as meta- and unstable states (dash-dotted). Panel b) visualizes the process explained above (with equal μ and p), while panel a) shows the traditional explanation in the (p, V)-plane. Here the black dots represent the coexistence points, chosen such that areas a_1 and a_2 (shaded red), bordered by the isobar (black, solid line), are of equal size. Those same coexistence points are also marked in panel b) and c). The latter shows the double tangent construction, which is applied for a canonical ensemble, where the corresponding potential is the free energy F, while particle number N and therefore density ρ (rather than μ) are fixed. The coexistence points are defined by a shared tangent connecting two minimum regions as the new lowest energy states. This is equivalent to the equal μ and equal Ω construction in the grand canonical ensemble, where the density is variable.

---

[2] It is $\Omega = U - TS - \mu N$ and $U = TS - pV + \mu N$, therefore $\Omega = -pV$.

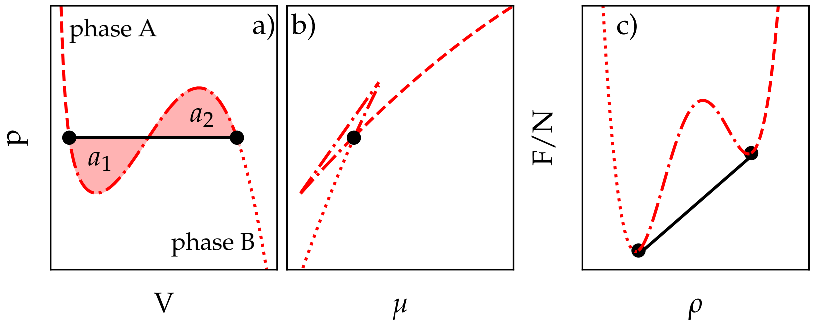

Fig. 2.4: Maxwell construction [31] for two uniform phases A (red dashed line) and B (red dotted line). Panel a) shows the traditional presentation of an isothermal line (red) in the $p - V$ plane, where shaded areas a_1 and a_2 are of equal size, therefore defining the coexistence points (black dots) connected by an isobar (black line). Panel b) shows the equal p and equal μ part of the coexistence, while panel c) depicts its equivalent for the canonical ensemble, the double-tangent construction.

2.3 Classical Nucleation Theory

When a system is pushed far enough into a binodal region (i.e., the region bounded by binodal and spinodal) to become metastable, a phase transition occurs. However, unlike when the phase becomes unstable, the new phase does not form everywhere at once. Instead, there is a gradual change, starting with an initial patch of the new phase, which then spreads across the domain. This phenomenon can be described by classical nucleation theory (CNT) [136, 137, 92]. It describes how systems in metastable states pass over a free energy barrier to reach the thermodynamically stable state (e.g., crystallization of a supercooled liquid). Besides impurities sparking the transition between phases, the system has to form a sufficient amount of the stable phase, the so-called critical nucleus, to be able to move from one state to the other. The reason such a nucleus has to reach a certain volume is due to the interface appearing between the two now separated phases. On the one hand the additional energy of the interface raises the overall energy, on the other hand having more of the energetically favorable new phase lowers it. The critical nucleus is reached when these energy gains and losses are equal.

In a container plus reservoir which fixes the chemical potential μ, the system in the metastable state A is described through the grand potential

$$\Omega_A = -p_A V, \tag{2.6}$$

where p_A is the pressure and V the volume. For the grand potential density that means

$$\omega_A = \frac{\Omega_A}{V} = -p_A\,. \tag{2.7}$$

For a system which reached the stable state B the same equations apply with pressure p_B.

For a nucleus (denoted by subscript AB) the system contains both, state A and state B, as well as an interface, which means the volume V is split into the state B part with volume v_B and the state A part with volume v_A. In other words, $\Omega_{AB} = \Omega_A|_{v_A} + \Omega_B|_{v_B} + I$, where I is the influence of the interface.

From here several assumptions are made [92]: First, that the nucleus and surrounding phase have the same thermodynamic properties as the full phases (e.g., density, structure). Second, the interface between the nucleus and its surroundings is sharp, meaning $V = v_A + v_B$. Finally, the interface is considered planar, meaning $I \approx a_b\gamma$ with the constant interface tension γ and the size of the interface a_b. This is only approximately true, as the interface is not generally planar and therefore the interface tension γ not constant. It therefore fails for small spherical nuclei, but works well enough for larger radii. In other words, CNT works best when a phase only just turned metastable, leading to large critical nuclei and small pressure differences between phase A and B (i.e., $\Delta p = p_B - p_A$).

Given all these assumptions the grand potential takes the form

$$\Omega_{AB} \approx -p_A(V - v_B) - p_B v_B + a_B\gamma\,. \tag{2.8}$$

The grand potential difference to the metastable state A is given by

$$\Delta\Omega = \Omega_{AB} - \Omega_A \approx -v_B\Delta p + a_B\gamma\,, \tag{2.9}$$

with the small pressure difference Δp, as defined above.

Nucleation naturally requires $\Omega_A > \Omega_B$. Otherwise state A would not be metastable, which means the theory is only valid for $\Omega_A < \Omega_B$ starting from the critical point where phases coexist (cf. Sec. 2.2). At this point $p_A = p_B$ and, therefore, $\Delta p = 0$. Given a known geometry of the surface of the nucleus a_B, this allows for the determination of the surface energy γ, as now $\Delta\Omega = a_B\gamma$.

In three dimensions with a spherical nucleus Eq. (2.9) takes the form:

$$\Delta\Omega_{3D} \approx -\frac{4}{3}\pi R^3 \Delta p + 4\pi R^2 \gamma\,. \tag{2.10}$$

Similarly in two dimensions with a circular nucleus one has:

$$\Delta\Omega_{2D} \approx -\pi R^2 \Delta p + 2\pi R \gamma\,. \tag{2.11}$$

In quasi-1D, i.e., for a rectangle with $L_y \gg L_x$ the equation becomes:

$$\Delta\Omega_{1D} \approx -2RL_x \Delta p + 2L_x \gamma\,. \tag{2.12}$$

All three dependencies (Eqs. (2.10)-(2.12)) are depicted in Fig. 2.5 a) in blue, red and black for one, two and three dimensions, respectively. The curves are linear, quadratic and cubic in turn and each has a maximum value $\Delta\Omega^*$ for $R \geq 0$, which represents the energy that has to be supplied to reach a nucleus with critical radius R^*. As it is an energy maximum both smaller and larger nuclei are more favorable, meaning it is an unstable steady state and the tipping point of moving the whole system into either state A or state B. In a bifurcation diagram the steady states should appear as an unstable branch of localized states, where each point on it is calculated for a different Δp corresponding to a different value of μ.

The critical values R^* and $\Delta\Omega^* = \Delta\Omega(R^*)$ are listed in Tab. 2.1 for the different dimensions.

	1D	2D	3D
R^*	0	$\frac{\gamma}{\Delta p}$	$\frac{2\gamma}{\Delta p}$
a_B^*	$2L_x$	$2\pi R^*$	$4\pi R^{*2}$
$\Delta\Omega^*$	$2L_x\gamma$	$\gamma\pi R^*$	$\frac{16}{3}\gamma\pi R^{*2}$

Table 2.1: Critical values for the radius R^*, the interface size a_B^* and the energy barrier $\Delta\Omega^*$ in one, two and three dimensions.

For the 2D case the dependence of the maxima at R^* on μ is depicted in Fig. 2.5 b), where darker colors are for states with μ closer to μ_c where $\Omega_A = \Omega_B$. As the distance from that point increases, the energy barrier decreases and a smaller nucleation radius is required, because state B becomes energetically more favorable.

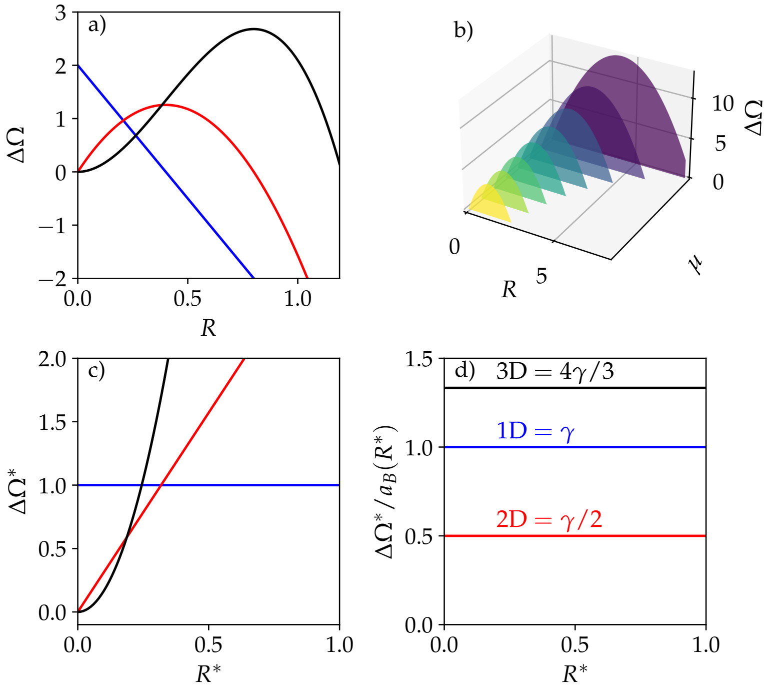

Fig. 2.5: a) The difference $\Delta\Omega$ of the grand potential of the nucleus to the metastable state A is plotted over the radius R of the nucleus as predicted through Eqs. (2.10)-(2.12) for the respective dimensions with line colors black (3D), red (2D) and blue (1D). Parameters $\gamma = 1$, $L_y = 0.5$ and $\Delta p = 2.5$ are freely chosen for demonstration purposes. In consequence, each curve has a set chemical potential μ. b) $\Delta\Omega$ plotted over R for the 2D case for different values of μ. Each color represents a different chemical potential with darker colors being closer to μ_c, and therefore showing a higher energy barrier $\Delta\Omega^*$ and bigger critical radii R^*. c) Energy barrier level $\Delta\Omega^*$ plotted over over the critical radius R^* of the nucleus as listed in Tab. 2.1. d) is same as panel c), but the critical grand potential is rescaled with respect to the critical surface a_B^* of the nucleus. All dimensional influence is reduced to prefactors in constants, which are noted over the respective lines, i.e., apart from dimensional influence the overall behavior is the same.

Fig. 2.5 c) finally shows the dependence of the energy barrier level $\Delta\Omega^*$ on the critical radii for each dimension (same colors as in panel a)), allowing for a comparison to steady state data. The curves are constant (1D), linear (2D) and quadratic (3D). Though they look qualitatively different, Fig. 2.5 d) shows that apart from dimensional effects they scale the same. To that end the critical grand potential is scaled with respect to the critical surface $a_B^* = a_B(R^*)$ (see Tab. 2.1).

2.4 Localized States and Coexistence at Finite Size

Unlike CNT, which is considered in the thermodynamic limit, systems are generally simulated at finite size and only later generalized to the thermodynamic limit. This generalization is trivial for uniform states while periodic patterns show some changes from the thermodynamic limit case. Those changes, however, are negligible for many (but not all) systems.

Nucleation, however, is a very size-dependent phenomenon. In a particle reservoir system, a bifurcation diagram would show an equivalent of the critical nucleus in form of an unstable steady state, which is commonly referred to as a localized state. As before, it is defined as a state where a finite patch of one phase coexists with a background of another. Unlike before, however, at least one phase is a patterned state [98]. Examples of this can be found in Fig. 2.7 a)-c) for one dimension or 2.1 e) for two dimensions. If the system is closed, i.e., is controlled by fixing the density ρ (rather than μ) the localized state can also be a stable steady state.

Localized states can appear close to phase transitions in parameter regions of phase coexistence [181, 83]. This means two (or more) different stable states (with different mean densities) exist, which are connected by the Maxwell construction (cf. Sec. 2.2). They have equal chemical potential μ and grand potential Ω (see also Fig. 2.4, which works nearly the same for coexistence of a uniform and a patterned phase [181]).

Independent of the analyzed system, branches of localized states have a very distinctive structure within bifurcation diagrams, depending on the parameter region. For example, states consisting of a patterned and a uniform state lead to two corresponding primary branches, one with an odd (red) and one with an even (rose) number of pattern layers, which are in turn connected by branches of asymmetric localized states (blue). An example of the bifurcation diagram can be found in Fig. 2.6 with examples of the odd, even and asymmetric localized states in 1D given in Fig. 2.7 a)-c), respectively. The odd and even states wind around each other like snakes with the asymmetric states resembling the rungs of a ladder. Consequently, this branch form is referred to as a snakes-and-ladders structure, or alternatively as 'homoclinic snaking' [29, 194, 98].

The snaking follows a line, the Maxwell line, between the coexisting states (black circles), i.e., the states with matching μ and Ω. Depending on whether the system is

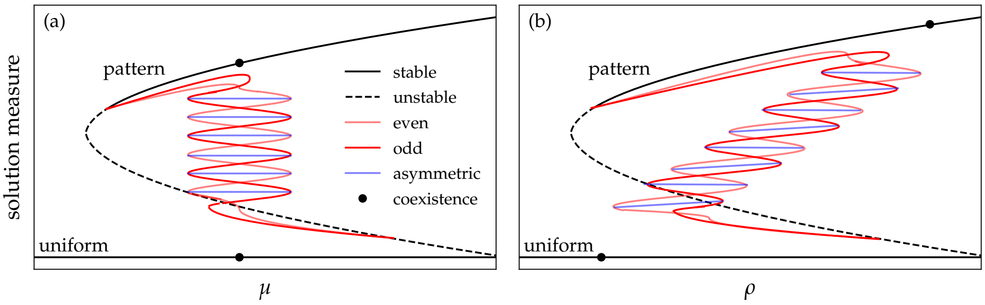

Fig. 2.6: Sketch of typical snaking behavior considered for (a) controlled chemical potential μ and (b) controlled density ρ. The black branches are for uniform and patterned stable (solid) and unstable (dashed) states, as indicated at the branches. The coexistence of states (black circles, equal μ and Ω) results in localized states, which have an odd (red) or even (rose) number of pattern layers, connected by asymmetric (blue) states (stabilities not indicated for ease of viewing). The localized branches emerge from the patterned branch, then perform the typical snaking and finally reconnect with the pattern branch again, at which point the latter becomes stable. The form of the snaking follows a line between the coexisting states which is either vertical (a) or slanted (b).

considered at fixed chemical potential (Fig. 2.6 (a)) or density (Fig. 2.6 (b)), this line and consequently the snaking will be vertical or slanted, respectively. Each snaking curve represents the addition of another layer of pattern, as shown in Fig. 2.7 d), where the layer appears by way of the growth of a single additional peak. Depending on parameter values, the snaking might be less pronounced, leading to fewer folds, which culminates in two largely straight branches with no folds, but the primary ones, in which case peaks do no longer grow in individual layers. Instead, several peaks form a front, which is slowly pushed outward as inner peaks reach optimum height, while new outer layers are added [182, 83, 97]. An example of the latter can be found in Fig. 2.7 e).

Ref. [181] takes a closer look at the effect of finite size on localized states as opposed to the thermodynamic limit. A fairly obvious consequence of increasing system sizes is that the amount of snaking of the branches of localized states rises proportional to the system size, as there is now more room to add pattern layers to the localized structure. In addition, all globally stable localized structures in the thermodynamic limit (both with and without snaking) have the same value of μ, and match perfectly with the Maxwell construction. In the finite size case, however, globally stable parts of the snaking branches appear on a narrow band of chemical potentials $\Delta\mu$ around

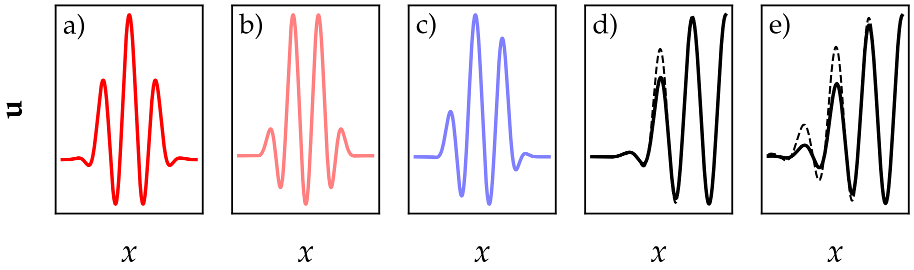

Fig. 2.7: Examples of localized states in one dimension. They have a) odd or b) even peak numbers, or can be c) asymmetric. Panels d) and e) show the addition of further peak layers (dashed line) through growth of either single or multiple peaks, respectively.

the Maxwell line.

2.5 Numerical Analysis of Nonlinear Partial Differential Equations

2.5.1 Spatial Discretization and Fourier Transform

For a system described by Eq. (2.1) the thesis now assumes $\mathbf{u}(\mathbf{x}, t)$ to be a field with spatial discretization of $N \in \mathbb{N}$ grid points, i.e., $\mathbf{x}$ now consists of discrete positions x_j with $j \in [1, N]$. In all following equations $\mathbf{u}(t)$ now consists of all $\mathbf{u}(x_j, t) = \mathbf{u}_j(t)$.

Furthermore, the right-hand side $\mathbf{G}$ of Eq. (2.1) is split into two parts

$$\partial_t \mathbf{u} = \mathbf{G}(\mathbf{u}) = \mathcal{L}(\mathbf{u}) + \mathcal{N}(\mathbf{u}) \tag{2.13}$$

with linear part $\mathcal{L}(\mathbf{u}) = \mathcal{L}\mathbf{u}$, which is diagonal in Fourier space, and a part $\mathcal{N}(\mathbf{u})$, which can contain nonlinear terms and functions of space.

In Fourier space $\mathbf{k}$ is also discretized into grid points k_m with $m \in [1, N]$. As $\mathbf{x}$ and $\mathbf{k}$ are also restricted in their range, the discrete Fourier transform [148] is used to move to and from Fourier space. The one dimensional version is[3]

$$\mathcal{F}[f](k_m) = \hat{f}(k_m) = \sum_{j=0}^{N-1} f(x_j) e^{-i2\pi jm/N} \tag{2.14}$$

$$\mathcal{F}^{-1}[\hat{f}](x_j) = f(x_j) = \frac{1}{N} \sum_{m=0}^{N-1} \hat{f}(k_m) e^{i2\pi jm/N} \,. \tag{2.15}$$

The Fourier transform simplifies convolutions and spatial derivatives to multiplications with functions of the wave vector [148]:

$$\int \mathrm{d}\mathbf{x}' g(\mathbf{x}-\mathbf{x}') f(\mathbf{x}') \quad \leftrightarrow \quad \hat{g}(\mathbf{k})\hat{f}(\mathbf{k}) \tag{2.16}$$

$$\nabla^n f(\mathbf{x}) \quad \leftrightarrow \quad (i\mathbf{k})^n \hat{f}(\mathbf{k}) \,. \tag{2.17}$$

The pseudospectral method [16, 27] makes use of the accompanying lowered computational costs. Specifically, for N grid points a convolution in one dimensional real space takes N^2 operations, whereas the associated multiplication in Fourier space only takes N operations. However, the computational cost of moving a field to and from Fourier space needs to be taken into account as well. The Fast Fourier Transform algorithm [27] cuts down on the number of operations required to perform the discrete Fourier transform to $N \log N$ by splitting them into odd and even parts.

In summary, even with the Fourier transformations taken into account it is numerically cheaper to treat $\mathcal{N}$ in real space while moving derivatives and convolutions to Fourier space for computation.

2.5.2 Time Evolution Methods

To study nonlinear differential equations by way of direct time evolution the first step is to discretize it in time t through integration over a time interval Δt, meaning

$$\mathbf{u}(t+\Delta t) - \mathbf{u}(t) = \int_t^{t+\Delta t} \mathbf{G}(\mathbf{u}) \mathrm{d}t \,. \tag{2.18}$$

Here $\mathbf{G}(\mathbf{u})$ once again represents the right-hand side of the the equation.

---

[3] Note that a constant factor of the real space sampling distance Δx $[1/\Delta x]$ needs to be multiplied to Eq. (2.14) [Eq. (2.15)] in case of only transforming in one direction. When performing both they cancel out.

Rewriting that leads to

$$\mathbf{u}(t+\Delta t) = \mathbf{u}(t) + \int_{t}^{t+\Delta t} \mathbf{G}(\mathbf{u})\mathrm{d}t\,, \tag{2.19}$$

which can be solved step wise if given an initial condition $\mathbf{u}(\mathbf{x}, t=0)$ (e.g., noise, a sine pattern or previous results). From there the solution evolves towards a stable state, meaning a fixed point, periodic orbit or strange attractor.

Semi-Implicit Euler
Generally the Euler's method [16] assumes that $\mathbf{G}(\mathbf{u})$ is constant over the time interval Δt, meaning the area beneath can be considered a rectangle, which simplifies the time integral in Eq. (2.19) to $\mathbf{G}(\mathbf{u})\Delta t$, i.e.,

$$\mathbf{u}(t+\Delta t) = \mathbf{u}(t) + \mathbf{G}(\mathbf{u})\Delta t\,. \tag{2.20}$$

If the constant is chosen to be $\mathbf{G}(\mathbf{u}(t))$, meaning the start of the time interval, the method is called explicit Euler. Like all explicit methods it has a maximum time step beyond which the error grows exponentially [27]. If the constant is chosen to be the end of the interval, meaning $\mathbf{G}(\mathbf{u}(t+\Delta t))$, the method is called implicit Euler, which is more forgiving of larger time steps, but requires the computation of $\mathbf{u}(t+\Delta t)$ at every step, which is numerically expensive.

The semi-implicit Euler method combines parts of both the implicit and explicit methods, keeping the numerical computation cost lower than for the implicit Euler, while allowing larger time steps than the explicit Euler. To that end $\mathcal{L}(\mathbf{u})$ is calculated implicitly and $\mathcal{N}(\mathbf{u})$ is calculated explicitly. This leads to

$$\mathbf{u}(t+\Delta t) = \mathbf{u}(t) + \Delta t[\mathcal{L}\mathbf{u}(t+\Delta t) + \mathcal{N}(\mathbf{u}(t))]\,. \tag{2.21}$$

Sorting all $\mathbf{u}(t+\Delta t)$ terms to the left and everything else to the right-hand side gives

$$\mathbf{u}(t+\Delta t) = \frac{\mathbf{u}(t) + \Delta t\mathcal{N}(\mathbf{u}(t))}{(1-\Delta t\mathcal{L})}\,, \tag{2.22}$$

if $\mathcal{L}$ can safely be separated from $\mathbf{u}$ as is sometimes the case in Fourier space, where $\widehat{\mathcal{L}}$ is a function of $\mathbf{k}$.

In this thesis both self written and adapted python code is used for simulations.

Fourier Split-Step
The Fourier split-step method [1, 14, 191, 58] is a pseudospectral method which,

similar to the semi-implicit Euler, splits the Hamiltonian on the right-hand side into $\mathcal{L}$ and $\mathcal{N}$, though it is primarily used for Schrödinger-type equations, meaning

$$i\hbar\partial_t\psi(\mathbf{x},t) = [\mathcal{L} + \mathcal{N}(\psi(\mathbf{x},t))]\psi(\mathbf{x},t)\,, \tag{2.23}$$

where ψ is a complex wave function.

This type of equation has a formal solution of the form

$$\psi(\mathbf{x},t+\Delta t) = e^{-i\Delta t(\mathcal{L}+\mathcal{N})/\hbar}\psi(\mathbf{x},t)\,. \tag{2.24}$$

The Baker-Campbell-Hausdorff formula [32] shows that multiplying exponential functions of non-commuting operators $\hat{a}$ and $\hat{b}$ leads to

$$e^{\hat{a}}e^{\hat{b}} = e^{\hat{a}+\hat{b}+[\hat{a},\hat{b}]/2+\dots}\,. \tag{2.25}$$

Consequently, when ignoring the the non-commuting nature of $\mathcal{L}$ and $\mathcal{N}$, Eq. (2.25) facilitates to

$$e^{\Delta t\mathcal{L}}e^{\Delta t\mathcal{N}} = e^{\Delta t(\mathcal{L}+\mathcal{N})}\,. \tag{2.26}$$

The dropped terms causes an error proportional to Δt^2 with every time step of size Δt. Given a small enough time step this error is minimal, allowing the use of

$$\psi(\mathbf{x},t+\Delta t) \approx e^{-i\Delta t\mathcal{L}/\hbar}e^{-i\Delta t\mathcal{N}/\hbar}\psi(\mathbf{x},t)\,. \tag{2.27}$$

From there the parts which are diagonal in Fourier space are computed there, while the rest is computed in real space.

The error can be reduced to Δt^3 if the linear exponential function is split further in half and moved to both sides of the nonlinear exponential, symmetrizing the operators in Eq. (2.25). Each part of the linear exponential is now propagated for only half a time step [1]:

$$\psi(\mathbf{x},t+\Delta t) \approx e^{-i\Delta t\mathcal{L}/2\hbar}e^{-i\Delta t\mathcal{N}/\hbar}e^{-i\Delta t\mathcal{L}/2\hbar}\psi(\mathbf{x},t)\,. \tag{2.28}$$

The final equation therefore takes the form

$$\widehat{\psi}(\mathbf{x},t+\Delta t) \approx e^{-i\Delta t\widehat{\mathcal{L}}/2\hbar}\mathcal{F}[e^{-i\Delta t\mathcal{N}/\hbar}\mathcal{F}^{-1}[e^{-i\Delta t\widehat{\mathcal{L}}/2\hbar}\widehat{\psi}(\mathbf{x},t)]]\,. \tag{2.29}$$

Leaving the equation as is, is known as real-time propagation, where the norm and energy are conserved, while the wave function fluctuates. This type of propagation can be used to evolve or test the robustness of solutions.

Alternatively the total energy can be minimized through a gradient flow, which is also known as imaginary-time propagation [14] and requires that the original equation is converted using $t \to -it$. As the norm is no longer conserved, renormalization is needed after each step.

In this thesis a self written parallelized python code is used for simulations.

2.5.3 Path Continuation

Path continuation [52, 185, 166] is a systematic way of looking through parameter space. It is useful to avoid lengthy parameter sweeps of time simulations and to gain additional information on unstable branches.

Path continuation works by following the steady state solutions which satisfy $\partial_t \mathbf{u} = \mathbf{G}(\mathbf{u}) = 0$, starting from a known solution $\mathbf{u}_0(\mathbf{x})$.

From there a continuation parameter λ is varied by a small step size $\Delta\lambda$ (i.e., $\lambda_{n+1} = \lambda_n + \Delta\lambda$) and the new solution $\mathbf{u}_{n+1}(\mathbf{x})$ is predicted (e.g., by following the tangent at $\mathbf{u}_n(\mathbf{x})$) and then corrected by solving Eq. (2.1) at λ_{n+1}. This is most commonly done through Newton's method.

The prediction method is depicted in Fig. 2.8 a), which also highlights the problem of this method. It's a natural parametrization, which fails when the solution folds back.

To get around that the pseudo-arclength parametrization uses the arclength s of the solution branch as continuation parameter instead of λ, which becomes part of the solution instead, meaning Eq. (2.1) is replaced by

$$\dot{\mathbf{u}}(\mathbf{u}_{n+1} - \mathbf{u}_n) + \dot{\lambda}(\lambda_{n+1} - \lambda_n) = \Delta s\,, \tag{2.30}$$

with the tangent $\mathbf{v} = (\dot{\mathbf{u}}, \dot{\lambda})$, and steps size Δs. This is depicted in Fig. 2.8 b).

From there the stability of the solution can be calculated through the eigenvalues of the Jacobian $\underline{\mathbf{J}}$ as explained in Sec. 2.1. Any time an eigenvalue crosses the imaginary axis there is a bifurcation, which some path continuation packages can use to switch branches.

If the system has additional constraints they are added as additional equations $q(\mathbf{u}, \lambda) = 0$ to the system of differential equations in (2.1) or (2.30), while additional parameters λ_{add} are used together with the original continuation parameters λ, to avoid overdetermining the system [52].

A constraint appearing in isolated and many closed systems is the conservation of density (cf. Ref. [52]), which leads to the additional equation

$$q_{\text{density}} = \frac{1}{V}\int \mathbf{u}\mathrm{d}\mathbf{x} - \bar{\mathbf{u}} = 0 \tag{2.31}$$

with mean density $\bar{\mathbf{u}}$ and the additional parameter λ_{density}, which is related to the chemical potential and changes the original equation to $\partial_t \mathbf{u} = \mathbf{G}(\mathbf{u}, \lambda) + \lambda_{\text{density}}$.

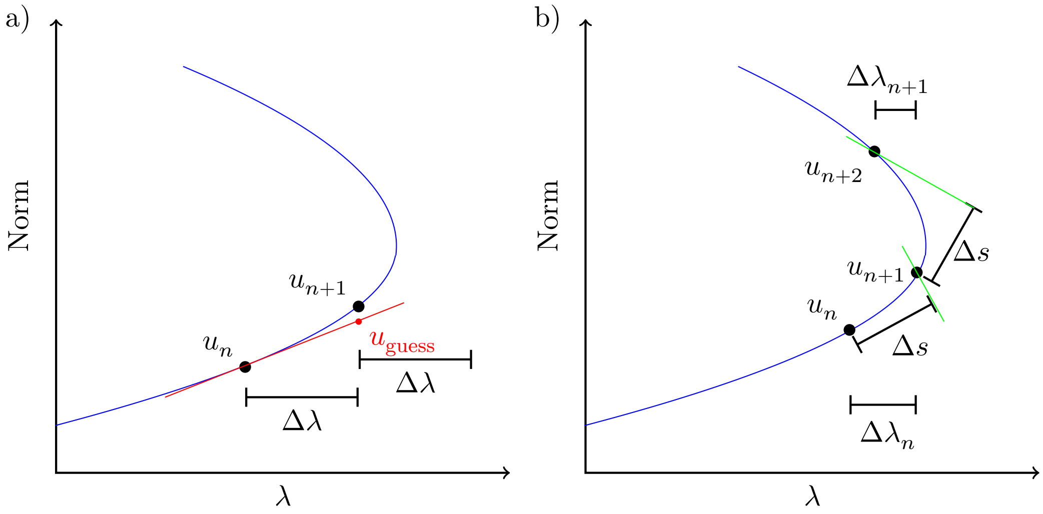

Fig. 2.8: a) Natural parametrization in path continuation. Starting from u_n parameter λ is varied by a small step $\Delta\lambda$ and a solution u_{guess} estimated by following the tangent (red). Correction (e.g., through Newton's method) leads to true solution u_{n+1}. Method fails at saddle-node bifurcation. b) Pseudo arclength path continuation. Starting from u_n arclength s is varied by a small step Δs which corresponds to different $\Delta\lambda$. As the Δs are not bound by the axis direction they can curve around a saddle-node bifurcation, while keeping previous predictor and corrector methods (green).

Another constraint is phase conservation [52] in periodic solutions, which is introduced for each direction where translation invariance applies (i.e., directions with periodic boundary conditions). Without it, every single phase shift in $\mathbf{u}$ would register as a different solution. This is called motion along the group orbit and can be prevented through permitting only solutions which are situated perpendicular to said group orbit. For that a reference profile $\mathbf{u}^*$ (e.g., the solution of the previous continuation step) is required, leading to the additional equation

$$q_{\text{phase}} = \int \mathbf{u}\partial_x \mathbf{u}^* \mathrm{d}\mathbf{x} = 0\,, \tag{2.32}$$

for phase conservation in x-direction. The additional parameter λ_{phase} changes the original equation to $\partial_t \mathbf{u} = \mathbf{G}(\mathbf{u}, \lambda) + \lambda_{\text{phase}} \partial_x \mathbf{u}$. This is equivalent to transforming the system into a comoving frame with velocity λ_{phase}.

For most problems the spatial discretization is based on finite elements [185, 65], but others (e.g., networks [186]) are possible. Specifically, for problems which are easier to solve in Fourier space, there are options of working with Fourier spectral differentiation matrices [186]. It works remarkably similar to the previously discussed method with the pseudospectral method used to solve the right hand side. Any move to and from Fourier space is done by way of a discrete cosine function, which can be applied directly or in form of a spectral differentiation matrix.

In this thesis the matlab package *pde2path* [185] is used.

3 Soft Matter Physics

3.1 Introduction to Soft Matter Physics and Models

Soft matter [46, 198, 45] describes materials which have a large, nonlinear response to small stimuli, often in form of deformations. This same response also tends to be slow, meaning that even equilibrium soft matter systems can spend comparatively long times outside of said equilibrium. In such a system, compared to "hard" matter, the driving force for structuring is not dominated by the interaction between particles. Instead, those interactions are of the same order of magnitude, or even lower than that of the entropy, which enters, e.g., in the form of thermal fluctuations. In other words, the drive towards equilibrium, i.e., a state of minimum free energy, is a question of interplay between the two or even outright dominated by the entropy, which in turn causes self-organization [198]. In non-equilibrium soft-matter physics structuring can be influenced or even caused in response to adding external fields [99] (cf. Ch. 4).

One way of modeling soft matter systems is through dynamical density functional theory (DDFT) [11, 51, 119, 120, 10, 9], which was originally developed for overdamped Brownian particle movement, based on stochastic equations. These days it is much more general, working for interacting classical particles in a non-equilibrium system and resulting in the time evolution of the ensemble's average one-body density field ρ.

DDFT corresponds to dynamics given by the continuity equation

$$\partial_t \rho = -\nabla \cdot \mathbf{j} \,, \tag{3.1}$$

where ∂_t is the partial derivative with respect to time t, ∇ the nabla operator and $\mathbf{j}$ a current with [57]

$$\mathbf{j} = \beta M(\rho) \nabla \mu \,. \tag{3.2}$$

Here $\beta = 1/k_B T$ with temperature T and Boltzmann constant k_B. M is a positive mobility depending on the density, which in the following will be $M = \rho$. The chemical potential μ can be calculated using functional derivatives[1] of the Helmholtz free energy F with respect to the density:

$$\mu = \frac{\delta F}{\delta \rho} \,. \tag{3.3}$$

Under exclusion of external potentials F consists of two parts. The first is the entropic ideal gas contribution, the second part F_{int} adds particle interactions:

$$F = \frac{1}{\beta} \int \rho[\log(\rho) - 1] \, \mathrm{d}^3x + F_{\text{int}} \,. \tag{3.4}$$

F_{int} requires some approximations to get to an expression of only a single convolution with an interaction potential U_{int} [11]. F_{int} is also where applications to different scenarios enter, as different particle interactions are modeled by different potentials.

In this thesis a potential for particles with soft, repulsive pair interactions is used, which can be described using the generalized exponential model with the exponent n, 'GEM-n' for short. It takes the form $U_{\text{int}}(r) = \varepsilon e^{-(r/R)^n}$. For $n = 4$ the model represents a coarse grained potential for soft particles in a solution, e.g., polymers whose structure allows for a limited overlap [8].

Starting from the exact DDFT (Eqs. (3.1)-(3.4)) many approximations exist, which facilitate the practical modeling of problems at the cost of accuracy. Such is the case for the Phase-Field Crystal (PFC) model [51, 11, 86, 179, 50], which was originally developed as a phenomenological model of crystal growth [49], but has since been used for modeling liquid-solid phase transitions, foam formation, colloids, liquid crystals and many more [51].

The PFC model is a classical pattern forming equation with a conserved dynamic and is well researched (see e.g. [182]). It takes the form

$$\partial_t \rho = \nabla^2 \mu \,, \tag{3.5}$$

i.e., Eqs. (3.1) and (3.2) but with constant M. The main change with respect to the DDFT model appears in the Helmholtz free energy F, where both, logarithm and the interaction potential, are approximated. In consequence, the PFC model differs from DDFT in prominent ways: There are two additional phases which do not appear in DDFT, as well as an additional phase transition at higher densities, as described in Ref. [11].

In addition to that, the PFC model has large parameter regions which show snaking behavior for localized states, a phenomenon which has not been observed in DDFT as modeled with the GEM-4. From there the question arises whether the appearance of snaking in the PFC model is caused by the approximations. If that were the case then the next question is whether this arises due to approximating the long-range interaction, approximating the logarithm or a combination of both.

---

[1] For $F = \int f(\rho, \nabla\rho, \dots)\mathrm{d}r$ with $\rho = \rho(r)$ it is $\delta F/\delta\rho = \sum_{i=0}(-1)^i \nabla^i \partial f/\partial(\nabla^i \rho)$.

Finally, it is of interest how snaking or the lack thereof influences the phase transition, for which this thesis draws on classical nucleation theory.

3.2 The DDFT Model with GEM-4 Potential

3.2.1 The Model

The GEM-4 pair potential takes the form

$$U_{\text{int}}(r) = \varepsilon e^{-(r/R)^4} \,. \tag{3.6}$$

It has a characteristic length scale R, interaction strength ε and inter-particle distance r. Generally, it looks like a softened Heaviside function with the height given by ε and the radius given by R. An example for $R = \varepsilon = 1$ is depicted in Fig. 3.1 a).

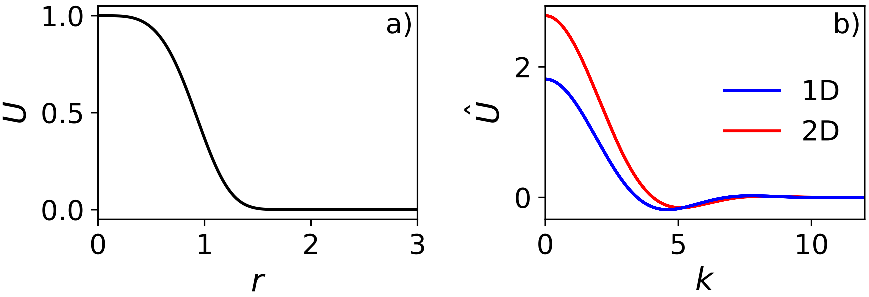

Fig. 3.1: Pair potential for $R = \varepsilon = 1$ in a) real space $U(r)$ (see Eq. (3.6)) and b) Fourier space $\hat{U}(k)$, calculated via Eq. (3.12) for 1D (blue) and Eq. (3.13) for 2D (red).

The corresponding DDFT model, taken from Ref. [11] (where it appears as DDFT-3) has the form

$$\partial_t \rho = \nabla \left[(\rho + 1) \nabla \frac{\delta F}{\delta \rho} \right] \,, \tag{3.7}$$

with the free energy

$$\beta F = \int \mathrm{d}x \left[(1+\rho) \log (1+\rho) - \rho + \frac{1}{2} \rho \rho_0 \beta (U_{\mathrm{int}} * \rho) \right] , \tag{3.8}$$

where $\beta = 1/k_B T$.

$$\rho' = \rho_0 (1+\rho) \tag{3.9}$$

represents the actual density of the system, split into a constant reference density ρ_0, also called bulk fluid density, and ρ, a density modulation field. The mean density follows as $\bar{\rho}' = \rho_0(1+\bar{\rho})$ where $\bar{\rho}$ does not have to be zero. The trivial homogeneous state $\rho = \bar{\rho} = \mathrm{const}$ has no clustering and the model describes a fluid. Values of $\rho' < 0$ and therefore $\rho < -1$ do not constitute a physically sensible solution. Also, $\rho = -1$ leads to trouble in the free energy (3.8), due to the $\log(1+\rho)$ term.

Finally, $(U * \rho) = \int U(r - r')\rho(r')\mathrm{d}r'$ is a convolution and represents the long-range interaction. Given the nature of convolutions it is convenient to treat this part of the equation in Fourier space, where $\widehat{U}_{\mathrm{int}}$ has a minimum below zero, which satisfies the Likos criterion [107], which states that such a minimum is required for the uniform phase to become unstable in favor of clustering. For larger k the Fourier interaction potential relaxes to zero. Examples of this in one (blue, Eq. (3.12)) and two (red, Eq. (3.13)) dimensions can be found in Fig. 3.1 b).

Introducing length- and timescales $x = Rx_s$, $y = Ry_s$, $r = Rr_s$ and $t = R^2 t_s$ (see App. A.2) Eq. (3.7) can be rescaled to

$$\partial_t \rho = \nabla [(1+\rho) \nabla [\log(1+\rho) + \alpha(u * \rho)]] , \tag{3.10}$$

where $\alpha = \varepsilon R^d \rho_0 \beta$, while

$$u = e^{-r^4} \tag{3.11}$$

no longer depends on R and energy scale ε.

The Fourier transformations $\hat{u}(k)$ of Eq. (3.11) are [150, 151]

$$\hat{u}_{1D}(k) = 2 \int_0^\infty \mathrm{d}r \, U(r) \cos(kr) , \tag{3.12}$$

$$\hat{u}_{2D}(k) = 2\pi \int_0^\infty \mathrm{d}r \, rU(r) J_0(kr) , \tag{3.13}$$

which use radial symmetry to go from the exponential function of the general Fourier transformation to the cosine function cos and Bessel function of the first kind J_0 multiplied by r, respectively. Both functions are even, meaning $\hat{u}(-k) =$

$\hat{u}(k)$. In 1D for $k = 0$ the Fourier potential $\hat{u}_0 = \hat{u}(k = 0)$ is $\hat{u}_0 = 2\Gamma(5/4)$ with Γ being the Gamma function. In 2D $\hat{u}_0 = \sqrt{\pi}^3/2$. The results are also listed in Tab. 3.2.

The accompanying free energy is

$$F = \int \mathrm{d}x \left[(1+\rho)\log(1+\rho) - \rho + \frac{1}{2}\rho\alpha(u * \rho)\right] \tag{3.14}$$

and the chemical potential:

$$\mu = \frac{\delta F}{\delta \rho} = \log(1+\rho) + \alpha(u * \rho)\,. \tag{3.15}$$

The grand potential density takes the form

$$\frac{\Omega}{V} = \omega = \frac{F}{V} - \mu(1+\rho)\,, \tag{3.16}$$

where V is the volume (or area, length) of the system.

For a uniform state $\rho = \bar{\rho}$ it follows

$$F_0 = V\left[(1+\bar{\rho})\log(1+\bar{\rho}) - \bar{\rho} + \frac{\bar{\rho}^2\alpha\hat{u}_0}{2}\right]\,, \tag{3.17}$$

$$\mu_0 = \log(1+\bar{\rho}) + \bar{\rho}\alpha\hat{u}_0\,, \tag{3.18}$$

$$\omega_0 = -\bar{\rho}\left(1 + \alpha\hat{u}_0\left(1 + \frac{\bar{\rho}}{2}\right)\right)\,, \tag{3.19}$$

due to $(u * \bar{\rho}) = \bar{\rho}\hat{u}_0$.

3.2.2 Temporal Stability

In this section the stability of homogeneous states with respect to perturbations is investigated, as explained in Sec. 2.1. This results in a dispersion relation for Eq. 3.10 of the form

$$\sigma = -k^2(1 + \alpha(1+\bar{\rho})\hat{u}(k))\,. \tag{3.20}$$

As $\hat{u}$ is a radially symmetric function the same is true for σ. As typical for models under conservation laws σ is zero at $k = 0$. It has an additional maximum at a wavenumber $k > 0$. This maximum is the first point to cross zero, at which point it gives the critical wavenumber k_c. This is a conserved-Turing instability, meaning if the maximum rises further this results in a band of unstable wavenumbers and therefore pattern formation. The moment the maximum crosses zero is depicted in Fig. 3.2 a) for 1D (blue) and 2D (red).

The parameters required for σ to cross zero can be determined by imposing $\sigma = 0$ and $\partial_k \sigma = 0$, while discarding $k = 0$. With the derivative of σ with respect to k being

$$\partial_k \sigma = -2k(1 + \alpha(1 + \bar{\rho})\hat{u}) - \alpha(1 + \bar{\rho})k^2 \partial_k \hat{u} = 0\,. \tag{3.21}$$

This is solved by $\partial_k \hat{u} = 0$ and $\alpha(1 + \bar{\rho})\hat{u} = -1$.

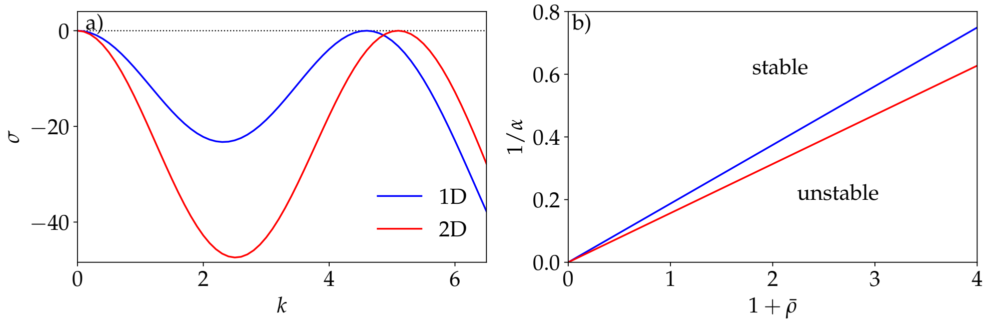

Fig. 3.2: a) Dispersion relation for $\alpha(1 + \bar{\rho}) = (\alpha(1 + \bar{\rho}))_c$ in 1D (blue line) and 2D (red line). The thin dotted line matches $\sigma = 0$ and is used as a guide to the eye. The dispersion relation touches it at $k = 0$ and $k = k_c$ where k_c matches the values in Tab. 3.1. b) Border of linear stability, split into a two parameter space with $1/\alpha \propto T$ over $1 + \bar{\rho}$. The curves for 1D (blue line) and 2D (red line) follow $\alpha = (1 + \bar{\rho})/(\alpha(1 + \bar{\rho}))_c$ with the critical value set according to Tab. 3.1.

Critical values can not be calculated analytically, but numerical evaluation gives the values in Tab. 3.1.

	1D	2D
k_c	4.592	5.096
$(\alpha(1 + \bar{\rho}))_c$	5.34	6.376

Table 3.1: Critical values for the wave vector k and the compound parameter $\alpha(1 + \bar{\rho})$ in one and two dimensions.

The resulting border of linear stability is just $1/\alpha \propto (1 + \bar{\rho})$, see Fig.3.2 b) for the linear dependencies for one (blue) and two (red) dimensions.

3.3 DDFT Approximations and the PFC Model

3.3.1 Approximating the Fourier Potential

This approximation, here denoted as GEM-4-ε, appears in Ref. [11] as DDFT-5. The idea is to express $\hat{u}$ as a Taylor series up to order k^4, and then match the border of linear stability as well as the curvature $\kappa = \partial_k^2 \sigma|_{k=k_c}$ of the dispersion relation to the full GEM-4 model. The values of κ as well as of $\hat{u}_{0\varepsilon} = \hat{u}_\varepsilon(k=0)$ are given in Tab. 3.2.

	1D	2D
$\hat{u}_0$	$2\Gamma(5/4)$	$\sqrt{\pi}^3/2$
$\hat{u}_{0\varepsilon}$	0.39	0.661
κ	0.219	0.252

Table 3.2: Curvature parameter $\kappa = \partial_k \sigma|_{k=k_c}$ of the dispersion relation Eq. (3.20), as well as the interaction potential $\hat{u}_0$ at $k = 0$ for the GEM-4 model and the GEM-4-ε approximation ($\hat{u}_{0\varepsilon}$) in one and two dimensions.

The resulting potential takes the form

$$\hat{u}_\varepsilon = \frac{\kappa}{8k_c^2}(k_c^2 - k^2)^2 - \frac{1}{(\alpha(1+\bar{\rho}))_c} \,. \tag{3.22}$$

All remaining equations stay the same as for the GEM-4, including the borders of linear stability and critical values.

According to Ref. [11] this approximation has a smaller coexistence region than the full DDFT, and said coexistence is closer to the border of linear stability. In addition, the patterned state exhibits physically impossible negative densities at higher mean densities.

3.3.2 Approximating the Logarithm and Using Constant Mobility

This approximation is called PFC-γ and appears in Ref. [11] under the same name. The idea is to express $(1+\rho)\log(1+\rho)$ as a Taylor series around $\rho = 0$ up to ρ^4 and keep the mobility constant ($M = 1$), instead of $M \propto 1+\rho$ during the derivation from the DDFT theory (see Ref. [11]).

The resulting model takes the form

$$\partial_t \rho = \Delta\left(\rho + \alpha(u * \rho) - s\rho^2 + t\rho^3\right) \,, \tag{3.23}$$

where $s = 1/2$ and $t = 1/3$. The energy and chemical potential in this approximation are:

$$F = \int \mathrm{d}x \, \frac{\rho^2}{2} - s\frac{\rho^3}{3} + t\frac{\rho^4}{4} + \frac{1}{2}\rho\alpha(u * \rho) \tag{3.24}$$

$$\mu = \rho - s\rho^2 + t\rho^3 + \alpha(u * \rho) \tag{3.25}$$

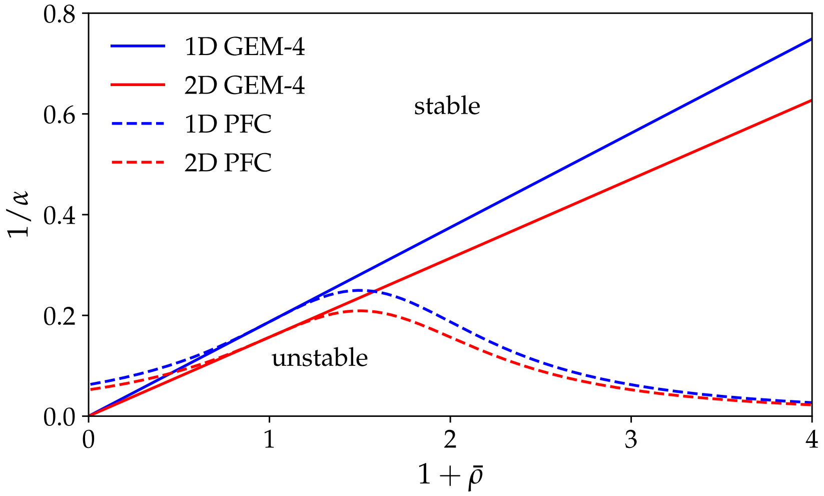

Fig. 3.3: Border of linear stability depending in the $(1+\bar{\rho}$,$1/\alpha)$-plane. One and two dimensions are indicated by blue and red respectively. The GEM-4-ε approximation is per definition indistinguishable from the full GEM-4 case (solid line), while both PFC approximations (dashed lines) only match the GEM-4 model close to $\bar{\rho} = 0$.

While the GEM-4-ε approximation can be made to perfectly match the border of linear stability of the full GEM-4 model, the PFC-γ approximation has the dispersion relation

$$\sigma = -k^2(1 + \alpha\hat{u} - s\bar{\rho} + t\bar{\rho}^2)\,. \tag{3.26}$$

For $\sigma = 0$ and $\partial_k\sigma = 0$ it follows that either $k = 0$ (trivial case) or $\partial_k\hat{u} = 0$ (as before) and $\alpha\hat{u} - s\bar{\rho} + t\bar{\rho}^2 = -1$, which only matches the border of the GEM-4 model close to $\bar{\rho} = 0$, as depicted in Fig. 3.3. Rather than the linear dependence it has a maximum slightly to the right of $\bar{\rho} = 0$, giving it an additional phase transition at higher values of α and no phase transition at low values of α. (Ref. [11] chooses different axes and sets $\bar{\rho} = 0$. As a consequence their borders for full model and PFC approximation match perfectly). Unlike the GEM-4-ε approximation, this approximation matches the dispersion relation of the full GEM-4 model perfectly at $\bar{\rho} = 0$.

In addition to the spurious second phase transition, according to Ref. [11], additional stable solution types (stripes and down hexagons) appear, which make those regions unsuitable for use as a DDFT approximation.

3.3.3 The Full PFC Approximation

This approximation is named PFC-ε and appears in Ref. [11] under the same name, but essentially matches the classical PFC model with a quadratic and cubic term. It applies the GEM-4-ε approximation on PFC-γ, meaning Eq. (3.22) is inserted into Eq. (3.23). The border of stability matches that of PFC-γ.

3.4 Bifurcation Analysis and Localized State Behavior

This section takes a closer look at the GEM-4 model and its approximations by way of bifurcation diagrams, phase diagrams and CNT theory. To measure solutions a classical solution measure of pattern formation is employed: the L_2-norm of the field's deviation from its mean, which is given by

$$||\delta\rho|| = \sqrt{\frac{1}{V}\int_0^V \mathrm{d}^3x(\rho - \bar{\rho})^2}\,, \tag{3.27}$$

where V is the domain size, which, in case of a pattern should be optimally related to its unit cell. In case of localized states the measure is not independent of V, consistency for comparison's sake is therefore required.

This section only details results for two dimensional domains, as they prove more interesting than the ones for one dimensional domains. For the latter see App. A.3.

3.4.1 GEM-4 in Two Spatial Dimensions

The results for two dimensional domains are calculated for a domain of size $L_x \times L_y = L_c/\sqrt{3} \times 14L_c$ with $L_c = 2\pi/k_c$ and $N_x \times N_y = 10 \times 140$ discretization points. The continuation parameter is the mean density $\bar{\rho}$, while α is set to 6.376 so that the border of linear stability can be found at $\bar{\rho}_c = 0$.

The left panel of Fig. 3.4 presents a bifurcation diagram containing branches of two domain spanning patterns, hexagons (blue) and a uniform state (black). In addition, two more patterns (down hexagons and stripes) emerge from the primary bifurcation, which are always unstable (not shown, cf. Fig. 5.7 for same bifurcation type). The primary bifurcation is, therefore, of higher order than the ones presented in Sec. 2.1. Simplified, it consists of a supercritical pitchfork bifurcation for the stripes and a transcritical bifurcation for the hexagons and down hexagons. The latter branch off towards higher mean densities, while the former branch off towards lower densities, before reaching a fold ($1 + \bar{\rho} = 0.84$), at which the branch turns back and continues towards higher densities, creating a multistable region.

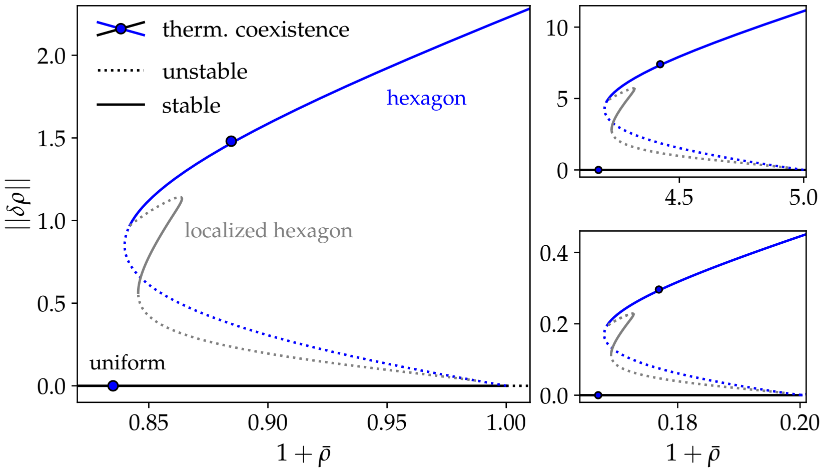

Fig. 3.4: Bifurcation diagrams of steady state solutions of Eq. (3.10) in 2D characterized by $||\delta\rho||$ (see Eq. (3.27)) as a function of $1 + \bar{\rho}$ at different fixed α. On the left, the critical values are $\alpha = 6.376$ with $\bar{\rho}_c = 0$. Top right has $\alpha = 6.376/5$ with $\bar{\rho}_c = 4$ and bottom right has $\alpha = 6.376 \cdot 5$ with $\bar{\rho}_c = -0.8$. The domain size is $L_x \times L_y = L_c/\sqrt{3} \times 14L_c$ with $L_c = 2\pi/k_c$ and $N_x \times N_y = 10 \times 140$ discretization points. The solutions are characterized through $||\delta\rho||$. Solid and dotted lines represent linearly stable and unstable states, respectively. The indicated patterns are uniform states (black), hexagons (blue) and localized hexagons (gray). The two filled circles represent stable coexisting states in an infinite domain (identical grand potential and chemical potential, see Fig.3.5 a) for $\alpha = 6.376$).

In an infinite domain two specific uniform and hexagon states (marked by filled circles) may coexist as given by a Maxwell construction. In a finite domain such a coexistence results in a branch of localized states (gray), where a finite patch of patterned state is embedded in a background of uniform state (or vice versa). The branch corresponding to this state emerges from the still unstable hexagon branch at $1+\bar{\rho} = 0.987$, goes through two saddle-node bifurcations ($1+\bar{\rho} = 0.846$ and 0.864, respectively), between which the solutions are stable, and finally reunites with the hexagon branch beyond the saddle-node bifurcation ($1 + \bar{\rho} = 0.842$), rendering it stable (close up in Fig. 3.6 a)). Note that the localized branch does not exhibit snaking, even if the large domain size would allow for it.

This type of bifurcation diagram stays effectively the same at different values of α, as depicted in the panels on the right of Fig. 3.4. It shows examples at $\alpha = 6.376/5$ with $\bar{\rho}_c = 4$ (top right) and $\alpha = 6.376 \cdot 5$ with $\bar{\rho}_c = -0.8$ (bottom right), which are effectively rescaled versions of the $\alpha = 6.376$ diagram by a factor of 5 and 1/5 respectively.

The coexisting uniform and hexagon states in each of these diagrams are determined via a Maxwell construction, geometrically represented by a crossing of stable branches in the (μ, ω)-plane. Fig. 3.5 a) shows a close up for the $\alpha = 6.376$ case, with the crossing marked with a filled circle. The same circles are shown in Figs. 3.4 and 3.5 c), highlighting the coexisting states. Additionally, Fig. 3.5 b) gives a phase diagram, showing the coexisting states as binodals (continuous line), with the the border of linear stability as spinodal (dashed line). Note that the saddle-node bifurcation on the hexagon branch lies between the binodals in the coexistence region, very close to the left binodal (not shown). The area between the binodals is gray and marks the coexistence region.

Energetically (see Fig. 3.5 d)), the uniform state is the most favorable state up to $1 + \bar{\rho} \approx 0.855$. Then there is a small parameter region of globally stable localized hexagons reaching up to $1 + \bar{\rho} \approx 0.857$. Beyond this point hexagons become the lowest energy state. This is further highlighted in the close up in Fig. 3.6 c). The width of the parameter region where the localized states are linearly stable depends on the domain size, with larger sizes widening the region, while lower sizes ($L_y = 12L_c$ and down) have no globally stable localized states at all.

Fig. 3.5 c) depicts the dependence of $1 + \bar{\rho}$ on μ, which easily shows that there is a marked difference between a system with or without mass conversation ($\bar{\rho}$ or μ as continuation parameter, see, e.g., Ref. [52] (sections 3.2 and 3.3), Ref. [182] (conclusion) or Ref. [83] (end of section 2) for detailed discussions). The former case is what is depicted in Fig. 3.4, though to read the diagram correctly it requires mentally flipping the axes. When read through the lens of a system without mass conservation, however, the diagram can be read as is, but any stability considerations must be re-evaluated as the saddle-node bifurcations shift position to where the branch folds back with respect to μ. This would move the saddle-node bifurcation on the hexagon branch to slightly higher densities. In case of the localized hexagon branch, its start is at $\mu \approx -0.24$ as before, but the saddle-node bifurcations vanish entirely, as there is no longer any point where the branch folds. Subsequently

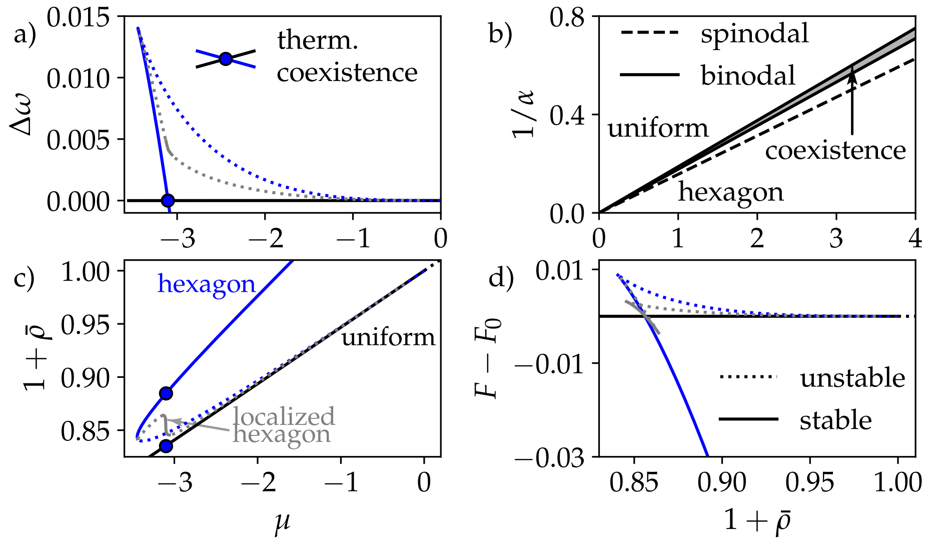

Fig. 3.5: Shown are (a) the grand potential density difference to the liquid state $\Delta\omega$ and (c) the mean density $1+\bar{\rho}$ as a function of the chemical potential μ, as well as (d) the energy difference to the uniform state $F-F_0$ as a function of the mean density $1+\bar{\rho}$, all for the model considered in the left panel of Fig. 3.4 (with matching line styles). The coexistence point (i.e., the crossing of continuous lines in panel (a)) is marked by filled circles, which indicate the existence of localized states. Finally, (b) shows the phase diagram of the two dimensional GEM-4 model, depicting the coexisting states as binodals (continuous line), the border of linear stability as the spinodal (dashed line) and the area between the binodals (gray) where localized states can be found.

there are no changes in the stability of that branch, leaving it completely unstable. In addition, this, as well as the close up in Fig. 3.6 b), highlight that the stable part of the branch of localized states follows a near straight line between the two coexisting states at $\mu=-3.1$.

The right parts of Fig. 3.6 show example profiles of localized states at loci on the branch of localized states as indicated by numbers in Fig. 3.6 a). Two profiles are at the saddle-node bifurcations and three on the different sections between bifurcations. Instead, of individual peaks (or peak layers) growing to full height one after the other, as occurs for normal snaking (see, e.g., Ref. [181]), here a pattern forming front develops. This front has a width of several peaks and all peaks within it grow in such a way that the overall form of the front remains constant. This form, however, only appears between the two saddle-node bifurcations (see panels 2-4). In panel 1 it has not yet fully developed, while panel 5 shows the deformation of the front as the branch reconnects with he full hexagon patterned branch.

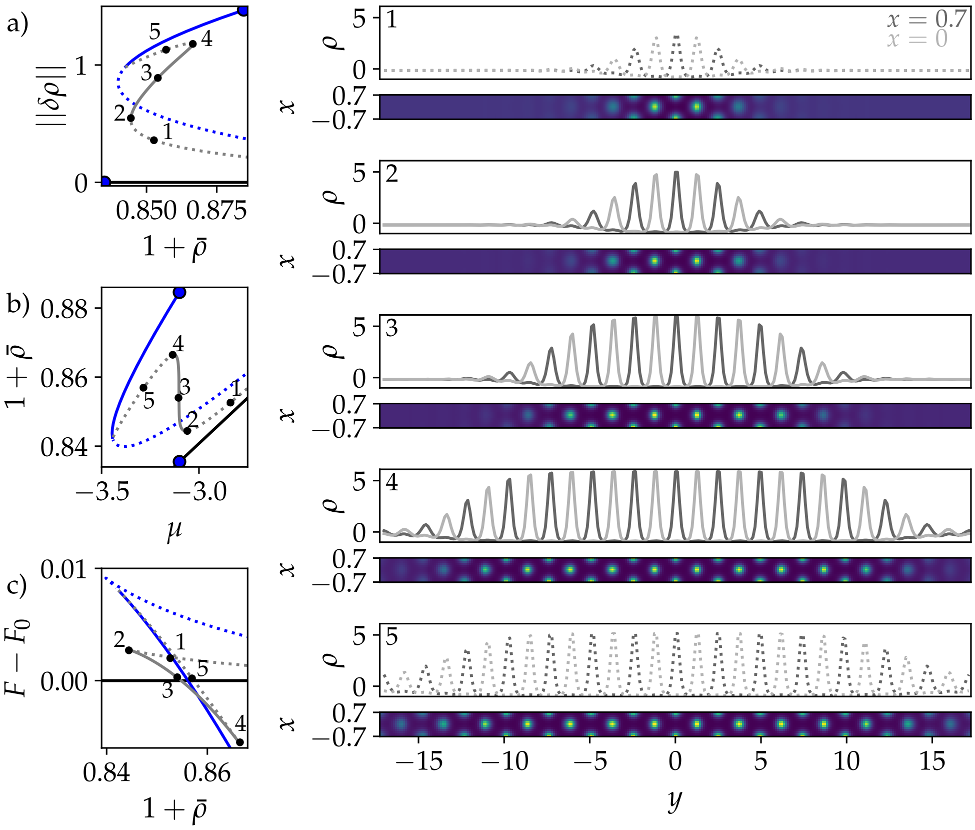

Fig. 3.6: Close ups of (a) the left panel of Fig. 3.4, (b) of Fig. 3.5 (c), and (c) of Fig. 3.5 (d) with five states marked on the localized branch. Stabilities and coexisting states are marked as in Fig. 3.4. In turn the panels highlight (a) the lack of snaking, (b) the straight vertical line of the localized hexagon branch between the coexisting states and (c) the small region where the localized states become the energetically favorable state. Profiles of the marked states are given in the right hand panels 1-5. The lower half of the panels shows the localized pattern, where lighter colors represent higher densities. The upper half shows two cuts through the lower panel at $x = 0.7$ (dark gray line) and $x = 0$ (light gray line). Solid lines represent stable and dotted lines unstable states.

3.4.2 DDFT Approximations and Snaking

All three approximations introduced in Sec. 3.3 have per definition identical k_c. At $\bar{\rho}_c = 0$ they also have the same value of $\alpha = \alpha_c$. To see how the approximations differ from the full model, bifurcation diagrams at $\alpha = \alpha_c$ for each of the approximations are compared while focusing on states in two dimensions. This is depicted in Fig. 3.7.

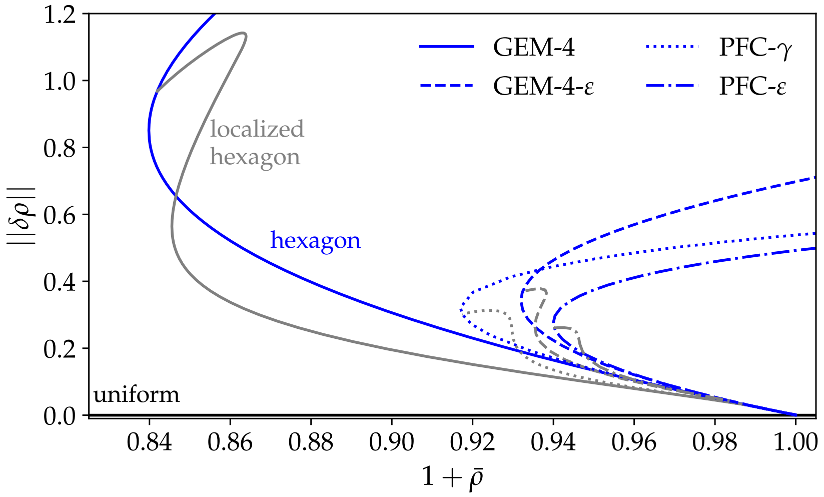

Fig. 3.7: Bifurcation diagram with the full GEM-4 model (solid lines) as well as the approximations GEM-4-ε (dashed line), PFC-γ (dotted line) and PFC-ε (dot-dashed line). The colors are chosen as in Fig. 3.4, though no stabilities are marked.

As expected, the approximations all match the full GEM-4 model at the border of linear stability, but then deviate from it relatively fast.

The GEM-4-ε approximation has its new fold at $1 + \bar{\rho} = 0.932$ as opposed to the original $1+\bar{\rho} = 0.835$. The development of the L_2-norm is similarly steep (meaning if it were rescaled to match at the fold points the curves would match fairly well), though the front of the localized state is wider, therefore the folds of the localized hexagon branch are comparatively closer together, leaving a much smaller stable region.

The PFC-γ approximation has a fold that is closer to the original than GEM-4-ε, though not by much. It is at $1+\bar{\rho} = 0.917$. The form of the branch, however, differs more as its height is compressed as compared to either previous model. The front width of the localized states is even wider than in the GEM-4-ε approximation and the snaking branch lacks even the customary two folds required to create a stable region.

Finally, the PFC-ε approximation combines the worst of both worlds. The fold point at $1+\bar{\rho} = 0.94$ is furthest away from the original one, the height compression of the curve is only marginally better than for PFC-γ and the localized states have an even wider front. The localized hexagon branch also has no folds and therefore no stable part.

To make sure the lack of snaking seen here is not a result of choosing domains that are too small as compared to the front's width, a second path continuation was performed for a much larger domain ($L_x = 30L_c$, result not shown), where there is no snaking either.

In conclusion, the approximations do not introduce snaking into the system at the parameters which match the GEM-4 model, but they do widen the fronts connecting the pattern with the uniform background to varying degrees in addition to the drawbacks already mentioned in Ref. [11].

3.4.3 The Cause of Snaking

To test which approximation causes the appearance of snaking without completely deviating from the model, the GEM-4-ε and PFC-γ approximations are analyzed for different parameter values which only preserve the position of the border of linear stability and critical values of $\bar{\rho}$ and α. From there all bifurcations and fold points are tracked through parameter space, thereby detecting the appearance of snaking in the form of additional folds that appear on the branch of localized hexagons.

For the GEM-4-ε approximation (see Eq. 3.22) the only parameter which can be varied while maintaining the border of linear stability is the curvature parameter κ. Its influence on the fold points is depicted in Fig. 3.8 a). Per definition the border of linear stability (red) is fixed at $\bar{\rho} = 0$, and the branch of hexagons (yellow) has not changed much in the studied parameter range. It moves only slightly towards lower densities with decreasing curvature κ. As for folds of the branches of localized states, the two main folds exist for $\kappa \leq 0.3$, but no additional folds appear.

A look at the accompanying bifurcation diagram (not shown) makes it clear that until $\kappa = 0.1$ no hint of snaking can be found (i.e., the branch does not wiggle at all). Beyond $\kappa = 0.1$ the numerical procedure eventually fails, as the coexisting pattern is at such high density that it lies beyond the border which marks the end of physically sensible solutions due to the appearance of negative densities. In

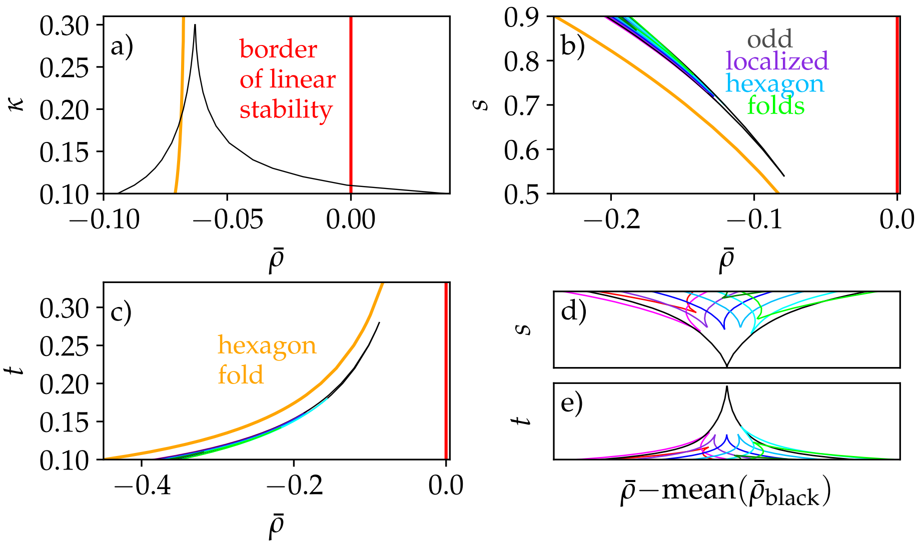

Fig. 3.8: Bifurcation and fold point continuation for a) the GEM-4-ε approximation and b)-d) the PFC-γ approximation. The former uses Eq. (3.10) with $\hat{u} = \hat{u}_\varepsilon$ given by Eq. (3.22), while varying the curvature parameter κ. The latter uses Eq. (3.23) with the original $\hat{u}$ given by Eq. (3.13), while varying the weights s and t of the quadratic [b) and d)] and cubic [c) and e)] terms, respectively. The red and yellow lines are the border of linear stability and the hexagon fold position respectively. The black lines depict the positions of the two main fold points of the odd localized states branch. Additional folds on the odd localized hexagon branch are marked through multicolored lines. d) and e) show those same odd localized state branch folds, spread out around the mean of the black lines for ease of viewing.

conclusion the snaking is not caused by approximating the interaction potential.

For the PFC-γ approximation (see Eq. (3.23)) the options for variable parameters are the prefactors s and t of the quadratic and cubic terms respectively. Their influence on the folds is depicted in Fig. 3.8 b) and c) respectively.

Again, the border of linear stability (red) is fixed at $\bar{\rho} = 0$. A more significant change appears in the position of the hexagon fold (yellow), which rises exponentially with rising s or falling t.

For the parameter s the primary folds of the odd localized hexagon branch (black) appear for values > 0.54 which then start wiggling until finally additional saddle-node bifurcations (multicolored) appear at $s > 0.7$.

The picture for t is structured similarly, with the main folds (black) appearing at $t < 0.28$ and full snaking (multicolored) appearing at $t < 0.18$. Fig. 3.8 d) and e) clarify the appearance of the snaking folds. To that end the center between the main folds (mean($\bar{\rho}_{\text{black}}$)) is used to rescale the axis, using $\bar{\rho}$-mean($\bar{\rho}_{\text{black}}$). To understand how the move towards snaking influences the density modulation field ρ of the localized states see App. A.4.

Fig. 3.9 shows an example of a bifurcation diagram with snaking at $s = 0.5$ and $t = 0.1$. Panel a) clearly shows the different position of the saddle-node bifurcation on the hexagon branch, as well as snaking of the localized state branch, while the border of linear stability is held at the expected value of $1+\bar{\rho} = 1$. Interestingly the bifurcation where the localized state branch emerges is close enough to the primary bifurcation that its position is not affected by the approximation. It remains at $1 + \bar{\rho} = 0.987$ (and $\mu \approx -0.24$). In addition, the chemical potential μ and its relation to the mean density are depicted in panel b), which shows that the snaking is indeed not slanted when plotted over μ. Instead, the folds for all but the first and last snaking ladders are on vertical lines.

Finally, panel c) shows the energy difference to the uniform ground state. While the hexagon branch behaves similarly to previous cases, the localized state (close up in the inset) now zigzags along a curve which at no point becomes the lowest energy state at the given domain size.

Panel d) shows the grand potential density difference to the uniform ground state, again similar to the previous depiction with the exception of the localized states branch, which, as seen in the inset zigzags around a single point.

3.5 Comparison to Classical Nucleation Theory

This section compares simulation results to the predictions of critical radii R^* and the accompanying energy barrier $\Delta\Omega^*$, as shown in Fig. 2.5.

To that end, first a definition for the radius R of a localized state is required, which can be calculated using densities:

$$R_d = L_y \frac{\bar{\rho}_{AB} - \bar{\rho}_A}{\bar{\rho}_B - \bar{\rho}_A} \,. \tag{3.28}$$

Here, the subscript AB denotes the nucleus or rather the localized state, while the B and A subscripts are for the crystalline and liquid state, respectively. The mean of the density modulation fields for the latter are taken where their chemical potential is $\mu_A = \mu_B = \mu_{AB}$.

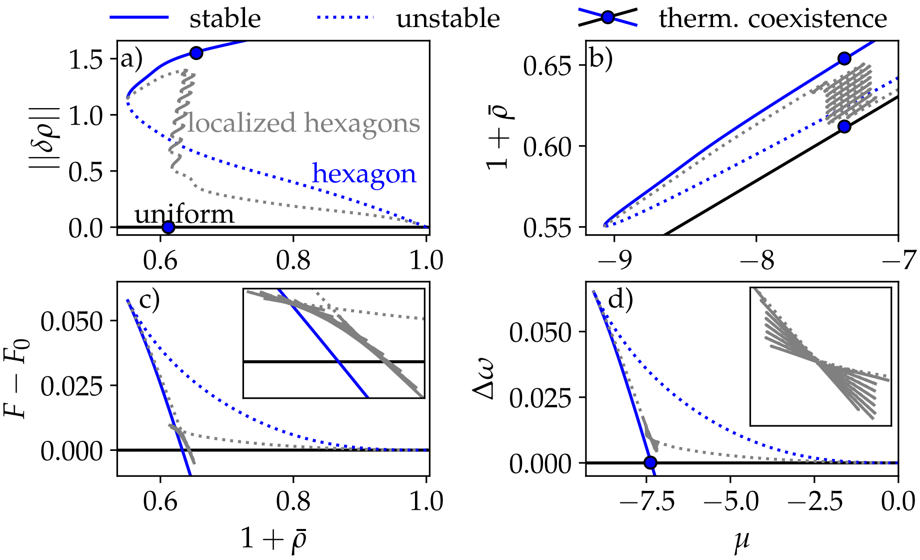

Fig. 3.9: Bifurcation diagrams for the changed PFC-γ equation (Eq. (3.23)) with $s = 0.5$ and $t = 0.1$. The colors, line and marker styles are as in previous bifurcation diagrams. It shows a) $||\delta\rho||$ as solution measure over the mean density $1+\bar{\rho}$, b) the mean density $1+\bar{\rho}$ plotted over the chemical potential μ and c) the energy difference to the uniform state $F-F_0$ as a function of the mean density $1+\bar{\rho}$, with inset of a close up of the localized hexagon branch. Panel d) shows the grand potential density difference to the liquid state $\Delta\omega$ as a function of the chemical potential μ. The crossing of the continuous lines is again marked by a filled circle and indicates that these states can coexist, allowing for the localized states. The inset shows a close up of the localized hexagon branch.

Alternatively, the radius can be estimated by looking at the actual amplitude profile of the localized state. The divide between uniform and patterned part is in fact not sharp. Instead, there is an area, the interface, which is neither flat, nor is there a fully developed pattern. The amplitude method measures the position of the outer and inner radius, R_o and R_i, defining the borders of this area.

The density of the innermost peak ρ_{inner} and the outermost part (peak or flat where applicable) ρ_{outer} are taken as reference points, while the distance between all peaks as well as the flat part are bridged by straight lines, forming a stepwise linearized front for the localized state $f_{\text{loc}}(R)$. See Fig. 3.10 for a visualization.

From there the inner and outer radii R_i and R_o are defined through setting a five

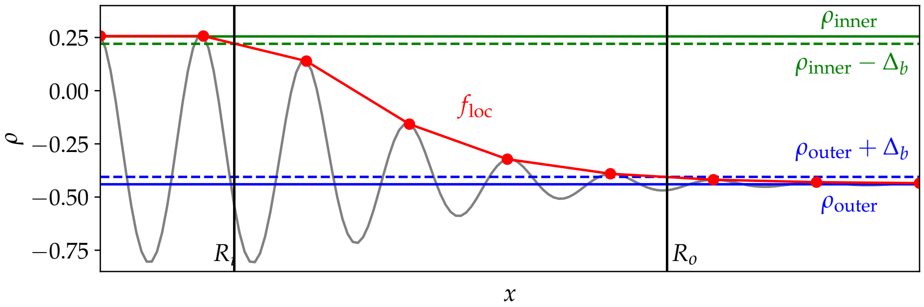

Fig. 3.10: Explanation of inner and outer radius R_i and R_o (black, solid) of a localized state profile (gray), as defined by the stepwise linearized front for the localized state $f_{\text{loc}}(R)$ (red), as well as inner maximum ρ_{inner} (green, solid) and the outermost flat density ρ_{outer} (blue, solid). The radii are given by the crossing of $f_{\text{loc}}(R)$ with the five percent deviation Δ_b from ρ_{inner} and ρ_{outer} (dashed).

percent border $\Delta_b = (\rho_{\text{inner}} - \rho_{\text{outer}}) \cdot 5\%$ and seeing where $f_{\text{loc}}(R)$ crosses it:

$$R_i = f_{\text{loc}}^{-1}(\rho_{\text{inner}} - \Delta_b) \tag{3.29}$$

$$R_o = f_{\text{loc}}^{-1}(\rho_{\text{outer}} + \Delta_b) \tag{3.30}$$

Here f_{loc}^{-1} is the inverted function of the linearized front of the localized state. The resulting mean radius is

$$R_a = \frac{R_o + R_i}{2} \,. \tag{3.31}$$

Given those radii as a first step the value of the interface energy γ is determined, by looking at the system at the coexistence point where $\Delta\Omega = a_B\gamma$ with $a_B = L_x$ (not $2L_x$ due to the reduced domain). Comparison with Eq. (2.12) leads to $\gamma_a = 0.06145$ for R_a and $\gamma_d = 0.06159$ for R_d and allows the determination of $\Delta\Omega^* = L_x\gamma$ (see Tab. 2.1, again not $2L_x\gamma$ due to the chosen domain).

From there the continuation results can be compared to $\Delta\Omega^*$. To that end the difference of the grand potential density of the localized state to the flat state $\Delta\Omega/V$ is plotted over the radius R_d (green) as measured according to Eq. (3.28) and radius R_a (gray) as measured according to Eq. (3.31) with the region bounded by the inner and outer radius R_i and R_o colored in light gray. The results are depicted in Fig. 3.11 a) for the GEM-4 model. Stable and unstable parts are once again marked in solid and dotted lines. The predicted results from the classical nucleation theory

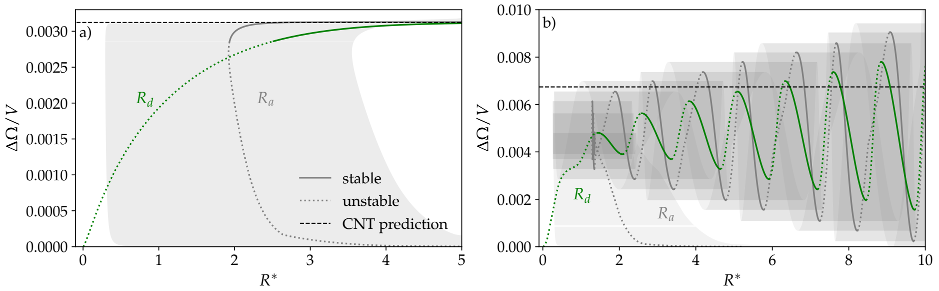

Fig. 3.11: The difference of the grand potential density of the localized state to the flat state $\Delta\Omega/V$ for a) the full GEM-4 model and b) the PFC-γ approximation with $s = 0.5$ and $t = 0.1$, plotted over the critical radius R^* as defined according to the density R_d (green, Eq. (3.28)) and radius R_a (gray, Eq. (3.31)), while the accompanying radii R_i and R_o which mark the inner and outer borders of the interface region are marked in light gray. Stable and unstable states are marked by solid and dotted lines respectively, while the theoretical prediction of classical nucleation is marked with a dashed black line.

are included as a black dashed line, the position of which is indistinguishable for either value of γ.

The most obvious conclusion is that the CNT prediction of a constant energy barrier independent of the radius is matched by the simulation results for a comparatively large range of radii. It works better for larger radii.

At small radii the continuation results do not match the theoretical prediction. In part this is because radii below a single peak radius can no longer be considered a fully formed patch of a pattern. In addition, unlike predicted, patterns do not just appear fully formed. The amplitude based radius accurately depicts that the unstable branch at low $\Delta\Omega/V$ does have a small pattern, rather than being flat. The R_d measurement predicts a smooth rise of the radius starting at $R^* = 0$ which a real system could never match and certainly does not fit the actual pattern of the localized state. Overall the amplitude-dependent radius measurement R_a is a much more accurate depiction of the real system and also matches better to CNT, while the density dependent radius calculation R_d is easier, and still close enough to be a valid approximation outside of very small radii.

Unlike the prediction in Sec. 2.3 the localized state has a stable part, which is due to the primary continuation parameter being the density rather than the chemical potential. A look at Fig. 3.6 c) easily shows that for a particle reservoir system the branch would indeed be purely unstable, as it does not contain any fold points to render it stable.

Finally, it should be noted that both CNT and the depicted simulations make the erroneous assumption of a sharp divide between liquid and patterned phase. In other words, neither theory nor data sets are completely accurate depictions of reality.

As a next step the influence of snaking on critical radii and the accompanying energy barriers is analyzed. To that end the PFC-γ approximation with $s = 0.5$ and $t = 0.1$ is subjected to the same treatment of calculating the interface energy (needed to predict the theoretical (dashed black) line), which is $\gamma = 0.133$ for both radii. Results of this procedure together with the radii and critical energy barrier are depicted in Fig. 3.11 b) with a similar color scheme as before. It also depicts the same differences to theory at low radii as in Fig. 3.11 a).

What is clearly different, however, is that rather than matching the theoretical line, the critical energy barrier forms peaks and valleys which become more pronounced with bigger radii. These differences to CNT make it clear that the theory is not suitable for predicting nucleation in systems with snaking behavior.

In addition, due to the snaking there are now stable solutions even for the particle reservoir system. This matches the implication of the peak and valley structure, namely that some radii have a lower energy barrier (valley points), making them easier to reach, while the surrounding peaks mean that going from there to another radius takes some additional energy.

4 Localized States in an Active Model

The following results are under consideration to be published, a pre-print version can be found in Ref. [82]. The system was first studied in the doctoral thesis of M. Holl [80]. All data shown in Figs. 4.1 to 4.6 have been re-calculated and in most cases completed (they are marked accordingly). All data in Sec. 4.4, which focuses on 2D rotating crystallites, is completely new.

4.1 Motility-Induced Phenomena in Active Soft Matter Models

Unlike passive soft matter systems, where stability of states is directly connected to a minimum in the free energy landscape, active soft matter models are typical examples of non-equilibrium phase transitions. Here, the energy enters the system via an external field. The energy influx makes the free energy F insufficient to determine optimal phases, instead methods such as structural entropy maximization have to be applied [12].

One focus of studying phase transitions in active soft matter is motility-induced phase separation (MIPS), i.e., the crossing of a density-dependent threshold beyond which self-propelled particles separate into dense and dilute fluid phases reminiscent of a liquid-like cluster coexisting with a gas-like phase [152, 156, 118, 35, 121, 64, 167]. Such clusters can be observed experimentally [118, 30, 15] as well as in particle-based simulations [53, 128, 140, 43, 33] and continuum models mainly based on nonvariational amendments [193, 170, 169, 154, 19, 18] of the Cahn-Hilliard model for phase decomposition [28] with consistent results for their properties [19].

Additionally, simulations and experiments yield active crystallites, i.e., resting, traveling or rotating crystalline structures within a fluid background [180, 30, 128, 138, 143, 15, 199, 142, 61]. They are also called finite-size active solids [71, 77, 55, 117] and often modeled using an active version [124, 125, 36, 2, 133, 149, 134, 135, 83] of the passive PFC model [49, 51, 182], which is a versatile microscopic field theory for colloidal crystallization and a local approximation of a Dynamical Density Functional Theory (DDFT) [11, 188].

The active PFC model is capable of modeling the transition from resting to traveling space-filling crystalline states [124], as well as active crystallites [133, 135, 83]. However, it fails to describe proper motility-induced crystallization (MIC). In other words, a crystalline structure found in the passive model [182, 174] is subdued by the addition of activity, which results in either the destruction of the crystal or the addition of translation, rotation or oscillation [134].

As a further downside, the active PFC model does not distinguish between different fluid phases, therefore, there is neither a liquid-gas transition nor is the interplay of condensation and crystallization considered.

4.2 The Extended Active PFC Model

This section introduces a model which attempts to mitigate both of the shortcomings of the standard active PFC model mentioned above. This includes the passive form, as well as two different types of activity: density-independent and density-dependent. Linear stability is analyzed for all three cases.

4.2.1 Model Introduction

The extended active PFC model is derived from two different theories. One part is an extended PFC-type equation (ePFC) of higher order (i.e., three- and four-point direct correlation functions). Its parameters are chosen with the specific aim of modeling three distinct phases, vapor, liquid and solid, as well as phase transitions and coexistence between them [190]. It has the free energy

$$\begin{aligned} F_{\text{ePFC}} = &\int -B_0\rho - \frac{1}{2}\rho(C_0 + C_2\Delta + C_4\Delta^2 + 16\Delta^3)\rho \mathrm{d}r \\ &+ \int \frac{1}{3!}(9\rho^3 + 34.2\rho^2\Delta\rho) + \frac{1}{4!}(6\rho^4 + 52.1\rho^2(\Delta\rho)^2)\mathrm{d}r \end{aligned} \tag{4.1}$$

with the (scaled and shifted) density field ρ and parameters as described in Tab. 4.1. The rescaled and shifted effective temperature T enters through those parameters, making it a second control parameter in addition to the mean density $\bar{\rho}$.

B_0	C_0	C_2	C_4
$-4.5 - 3T$	$-5.764 - T$	$17.8 + 2T$	$39.8 - T$

Table 4.1: Parameter values for the temperature dependent parts of the extended PFC model according to Ref. [190].

Both the vapor and the liquid phase are uniform and differ only in their densities. The solid takes the form of a spatially periodic pattern. In its passive form the model already captures the liquid-gas transition, as well as liquid-solid and gas-solid transitions.

The active component resulting from self-propulsion enters the model by way of a polarization field **P**, detailing the local strength and direction of the polar order (cf. [124, 125]). The free energy used here takes the form

$$F_P = \int \frac{1}{2}\mathbf{P}^2 \mathrm{d}r\,, \tag{4.2}$$

as in, e.g., Ref. [133].

The polarization field **P** and density field ρ are non-reciprocally connected (right most terms in Eqs. (4.3) and (4.4)), which breaks the overall gradient dynamics structure, thereby indicating sustained non-equilibrium influences such as chemo-mechanical driving. They are ultimately responsible for all occurring moving and oscillating states.

$$\partial_t \rho = \Delta \frac{\delta F_{\mathrm{ePFC}}}{\delta \rho} - \nabla v(\rho)\mathbf{P} \tag{4.3}$$

$$\partial_t \mathbf{P} = \Delta D_c \frac{\delta F_P}{\delta \mathbf{P}} - D_{nc}\frac{\delta F_P}{\delta \mathbf{P}} - \alpha \nabla v(\rho)\rho\,, \tag{4.4}$$

with the parameters in Tab. 4.2.

D_c	D_{nc}	α
0.2	0.5	0.5

Table 4.2: Parameter values for the polarization field and coupling of the active PFC model, chosen according to Refs. [124, 80].

The coupling strength, i.e., the self-propulsion speed of the active particles, is given by $v(\rho)$. It is often assumed constant ($v = v_0$) [124, 133], representing an effective speed of individual particles. However, in this thesis the density-dependent expression $v = v_0 - \zeta\rho$ is used, which often appears in effective hydrodynamic models for MIPS [170, 169, 18]. It accounts for the force imbalance related to the self-trapping of particles due to interactions in dense regions. Note that v_0 might take on negative values, due to the scaling and shifting of ρ away from the proper density ρ' [18]. In that case ζ remains a positive constant as in a ρ'-based model. This thesis takes the symmetry of Eqs. (4.5) and (4.6) into account, which implies identical behavior for $v_0 < 0, \zeta > 0$ and $v_0 > 0, \zeta < 0$, with only a change in the direction of the polarization (i.e., $\mathbf{P} \to -\mathbf{P}$).

The remaining terms in Eq. (4.4) correspond to translational and rotational diffusion, which are conserved and non-conserved gradient dynamics, respectively.

The full form of the model is:

$$\begin{aligned}\partial_t \rho = \Delta\Big[&-(C_0 + C_2\Delta + C_4\Delta^2 + 16\Delta^3)\rho \\ &+ \frac{9}{2}\rho^2 + \frac{57}{10}(2\rho\Delta\rho + \Delta(\rho^2)) \\ &+ \rho^3 + \frac{521}{120}(\rho(\Delta\rho)^2 + \Delta(\rho^2\Delta\rho))\Big] - \nabla v(\rho)\mathbf{P} \qquad (4.5)\\ \partial_t \mathbf{P} = D_c&\Delta\mathbf{P} - D_{nc}\mathbf{P} - \alpha\nabla v(\rho)\rho\,. \qquad (4.6)\end{aligned}$$

In combination the system captures the destruction of passive clusters as the earlier active PFC model as well as MIC and MIPS [80].

In the following the thesis analyzes its phase behavior in passive (thermodynamic) and active cases thereby focusing on the destruction of passive clusters (drops and crystallites) and the emergence of active ones. Finally, the emerging rotating crystallites are analyzed.

4.2.2 Linear Stability Analysis

The linear stability of a one dimensional uniform steady state $(\bar{\rho}, 0)^T$ of a two field model requires a vectorial perturbation, where the components take the form introduced in Eq. (2.4), i.e., $\delta = (\delta\rho, \delta P)^T \propto e^{i\mathbf{kx}+\sigma t}$ (cf. [80]).

Introducing $(\bar{\rho}, 0)^T + \delta$ into Eqs. (4.5) and (4.6) results in a two dimensional eigenvalue problem

$$\sigma\delta = \underline{\mathbf{J}}\delta \qquad (4.7)$$

with Jacobian

$$\underline{\mathbf{J}} = \begin{pmatrix} J_\rho & -ik(v_0 - \zeta\bar{\rho}) \\ -ik\alpha(v_0 - 2\zeta\bar{\rho}) & J_P \end{pmatrix} \qquad (4.8)$$

where J_ρ and J_P are the dispersion relations of the uncoupled Eqs. (4.5) and (4.6), respectively:

$$J_\rho = \left(C_0 - 9\bar{\rho} - 3\bar{\rho}^2\right)k^2 - \left(C_2 - \frac{114}{5}\bar{\rho}\right)k^4 + \left(C_4 - \frac{521}{120}\bar{\rho}^2\right)k^6 + 6k^8 \qquad (4.9)$$

$$J_P = -(D_c k^2 + D_{nc})\,. \qquad (4.10)$$

The two branches of the full dispersion relation are given by

$$\sigma_\pm = \frac{1}{2}\left[J_\rho + J_P \pm \sqrt{(J_\rho + J_P)^2 - 4\det(\underline{\mathbf{J}})}\right] \tag{4.11}$$

with the determinant of the Jacobian

$$\det(\underline{\mathbf{J}}) = J_\rho J_P + k^2\alpha[v_0^2 + 2(\zeta\bar\rho)^2 - 3v_0\zeta\bar\rho]\,. \tag{4.12}$$

Note that changing the sign of $v = v_0 - \zeta\rho$, i.e., changing the sign of both v_0 and ζ has no effect on σ.

As the bigger eigenvalue σ_+ dictates the actual growth rate, which is given by $\mathrm{Re}(\sigma_+)$ and depends on the wavenumber k. The frequency of the harmonic modes is given by $\mathrm{Im}(\sigma)$, also depending on k. As long as $(J_\rho - J_P)^2 > 4k^2\alpha[v_0^2 + 2(\zeta\bar\rho)^2 - 3v_0\zeta\bar\rho]$ it is $\mathrm{Im}(\sigma) = 0$.

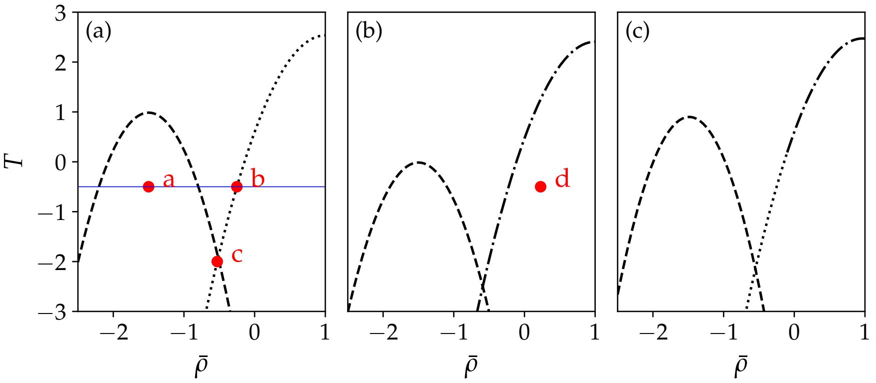

Fig. 4.1: Spinodals, i.e., the stability thresholds of uniform states, of the extended active PFC model Eqs. (4.5) and (4.6) in the $(\bar\rho, T)$-plane (black lines). The parameters are a) $v_0 = 0$, $\zeta = 0$ (passive limit) b) $v_0 = 1$, $\zeta = 0$ and c) $v_0 = 1$, $\zeta = -0.5$. Dashed, dotted, and dash-dotted lines respectively mark the instability type: large-scale, stationary (Cahn-Hilliard), small-scale, stationary (conserved-Turing), and small-scale oscillatory (conserved-wave). All three panels show a codimension-2 point where the onset of large- and small-scale instability coincides, i.e., the spinodals cross. Red dots mark positions of dispersion relations shown in Fig. 4.2, while the blue line matches the parameters in Fig. 4.3.[1]

Fig. 4.1 shows the stability thresholds of the uniform state in the $(\bar\rho, T)$-plane for a) $v_0 = 0$, $\zeta = 0$ (passive limit) b) $v_0 = 1$, $\zeta = 0$ and c) $v_0 = 1$, $\zeta = -0.5$.

---

[1] Re-calculated from Ref. [80] and instability types amended.

They are categorized according to Ref. [60]: Regardless of the parameter choice, all cases show liquid-gas phase separation, marked by a dashed line. It results from a Cahn-Hilliard instability (stationary, large-scale, conserved system). They appear for temperatures $T < T_c$, which is roughly equal in panel (a) and (c) at $(\bar{\rho}_c, T_c) \approx (-1.5, 1)$ but lower in (b) $(\bar{\rho}_c, T_c) \approx (-1.5, 0)$. In other words, the density-independent activity suppresses phase separation by shifting the critical point and the entire spinodal to lower temperatures while the density-dependent activity fosters phase separation by reversing the shift and therefore leading to MIPS.

Crystallization also occurs for all parameters. The accompanying instability is either a conserved-Turing instability (stationary, small-scale, conserved system) as in panel (a) and (c) (for lower T), or a conserved-wave instability (oscillatory, small-scale, conserved system) in panel (b) and (c) (for higher T). They are marked by dotted and dot-dashed lines, respectively. In contrast to the phase-separation stability threshold, the crystallization spinodals barely move, meaning potential occurrences of suppression or fostering of MIC will be decided by the nonlinear behavior (see Fig. 4.6).

There is a codimension-2 point at $(\bar{\rho}, T) \approx (-0.5, -2)$, where large- and small-scale instabilities occur simultaneously, i.e., where the spinodals cross.

Dispersion relations matching the different types of instabilities, as well as the codimension-2 point are depicted in Fig. 4.2. There the real parts of σ are depicted as black lines in case of purely real eigenvalues or as red dashed lines if $\mathrm{Im}(\sigma) \neq 0$.

Panel (a) gives an example at $T = -0.5$, and $\bar{\rho} = -0.5$, which is well above the onset of a Cahn-Hilliard instability. At the onset $k = 0$ would appear as the mode with the largest growth rate, here however, the eigenvalue at $k = 0$ remains zero and there is an adjacent band of unstable wavenumbers. In time evolutions, this gives rise to large-scale structures, specifically, a phase-separated state.

Panel (b) shows an example at the same temperature as panel (a), i.e., $T = -0.5$, but at a higher mean density $\rho = -0.2515$. This is only slightly above the onset of a conserved-Turing instability, meaning there is a small band of wavenumbers close to $k \approx 1.1444$ which is unstable. Directly at onset and barring further nonlinear influences, a time evolution will give rise to a spatially periodic state, i.e., a crystal.

Panel (c) shows a dispersion relation close to the codimension-2 point in the passive case at $T = -2$ and $\bar{\rho} = -0.52895$. There, both the large-scale and the small-scale instability, occur simultaneously. There are two bands of unstable wavenumbers: one adjacent to $k = 0$ and the other around $k_c \approx 1.1533$. While nonlinear effects make predicting the outcome of a time simulation from linear stability analysis

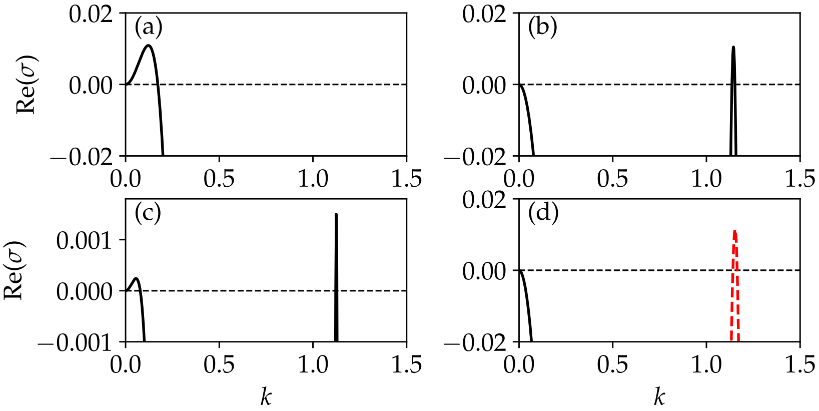

Fig. 4.2: Examples of dispersion relations of the extended active PFC model in Eqs. (4.5) and (4.6). Purely real eigenvalues are represented by black solid lines, complex eigenvalues are represented by a red dashed line. Dispersion relations are given at (a) $\bar{\rho} = -1.5$, $T = -0.5$, and $v_0 = 0$, (b) $\bar{\rho} = -0.2515$, $T = -0.5$, and $v_0 = 0$, (c) $\bar{\rho} = -0.52895$, $T = -2.$, and $v_0 = 0$ and (d) $\bar{\rho} = 0.229$, $T = -0.5$, and $v_0 = 1$. Panels (a)-(c) show monotonic instabilities corresponding to (a) a Cahn-Hilliard instability, (b) a small-scale (conserved-Turing) instability and (c) a case close to the codimension-2 point, where the small-scale and the large-scale stationary instabilities occur simultaneously. Panel (d) shows an active case. The resulting dispersion relation corresponds to an oscillatory small-scale (conserved-wave) instability.[2]

impossible, the competition between the instabilities is a first indicator for the existence of three-phase (vapor-liquid-solid) coexistence.

Finally, panel (d) shows a dispersion relation for an active case at $v_0 = 1$, as well as $\bar{\rho} = 0.229$ and $T = -0.5$. It shows a small-scale instability, which unlike the one in panel (b), features complex eigenvalues, meaning the instability is oscillatory, i.e., a conserved-wave instability. Barring additional nonlinear effects, a time evolution would produce a traveling periodic state, i.e., a traveling crystal.

---

[2] Re-calculated from Ref. [80].

4.3 Bifurcations in One Dimension

In this section an example of a bifurcation diagram of the passive extended PFC model (i.e., for $v_0 = \zeta = 0$) at $T = -0.5$ is presented for a one-dimensional domain of size $L = 100$ with $N = 256$. The bifurcation diagram is depicted in Fig. 4.3

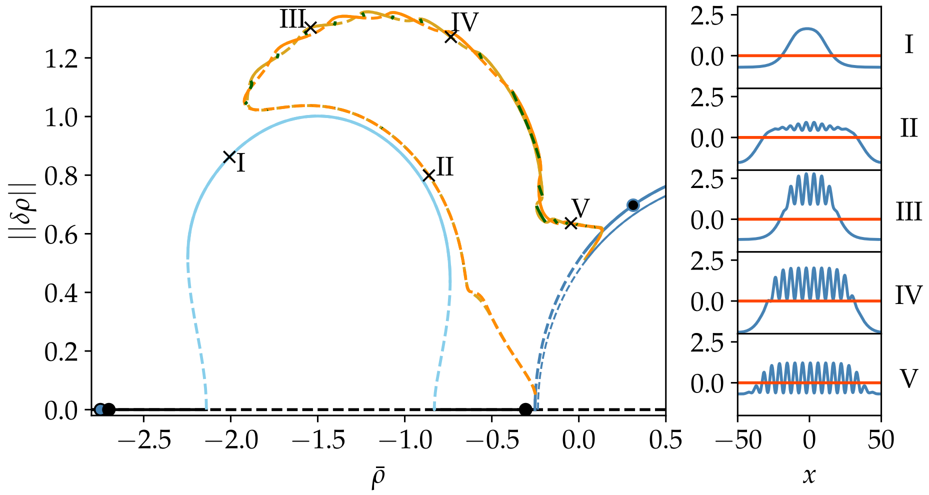

Fig. 4.3: Bifurcation diagram at fixed $T = -0.5$ for $v_0 = \zeta = 0$, given as a function of the mean density $\bar{\rho}$ for a 1D domain of size $L = 100$. The resulting branches of steady states are characterized by their L_2 norm $||\delta\rho||$, while solid [dashed] lines indicate linearly stable [unstable] states. Black branches represent uniform states (gas or liquid), light blue states are phase separated states, i.e., states with gas-liquid coexistence, while the thick [thin] dark blue line corresponds to domain-filling crystalline (periodic) states with 18 [19] peaks. The intertwined dark and light orange lines represent branches of localized states with odd and even peak numbers, respectively, featuring predominantly crystal-gas coexistence. The interconnecting branches in dark green represent asymmetric localized states. The four filled circles indicate two pairs of binodal points, with the colors indicating the respective coexisting state, specifically, the fully black circles are coexistence between two uniform states, while the dark blue and black combination indicates gas-crystal coexistence. The crosses mark states depicted in panels I to V, which show density profiles $\rho(x)$ in blue and the polarization $P(x)$ in dark orange.[3]

---

[3] Re-calculated from Ref. [80], panel I-V adapted.

depending on $\bar{\rho}$ and characterized by the L_2 norm $||\delta\rho||$ (cf. Eq. (3.27)). It matches the horizontal cut through the phase diagram in Fig. 4.1 (a).

The uniform state has $||\delta\rho|| = 0$. At low $\bar{\rho}$ it is considered a gas, for higher $\bar{\rho}$ a liquid. Its accompanying branch (black) exist for all $\bar{\rho}$. Starting from low $\bar{\rho}$ the state is stable, but then loses stability in a subcritical pitchfork bifurcation at $\bar{\rho} \approx -2.140$ and regains it at the same way at $\bar{\rho} \approx -0.830$. Finally, the branch destabilizes at $\bar{\rho} \approx -0.251$ in a supercritical pitchfork bifurcation. They match the Cahn-Hilliard instabilities and conserved-Turing instability presented in Fig. 4.1 (a), respectively.

The two lower $\bar{\rho}$ bifurcations connect through a branch of phase-separated states (light blue), where liquid and gas coexist as predicted by the crossing of the black solid line with itself in Fig. 4.4 (b) at $(\mu, \omega) \approx (1.854, -0.15)$. The coexisting states are marked with black circles. The phase-separated branches both emerge subcritically and are unstable, however, they gain stability at saddle-node bifurcations at $\bar{\rho} \approx -2.247$ and $\bar{\rho} \approx -0.739$, respectively. Between them the branch is linearly stable, with an example profile given in Fig. 4.3, panel I. That same stable part follows parts of the Maxwell line, which connects the two coexisting states, and matches the upper thin dotted horizontal line (at $\mu \approx 1.854$) in Fig. 4.4 (a).

The supercritical bifurcation at $\bar{\rho} \approx -0.251$ gives rise to a branch (dark blue, thick) of domain-filling periodic states with 18 peaks, which is initially stable, but destabilizes at $\bar{\rho} \approx -0.249$ in a secondary subcritical pitchfork bifurcation, which results in two branches of localized states (with odd and even peak numbers, orange). A second branch of domain-filling periodic states with 19 peaks (dark blue, thin) emerges from the uniform state in a supercritical bifurcation at $\bar{\rho} \approx -0.239$. It starts out unstable, but stabilizes when the branches of localized states reconnect with it at $\bar{\rho} \approx 0$ in another pitchfork bifurcation.

The localized states are a result of coexistence between a 18 peak crystalline state and a uniform state, as indicated by the crossing of their respective branches in Fig. 4.4 (b) at $(\mu, \omega) \approx (1.675, -0.15)$.

Both the odd (dark orange) and even (light orange) states are unstable when their branches emerge from the 18 peak branch. They approach and then closely follow the stable part of the branch of phase-separated states. The localized states on this part of the branch resemble a phase-separated state with a comparatively small periodic modulation on the high-density plateau, which therefore matches coexistence between gas and a weakly modulated crystal state (cf. Fig. 4.3, panel II).

The localized state branches veer off from the phase-separated branch shortly after passing its maximum. From there at $\bar{\rho} \approx -1.9$ they fold back toward larger $\bar{\rho}$ by way of two saddle-node bifurcations. The odd localized state branch gains stability

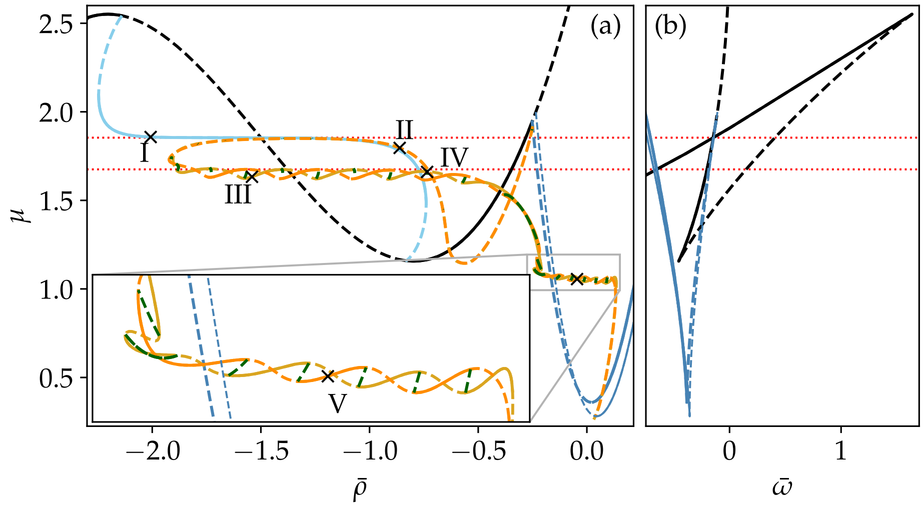

Fig. 4.4: Chemical potential μ given as a function of (a) the mean density $\bar{\rho}$ and (b) the mean grand potential $\bar{\omega}$ for states depicted in Fig. 4.3. All parameters, line styles and symbols match accordingly. (b) only shows branches of domain filling states. Intersections of branches of stable states in panel (b) indicate a coexistence of states in the thermodynamic limit by way of Maxwell (binodal) points. They are marked by filled circles in Fig. 4.3 and their μ values indicated by the horizontal red dotted lines, which indicates the position of the Maxwell line in (a) that coexisting state branches follow. Note that at $\mu \approx 1.2$ a near intersection exists in (b), causing the snaking of branches magnified in the inset of (a).[4]

at that point, while its even counterpart remains unstable. However, they exchange stability through a series of pitchfork bifurcations, giving rise to short asymmetric localizes state branches (dark green), connecting both branches. An example of such an asymmetric state can be found in Fig. 4.3, panel IV. Gas-crystal coexistence for an even state can be found in panel III. Both states are sufficiently close to the triple point (at $(\bar{\rho}, T) \approx (-0.379, -0.271)$) such that they also exhibit hints of “liquid shoulders” between the gas and the crystal phase. Together, the localized state branches form a typical snake-and-ladder structure of slanted homoclinic snaking found in many systems with mean density conservation [182, 97, 83]. It follows the Maxwell line for a limited density range, as shown in Fig. 4.4 (a) (lower red dotted line). If the chemical potential were used as control parameter the snaking would become vertically aligned (cf. Fig. 4.4 (a) when rotated by 90 degree and the discussions in [182, 83]).

---

[4] Re-calculated from Ref. [80] and re-arranged.

Fig. 4.4 (a) shows another distinct snaking structure at $\mu \approx 1.06$, which is magnified in the inset. It is caused by a "ghost-binodal", i.e, the near miss of coexistence between the liquid and crystalline state, as indicated by the close proximity of the saddle-node bifurcation where solid and dashed black lines meet, and the blue solid line in Fig. 4.4 (b).

In 4.3 the second snaking structure is situated on the near horizontal part of the localized state branches close to where they reconnect with the crystalline branch. Profile V consequently shows a clear liquid-solid coexistence.

The two distinct snaking structures (solid-liquid and solid-gas) are separated by a pair of saddle-node bifurcations, which can be found at $\bar{\rho} \approx -0.218$ and $\bar{\rho} \approx -0.230$ for the odd and at $\bar{\rho} \approx -0.210$ and $\bar{\rho} \approx -0.243$ for the even branch of localized states.

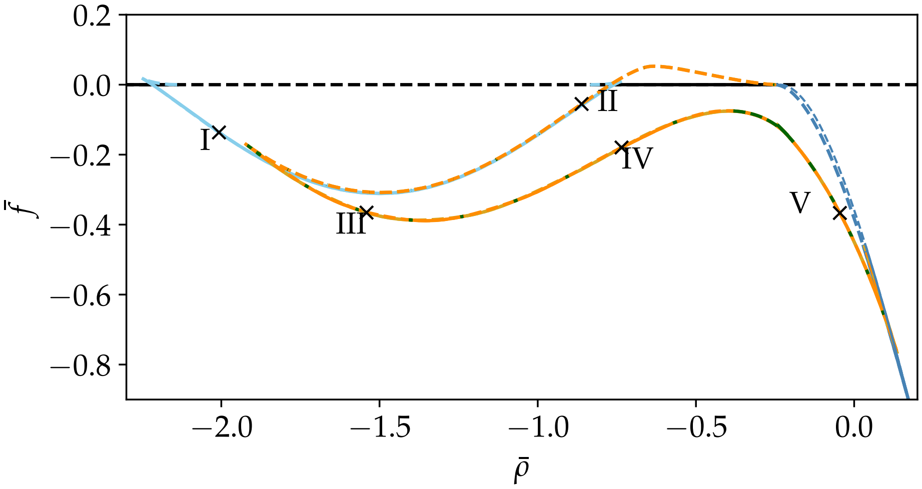

Fig. 4.5: Relative mean free energy density $\bar{f}$ for all states depicted in Fig. 4.3, shown in dependence of $\bar{\rho}$. All parameters, line styles and symbols match accordingly.[5]

Energetically, going from low to high $\bar{\rho}$ the gas starts as the most favorable state, followed by the phase-separated states shortly after passing the left saddle-node bifurcation (above $\bar{\rho} \approx -2.218$) up until $\bar{\rho} \approx -1.829$. After that the branches of odd and even localized states alternately form the global minimum, spanning the region between $\bar{\rho} \approx -1.829$ and $\bar{\rho} \approx 0.103$. At larger densities the domain-filling crystal with 19 peaks corresponds to the state of lowest energy. This is shown in Fig. 4.5.

---

[5] Re-calculated from Ref. [80].

The part of the localized states branches which is both unstable and closely matched to the linearly stable phase-separated branch has slightly higher energy than its phase-separated companion. Therefore, it represents the threshold states which the system is required to overcome in order to reach the stable localized states when starting from the metastable phase-separated state.

In summary the extended PFC model both matches the phase diagram and combines structures from both Cahn-Hilliard and PFC models as intended.

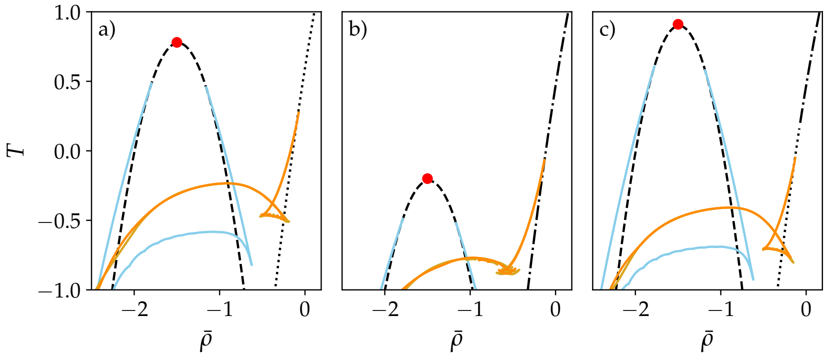

Fig. 4.6: Spinodals (i.e., linear stability borders) and binodals (i.e., loci of outermost saddle-node bifurcations) tracked through the $(\bar{\rho}, T)$−plane for a system with $L = 100$ and $N = 256$, as well as a) $v_0 = 0$, $\zeta = 0$ b) $v_0 = 1$, $\zeta = 0$ and c) $v_0 = 1$, $\zeta = -0.5$. Spinodal are given as black dashed and dotted lines, which denote the Cahn-Hilliard and conserved-Turing instabilities respectively, while the dot-dashed lines indicate a conserved-wave instability. The red dot marks the critical point of the gas-liquid spinodal. For the binodals (colored lines) only stationary solution branches are tracked. Colors match the branches of the saddle-node bifurcations in Fig. 4.3. [6]

Given the present bifurcation diagram, continuation of the outermost saddle-node and primary pitchfork bifurcations through the (ρ, T)−plane gives the binodals of the system. They are depicted in Fig. 4.6 for the same parameters as Fig. 4.1, i.e., for a) $v_0 = 0$, $\zeta = 0$ b) $v_0 = 1$, $\zeta = 0$ and c) $v_0 = 1$, $\zeta = -0.5$ with matching line styles, however, the spinodals are now adapted for a system of size $L = 100$, which shifts them slightly from where they are in Fig. 4.1.

---

[6] Re-calculated from Ref. [80], spinodals adapted to finite size with stability types amended.

To match the colors of the bifurcation diagram, the loci for the gas-liquid coexistence are shown in light blue and branch off from the spinodal representing the Cahn-Hilliard instability. The remaining colored lines represent the loci of the outermost saddle-node bifurcations for the branches of localized states of odd (dark orange) and even (light orange) number of peaks. They are nearly on top of each other and show complex structures, some of which are explained by the discussion above. While additional traveling states exist for the active cases shown in (b) and (c) (not shown) they do not have a significant impact on the overall size of the coexistence region.

The triple point should be located in the swallow tail formed structure, where different parts of the lines correspond to different coexistences with the crystal state.

This is also where it becomes obvious that adding a density-independent activity not only lowers the gas-liquid spinodal (critical point marked by the red dot) and accompanying binodals, but also affects the crystallization process beyond changing the instability from conserved-Turing to conserved-wave. The whole crystal-gas binodal, including swallow tail structure are lowered significantly from its passive counterpart. Adding a density-dependent activity, however, not only lifts the gas-liquid spinodal and binodals to higher T values, but also, to a lesser extent the liquid-solid binodal, therefore accounting for both MIPS and MIC.

4.4 Rotating Localized States in Two Dimensions

Rotating crystallites are an intriguing state, appearing in many experimental systems [77, 143, 175, 195]. Here they are simulated for a system with $v_0 = \zeta = 1$ using a semi-implicit Euler method on a periodic boundary domain of length $L_x = L_y = 100$, with a discretization of $N_x = N_y = 256$. Starting from an initial condition of a rotating localized state with six fold rotational symmetry, the existence range of those same structures, as well as their radius R and angular velocity ω is tracked for densities $\bar{\rho} = -0.2$ to $\bar{\rho} = -0.45$ as a function of both T and R. The results are depicted in Fig. 4.7. Generally the crystalline clusters show a hexagonal or near hexagonal shape which rotates as a rigid body, i.e., with identical group and phase velocity. Odd and even states rotate around a central peak or valley, respectively.

The radius is calculated using a time average, then taking a slice at $y = 0$ and then measuring at which point $\rho(x, 0)$ first reaches a threshold value A when starting from the outer edge and moving in. A is defined as the difference of the highest peak density ρ_h and the background density ρ_b multiplied by a percentage p, i.e.,

$A = (\rho_h - \rho_b)p$. For odd localized states $p = 0.75$ is used. For even localized states it is $p = 0.65$, so as to compensate that there is no central peak, which lowers the value of ρ_h when averaging over time. The x-value where A is passed gives the cluster radius R.

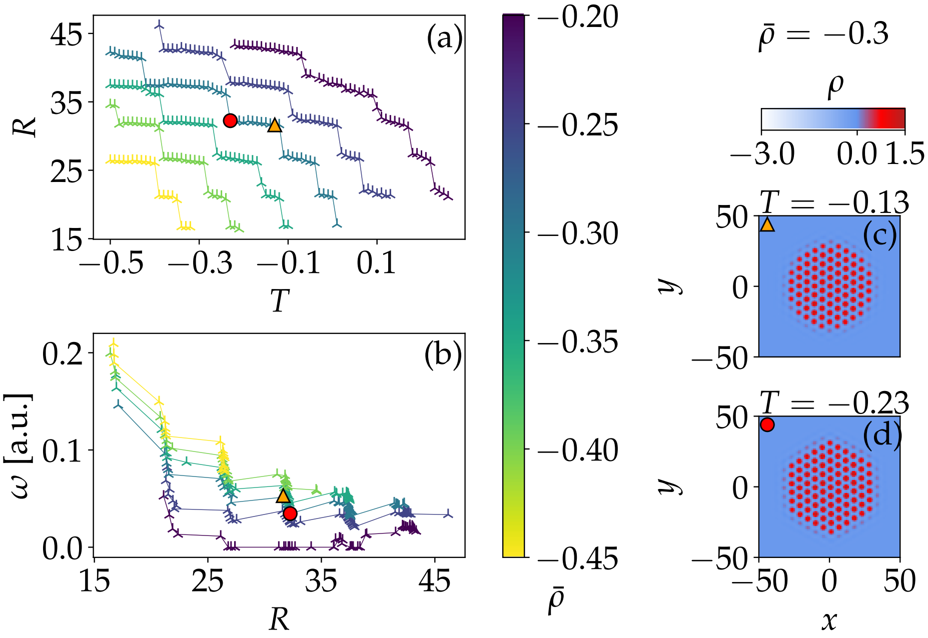

Fig. 4.7: Characteristics of rotating crystallites: (a) Radius R of the rotating localized structures depending on the temperature T. (b) Angular velocity ω in degree per time unit depending on the radius R. In both (a) and (b) results are given for several fixed mean densities $\bar{\rho}$ as indicated by the colorbar. Example profiles from two ends of a plateau state for $\bar{\rho} = -0.3$ are depicted in (c) and (d). Their exact placement in (a) and (b) is marked by an orange triangle and red circle, respectively. The system is at $v_0 = \zeta = 1$ with a domain of $L_x = L_y = 100$ and a discretization of $N_x = N_y = 256$.

Fig. 4.7 (a) shows the radius R of the rotating localized states depending on the temperature T. It has the appearance of a staircase that goes up with decreasing T, even as the step length increases. The step height, however, is roughly equal for all presented mean densities, which are indicated according to the colorbar. The near horizontal part of each step is indicative of a constant radius, with only slight alterations as exemplified in the density fields in Fig. 4.7 (c)-(d) (marked by orange triangle and red circle, respectively). They show two different states on the same plateau at $\bar{\rho} = -0.3$, i.e., with similar radii, the only difference being that with falling T the initially incomplete outer shell of the hexagonal structure laterally grows more peaks until the shell is completed, at which point a new outer layer is initiated by peaks in the central part of each face. The new layer initiates the jump in R, leading to a step-like form.

The stairs can also be taken as an indication of snaking behavior, which is a common feature of localized structures [29, 97]. In consequence, a certain level of hysteresis between the different plateau solutions can be assumed which is not captured in this figure.

Generally, lower mean densities can be found at lower values of T even as the overall form of the stairs stays the same. The maximum radius is close to $R = 45$, with higher radii excluded from the analysis as the localized states would then start to interact with themselves via periodic boundary conditions, leading to different patterns appearing, such as (traveling) holes within a (traveling) pattern. Similarly there is a lowest possible radius slightly above $R = 16$. It marks the lowest possible amount of seven peaks (one center six around) which is required to form a stable localized state. Lower densities lead to a breakdown of the localized structure in favor of a uniform state. For the higher mean densities $\bar{\rho} = -0.2$ and $\bar{\rho} = -0.25$ the lowest radius is even higher at $R = 21$, which is due to the softening of the boundary between uniform background and pattern. The boundary is very steep at lower temperatures, but wider for higher values, therefore leading to a requirement of more than the minimum of seven peaks for a localized state.

Fig. 4.7 (b) shows the angular velocity ω of the localized states in degree per time unit. Overall, low radius states are faster than high radius states, with a sharp decline for very small states. Beyond that, each radius plateau shows a change in angular velocity, with the angular velocity for fully filled out hexagon states lower than for states with an incomplete shell. Note that for the largest $\bar{\rho}$ the clusters seem to remain at rest in an intermediate parameter range.

Generally, lower mean densities lead to lower angular velocities at the same radius. The $\bar{\rho} = -0.2$ states are a special case, as they have the lowest angular velocity. This is further lowered for a complete outer shell, at which point they come to rest.

In addition to the discussed odd and even states, asymmetrical states (with the radius bigger in two directions than in others) also exist. They can be the only stable rotating state, but are not included in Fig. 4.7, as their radius is no longer easily defined. As a further complication the group and phase velocity diverge for the outermost peaks of the longer axis, effectively destroying the rigid body rotation.

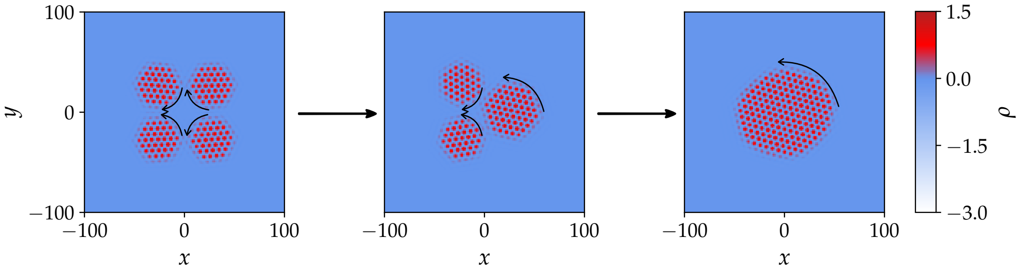

Fig. 4.8: A cluster of several rotating states at $\bar{\rho} = -0.3$ is depicted as a density field for $T = 0$. Left pane: rotating states move both with and against the clock as indicated by the arrows, with the local density given by the colors in the colorbar. The edges of states brush against each other during rotations, but do not visibly disturb their form or speed for comparatively long time scales. Middle: Two rotating states collapsed into one, forming a bigger rotating localized state, again edges interact with other states which after comparatively low time leads to the right panel, where all states collapsed into one localized patch. The domain is $L_x = L_y = 200$, with a discretization of $N_x = N_y = 512$.

Fig. 4.8 (left panel) shows a cluster of several rotating states in close proximity, two of which move with, the other two against the clock. The rotating hexagons are close enough that their edges interact during rotation, though without visibly hindering the individual rotation for a comparatively long time. However, eventually the state collapses first into three (middle) and finally one (right) localized structures.

Finally, in Fig. 4.9 there are additional localized states depicted for more extreme parameter regions, i.e., at low $\bar{\rho}$ and T. They show a rich variety of intricate behavior, including a stripe phase (in analogy to the standard active PFC model [124]) which corresponds to particles that are periodically placed in one direction but are mobile in the other. The newly resulting localized structures, shown in Fig. 4.9, feature combinations of local stripe and crystalline arrangements (two-phase cluster) or pure stripe phase, in addition to the previously discussed pure crystal phase. In consequence, they often are of lower symmetry and due to the activity the entire cluster or just parts of it may move in different ways.

Fig. 4.9 (a) shows an elongated hexagonal crystallite swinging like a torsion pendulum, implying a periodic reversal of the polarization field. (b) shows a slowly rotating two-phase crystallite in the form of a hexagon patterned bow tie shape surrounded by stripes. The bow tie structure does a kind of bouncing motion. (c) depicts a two-phase crystallite of shaking stripes surrounding a resting hexagon

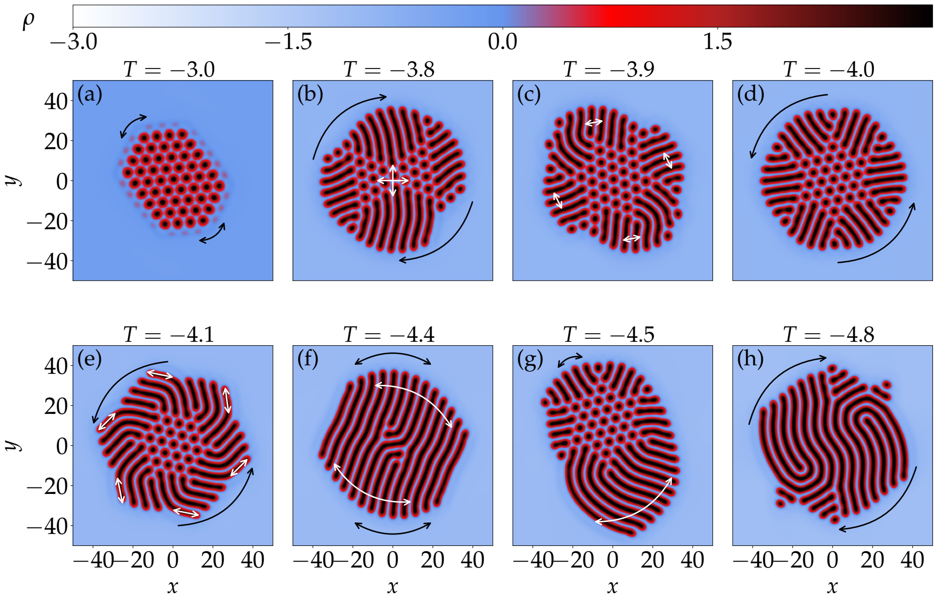

Fig. 4.9: Examples of intricate behavior of crystalline clusters at lower T and $\bar{\rho} = -1$. The black and white arrows indicate collective motion and inner modi of motion, respectively. The local density ρ is given by the colorbar. The individual states are described in the main text. Remaining parameters are as in Fig. 4.7.

patterned star. (d) shows a rotating two-phase crystallite, the hexagons once again forming a star. The overall structure shows 180 degree rotational symmetry. (e) shows a rotating two-phase crystallite with additional wobbling motion of the stripes. The structure has 60 degree rotational symmetry. (f) shows a swinging stripe structure with additional waving motion of the stripes, once again with 180 degree rotational symmetry. (g) shows a swinging two-phase crystallite with the hexagons forming a star, while the longer stripes at the bottom wave. Finally, (h) shows a rotating stripe state with inversion symmetry.

5 Bose-Einstein Condensation

5.1 Bose-Einstein Condensation with Interactions

Bosons are particles with integer spin which (in contrast to half-integer spin fermions) are allowed to occupy the same single-particle state. In layperson terms Bose-Einstein condensation occurs when a dilute gas of bosons is cooled to very low temperatures, where their thermal de Broglie wavelength

$$\lambda_{\mathrm{dB}} = \sqrt{\frac{2\pi\hbar^2}{mk_BT}} \tag{5.1}$$

(with mass m, Boltzmann constant k_B, reduced Planck constant $\hbar$ and temperature T) becomes a size comparable to the mean distance between the particles $d_p = \rho^{-1/3}$ with particle number density $\rho = N/V$. At that point the particle waves overlap so much that they become indistinguishable, which constitutes a new phase of matter with different properties [141]. A conceptual visualization of the same (inspired by Ref. [94]) can be found in Fig.5.1 for a) high and b) low temperature Bose gases. In the former case the bosons can be treated like hard spheres. In the latter case the bosons have wave character with different phases. At the critical temperature c) there is the onset of Bose-Einstein condensation, where particles overlap to the point that they become indistinguishable. This is also the start of phase coherence. Many, but not all bosons are now part of the lowest energy state. In the hypothetical case of d) $T = 0$, there would be a “pure condensate” where the lowest energy state is occupied by all bosons.

For a more thorough explanation of the general principles for the non-interacting Bose gas see, e.g., Ref. [147]. This thesis, meanwhile, lays the focus on a weakly interacting Bose gas, considered under dilute conditions.

A weakly interacting gas [147] is defined as interacting on a length scale a where $|a|^3\rho \ll 1$. The diluteness condition [147] requires a to be much smaller than the distance between particles $d_p = \rho^{-1/3}$. It therefore is:

$$a \ll \rho^{-\frac{1}{3}}\,. \tag{5.2}$$

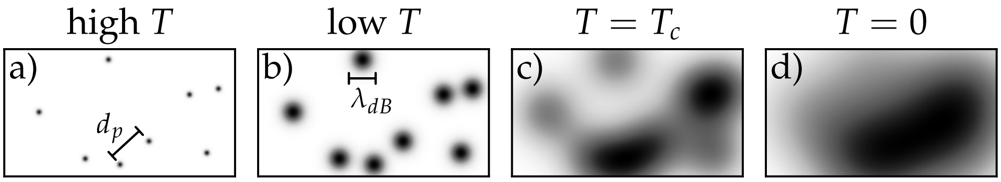

Fig. 5.1: Conceptual visualization of Bose gases at different temperatures: a) high temperature, bosons primarily interact as particles with velocity v and distance d_p, b) low temperature, bosons interpreted as wave packets with wavelength λ_{dB} according to Eq. (5.1), c) Bose-Einstein condensation with coherent matter wave overlap where $\lambda_{\mathrm{dB}} \approx d_p$, d) zero temperature, "pure condensate". Inspired by Ref. [94].

The latter makes it possible to focus on the interactions between only two particles. Violating the diluteness condition leads to inelastic three-body interactions and recombination effects which result in atom loss in the BEC [54].

Under the described conditions the dynamics of a Bose-Einstein condensate are governed by the (second quantization) Hamiltonian [147, 165][1] of the field operator $\hat{\psi}$

$$\begin{aligned} \hat{H} = & \int \mathrm{d}\mathbf{r}\, \hat{\psi}^\dagger(\mathbf{r}) \left[-\frac{\hbar^2}{2m}\Delta + V_{\mathrm{ext}} \right] \hat{\psi}(\mathbf{r}) \\ & + \frac{1}{2} \iint \mathrm{d}\mathbf{r}'\mathrm{d}\mathbf{r}\, \hat{\psi}^\dagger(\mathbf{r})\hat{\psi}^\dagger(\mathbf{r}')U_{\mathrm{int}}(\mathbf{r}-\mathbf{r}')\hat{\psi}(\mathbf{r}')\hat{\psi}(\mathbf{r})\,, \end{aligned} \tag{5.3}$$

with the particle interaction described by the real function $U_{\mathrm{int}}(\mathbf{r}-\mathbf{r}')$ and external trapping potential given by $V_{\mathrm{ext}}(\mathbf{r})$. From there the time evolution is described by the Heisenberg equation of motion

$$\begin{aligned} i\hbar\partial_t\hat{\psi}(\mathbf{r},t) &= [\hat{\psi}(\mathbf{r},t), \hat{H}] \\ &= \left[-\frac{\hbar^2}{2m}\Delta + V_{\mathrm{ext}} + \frac{1}{2}\int \mathrm{d}\mathbf{r}'\, \hat{\psi}^\dagger(\mathbf{r}')U_{\mathrm{int}}(\mathbf{r}-\mathbf{r}')\hat{\psi}(\mathbf{r}') \right] \hat{\psi}(\mathbf{r},t)\,. \end{aligned} \tag{5.4}$$

If the ground state has a macroscopic occupation number a mean-field description of the field operator can be derived using the Bogoliubov ansatz [24]:

$$\hat{\psi} = \psi + \hat{\phi}\,. \tag{5.5}$$

---

[1] The full N-body Hamiltonian is reduced to this single particle Hamiltonian due to particles being indistinguishable. A more thorough explanation can be found in, e.g., Sec. 4 of Ref. [34]

Here ψ is the expectation value $\langle\hat{\psi}\rangle$, represented by $\langle\cdot\rangle$, and the so-called condensate wave function. It is normalized to $\langle\psi|\psi\rangle = N$ and for very weak interactions it represents the wave function all bosons in the BEC reside in. $\hat{\phi}$ represents fluctuations and averages to zero, i.e., $\langle\hat{\phi}\rangle = 0$ [75].

Applied to the expectation value of Eq. (5.4) it follows:

$$i\hbar\partial_t\psi(\mathbf{r},t) = \left[-\frac{\hbar^2}{2m}\Delta + V_{\text{ext}}\right]\psi + \frac{1}{2}\int \mathrm{d}\mathbf{r}'\, U_{\text{int}}(\mathbf{r}-\mathbf{r}')\langle\hat{\psi}^\dagger(\mathbf{r}',t)\hat{\psi}(\mathbf{r}',t)\hat{\psi}(\mathbf{r},t)\rangle\,. \tag{5.6}$$

The Hartree-Fock approximation neglects all fluctuations but requires the first Born approximation [34]. Its application would reduce $\langle\hat{\psi}^\dagger(\mathbf{r}',t)\hat{\psi}(\mathbf{r}',t)\hat{\psi}(\mathbf{r},t)\rangle$ to $|\psi(\mathbf{r}',t)|^2$ and lead to the Hartree equation

$$i\hbar\partial_t\psi = \left[-\frac{\hbar^2}{2m}\Delta + V_{\text{ext}} + (U_{\text{int}} * |\psi|^2)\right]\psi\,, \tag{5.7}$$

with the convolution $(U_{\text{int}} * |\psi|^2) = \int U_{\text{int}}(\mathbf{r}'-\mathbf{r})|\psi(\mathbf{r}',t)|^2\mathrm{d}\mathbf{r}'$.

The first Born approximation requires U_{int} to be weak enough to neglect correlations between particles. Contact interactions have forms relatively close to a Lennard-Jones potential, which is strong for short range interactions and therefore does not fit the criterion. This is demonstrated in Fig. 5.2 for small particle distances d_p. The potential even has an optimal distance d_c between particles which would results in crystallization on large time scales, but is suppressed by the diluteness of the BEC for shorter time scales [34, 75, 147].

In the second Born approximation neither the possible bound state nor the strong interacting parts cause problems, when dilute conditions (5.2) are taken into account [75, 147]. Under those the results of the Schrödinger equation for the interacting and non-interacting case can be compared for very large d_p. The only difference in the results is a phase shift proportional to the scattering length a_s [75, 147, 34].

In consequence, any potential U_{eff} which results in the same phase shift is a valid approximation for U_{int}. Choosing one which is weak for all d_p, e.g., a Gaussian (see Fig. 5.2), allows for the application of the first Born approximation after all. As the interaction is short range, U_{eff} can be further approximated, e.g., $U_{\text{eff}} = g\delta(\mathbf{r})$. For scattering it is $g = 4\pi\hbar^2 a_s/m$ [147] with s-wave scattering length a_s. This turns Eq. (5.7) into

$$i\hbar\partial_t\psi = \left[-\frac{\hbar^2}{2m}\Delta + V_{\text{ext}} + g|\psi|^2\right]\psi\,, \tag{5.8}$$

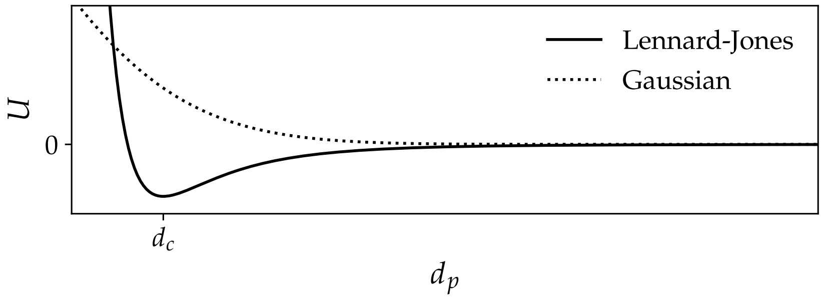

Fig. 5.2: Possible particle interaction potentials U depending on the distance d_p between particles. The Lennard-Jones potential (solid line) is large for small d_p and encourages a bound state at $d_p = d_c$. The Gaussian potential (dotted line) can be used as an approximation as it causes the same phase shift. It is weak for all d_p and does not give rise to a bound state.

as U_{int} is replaced by U_{eff}.

The s-wave scattering length is tunable through external fields using Feshbach resonances [89], making a_s a viable continuation parameter in addition to the density $\rho = |\psi|^2$.

Additional long-range interactions can influence the properties of the quantum gas (e.g., shape, density, excitation, possible phases, accessible range of parameters). They enter U_{eff} through an additional term for which the first Born approximation also has to be valid. For example, for dipole-dipole interactions the length scale is a_{dd} which is different depending on the specific dipole.

The temporal evolution of such a BEC can be described using the non-local Gross-Pitaevskii equation (GPE) [67, 146], where the new effective potential U_{eff} (which still contains a scattering term g) replaces U_{int} in Eq. (5.7):

$$i\hbar\partial_t\psi = \left[-\frac{\hbar^2}{2m}\Delta + V_{\text{ext}} + (U_{\text{eff}} * |\psi|^2)\right]\psi\,. \tag{5.9}$$

When working with dipolar interactions beyond mean-field effects have to be considered, meaning $\langle\widehat{\psi}^\dagger(\mathbf{r}',t)\widehat{\psi}(\mathbf{r}',t)\widehat{\psi}(\mathbf{r},t)\rangle$ is subject to less drastic approximations. The $|\psi(\mathbf{r}')|^2\psi(\mathbf{r})$ remains as before, i.e., it matches the previous GPE. Due to the small size of the fluctuations the remaining terms are only considered in quadratic order, while the cubic term is neglected. What remains are the non-condensate density terms $\langle\widehat{\phi}^\dagger(\mathbf{r}')\widehat{\phi}(\mathbf{r}')\rangle\psi(\mathbf{r})$ and $\langle\widehat{\phi}^\dagger(\mathbf{r}')\widehat{\phi}(\mathbf{r})\rangle\psi(\mathbf{r}')$ as well as the anomalous non-condensate density term $\langle\widehat{\phi}(\mathbf{r}')\widehat{\phi}(\mathbf{r})\rangle\psi^*(\mathbf{r}')$. In the Popov approximation, the latter is neglected [66]. From here the remaining terms are subjected to a Bogoliubov transformation, leading to the Bogoliubov-de Gennes equations, which in turn can be solved using the local density approximation. The result is the so-called Lee-Huang-Yang expansion [101, 109, 108, 72], a correction term for quantum fluctuations with strength γ_{QF}:

$$i\hbar\partial_t\psi = \left[-\frac{\hbar^2}{2m}\Delta + V_{\mathrm{ext}} + (U_{\mathrm{eff}} * |\psi|^2) + \gamma_{\mathrm{QF}}|\psi|^3\right]\psi\,. \tag{5.10}$$

γ_{QF} is directly related to the quantum depletion of the condensate due to excitations, which is small ($\gamma_{\mathrm{QF}}|\psi|^3$ contains $\sqrt{a_s^3\rho}$ which is $\ll 1$ for weak interactions [147, 78]) and > 0 making it repulsive, allowing it to stabilize otherwise inaccessible states in specific parameter regimes [144, 56, 90, 196, 197, 79].

The accompanying energy to the GPE is

$$E = \frac{1}{V}\int \mathrm{d}\mathbf{r}\,\psi^* \left(-\frac{\hbar^2}{2m}\Delta + V_{\mathrm{ext}} + \frac{1}{2}(U_{\mathrm{eff}} * |\psi|^2) + \frac{2}{5}\gamma_{\mathrm{QF}}|\psi|^3\right)\psi\,. \tag{5.11}$$

It connects to Eq. (5.10) through

$$i\hbar\partial_t\psi = \frac{\delta E}{\delta\psi^*}\,. \tag{5.12}$$

In a complex-time evolution Eq. (5.12) represents standard gradient dynamics on the energy E for coupled order parameter fields $\mathrm{Re}(\psi)$ and $\mathrm{Im}(\psi)$.

5.2 Phases, Transitions and Linear Stability

5.2.1 Superfluid, Supersolid and Isolated Droplets

The unmodulated ground state of the BEC behaves like a superfluid, which is an exotic state of matter. In layperson terms its a gas, but due to coherence between particles it has the properties of a fluid with its attributes taken to the extreme, i.e., it flows without friction. This allows, e.g., for passage through narrow channels or quantized vortices [141].

More formally speaking, friction would slow down the flow of a superfluid, as it transforms kinetic energy into quantized thermal energy in the form of an elementary excitation. The elementary excitation, however, raises the overall energy of the superfluid. In other words, retaining a frictionless flow is more energetically favorable [95, 100].

The supersolid is a contradictory state of matter, which retains superfluidity, but also shows a weakly modulated density structure with discrete translational symmetry reminiscent of a solid [115].

The portion of the BEC which is superfluid is estimated using the Leggett estimator [104], which gives an upper bound for the superfluid fraction

$$f_s = \left[\frac{|\psi_0|^2}{L} \int_0^L \frac{\mathrm{d}x}{|\psi(x)|^2} \right]^{-1} . \tag{5.13}$$

It describes the fraction of atoms that support frictionless flow, written here for a boost along a line of length L in x-direction. Alternatively, this can be defined for the fraction of resting particles in a rotating cylinder, in which case $L = 2\pi$ while x is replaced by the angle θ. In both cases $|\psi_0|^2$ gives the mean density of ψ.

If there is no modulation, i.e., if $\psi = \psi_0 =$const this results in $f_s = 1$. For a small modulation it is $f_s < 1$. If the modulation of the supersolid becomes so large that the density between peaks at x_{min} falls to zero, it is $1/|\psi(x_{\mathrm{min}})|^2 \to \infty$ and $f_s \to 1/\infty = 0$. This so-called isolated droplet (or crystal) state has no long range phase coherence and therefore is the opposite of a supersolid [26].

As the Legget estimator only gives an upper bound the use of Eq (5.13) does not necessarily give precise results [176]. Other ways of measuring the superfluid fraction of a supersolid have been proposed [17].

Alternatively, to avoid the ambiguity, the amplitude modulation induced in the field ψ can be measured using the contrast C [26, 39, 177]. It takes the form

$$C = \frac{|\psi|^2_{\mathrm{max}} - |\psi|^2_{\mathrm{min}}}{|\psi|^2_{\mathrm{max}} + |\psi|^2_{\mathrm{min}}} . \tag{5.14}$$

Similar to the superfluid fraction it has a range from zero to one, however, for the contrast values close to zero represent a superfluid. Higher values are associated with a supersolid and values close to one are considered isolated droplets.

Under the right circumstances there is a relation between the contrast and the superfluid fraction from Eq. (5.13), which is detailed in Ref. [38]. Specifically, for shallow modulations, i.e., the supersolid regime, it is $f_s \approx 1 - C^2/2$.

5.2.2 Stability and Phase Transition

The stationary state of the GPE is

$$\psi(\mathbf{r}, t) = \psi_0(\mathbf{r}) e^{-i\mu t/\hbar} , \tag{5.15}$$

with a parameter μ which is constant with respect to $\mathbf{x}$ and t. Inserted into the GPE it gives the a steady state equation for the chemical potential μ:

$$\left[-\frac{\hbar^2}{2m}\Delta + \int \mathrm{d}\mathbf{r}' |\psi_0(\mathbf{r}')|^2 U_{\mathrm{eff}}(\mathbf{r}'-\mathbf{r}) + \gamma_{\mathrm{QF}}|\psi_0(\mathbf{r})|^3 - \mu\right]\psi_0(\mathbf{r}) = 0\,. \tag{5.16}$$

Now small amplitude perturbations $\delta(\mathbf{r},t)$ of $\psi_0(\mathbf{r})$ are used to determine the linear stability by way of the excitation spectrum [24], similar to the proceedings in Ch. 2. The perturbation takes the form

$$\delta(\mathbf{r},t) = \varepsilon\left[u(\mathbf{r})e^{-i\omega t} + v^*(\mathbf{r})e^{+i\omega t}\right]\,, \tag{5.17}$$

with the smallness parameter ε, excitation ω and Bogoliubov modes $u(\mathbf{r})$ and $v(\mathbf{r})$. The perturbed wave function Eq. (5.15) is

$$\psi_p(\mathbf{r},t) = \left[\psi_0(\mathbf{r}) + \delta(\mathbf{r},t)\right]e^{-i\mu t/\hbar}\,. \tag{5.18}$$

Eq. (5.18) is then introduced into Eq. (5.10), linearized in ε and sorted by terms $\propto e^{-i\omega t}$, $\propto e^{+i\omega t}$ as well as terms without exponential functions. The latter simply gives Eq. (5.16), which has to be solved to be able to identify μ and (if not already known) ψ_0.

Terms with $e^{-i\omega t}$ and $e^{+i\omega t}$ lead to a pair of differential equations (cf. [158, 75]):

$$\begin{aligned}
\hbar\omega u(\mathbf{r}) = &\left[-\frac{\hbar^2}{2m}\Delta + \int \mathrm{d}\mathbf{r}' |\psi_0(\mathbf{r}')|^2 U_{\mathrm{eff}}(\mathbf{r}'-\mathbf{r}) + \gamma_{\mathrm{QF}}|\psi_0(\mathbf{r})|^3 - \mu\right]u(\mathbf{r}) \\
&+ \psi_0(\mathbf{r})\int \mathrm{d}\mathbf{r}' U_{\mathrm{eff}}(\mathbf{r}'-\mathbf{r})(u(\mathbf{r}') + v(\mathbf{r}'))\psi_0(\mathbf{r}') \\
&+ \frac{3}{2}\gamma_{\mathrm{QF}}|\psi_0(\mathbf{r})|^3(u(\mathbf{r}) + v(\mathbf{r})) \qquad (5.19)\\
-\hbar\omega v^*(\mathbf{r}) = &\left[-\frac{\hbar^2}{2m}\Delta + \int \mathrm{d}\mathbf{r}' |\psi_0(\mathbf{r}')|^2 U_{\mathrm{eff}}(\mathbf{r}'-\mathbf{r}) + \gamma_{\mathrm{QF}}|\psi_0(\mathbf{r})|^3 - \mu\right]v^*(\mathbf{r}) \\
&+ \psi_0(\mathbf{r})\int \mathrm{d}\mathbf{r}' U_{\mathrm{eff}}(\mathbf{r}'-\mathbf{r})(u^*(\mathbf{r}') + v^*(\mathbf{r}'))\psi_0(\mathbf{r}') \\
&+ \frac{3}{2}\gamma_{\mathrm{QF}}|\psi_0(\mathbf{r})|^3(u^*(\mathbf{r}) + v^*(\mathbf{r})) \qquad (5.20)
\end{aligned}$$

These equations can be solved, which is easiest if $\psi_0 = $const, using $u(\mathbf{r}) = ue^{i\mathbf{kr}}$ and $v(\mathbf{r}) = ve^{i\mathbf{kr}}$ with constant u and v. This finally leads to an excitation spectrum of the form

$$\hbar^2\omega^2 = f(\mathbf{k}, \hat{U}_{\mathrm{eff}}) \tag{5.21}$$

when substituting either u or v from the equation.

The excitation spectrum for a Bose-Einstein condensate near a phase transition towards a supersolid or isolated droplet state takes the form of a classical maxon-roton structure, i.e., starting from $|\mathbf{k}| = 0$ the spectrum passes a maximum, the maxon, and a minimum, the so-called roton minimum.

An example of an excitation spectrum with typical maxon-roton structure is given in Fig. 5.3 for a system where changes in a parameter α (often the strength of the interaction) lead to a phase transition.

Three excitation spectra are shown. One for a state right on the border of linear stability $\alpha = \alpha_c$ (blue), one for a linearly stable state at $\alpha < \alpha_c$ (black) and one for a linearly unstable state $\alpha > \alpha_c$ (red). The latter is indicated by a parameter configuration which leads to $f(\mathbf{k}, \hat{U}_{\text{eff}}) < 0$ state [147, 75, 158]. As the latter are purely complex the spectrum is only plotted for regions with $\omega > 0$.

The excitation spectrum functions much like the dispersion relation introduced in Ch. 2, though upside down, meaning instability is now determined by $\omega^2 < 0$, leading to complex values for ω. It matches a conserved-Turing instability.

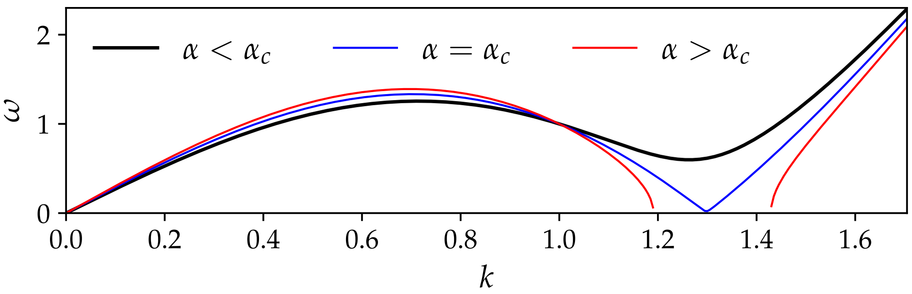

Fig. 5.3: Example of a excitation spectra with typical maxon-roton structure, given at different parameter values. $\alpha = \alpha_c$ (blue) is the excitation spectrum at the border of linear stability, while $\alpha < \alpha_c$ (black) and $\alpha > \alpha_c$ (red) correspond to excitation spectra matching linearly stable and unstable parameter regions.

5.3 Hydrodynamic Formulation for Steady State Solutions

The transformation of the Schrödinger equation into a hydrodynamic form consisting of separate transport/balance equations for the density $\rho(\mathbf{r}, t)$ and the phase $\phi(\mathbf{r}, t)$ of the probability wave function was introduced by Madelung in 1927 [116].

The first step of the Madelung transformation is to write the complex wave function into polar form as

$$\psi(\mathbf{r},t) = \sqrt{\rho(\mathbf{r},t)}e^{i\phi(\mathbf{r},t)} \tag{5.22}$$

and using it in the time dependent Schrödinger equation

$$i\hbar\partial_t\psi = \left(-\frac{\hbar^2}{2m}\Delta + V(\mathbf{r})\right)\psi\,, \tag{5.23}$$

where $V(\mathbf{r})$ is an arbitrary potential. In case of a Bose-Einstein condensate it is $V_{\text{ext}} + (U_{\text{eff}} * |\psi|^2) + \gamma_{\text{QF}}|\psi|^3$ (see Eq. (5.10)).

Separating the complex and real parts gives after some further algebraic steps (see Ref. [116])

$$\partial_t\rho = -\nabla\cdot\left(\rho\frac{\hbar}{m}\nabla\phi\right) = -\nabla\cdot\mathbf{j}\,, \tag{5.24}$$

which represents a continuity equation with probability current $\mathbf{j} = \rho\frac{\hbar}{m}\nabla\phi$, and

$$\hbar\partial_t\phi = -(Q+V) - \frac{\hbar^2}{2m}(\nabla\phi)^2\,, \tag{5.25}$$

where $Q = -\frac{\hbar^2}{2m}\frac{\Delta\sqrt{\rho}}{\sqrt{\rho}}$ is the so-called quantum potential. The term assumes that at no point $\rho = 0$, which automatically disallows trapping potentials and completely isolated droplets.

When looking at steady states of a BEC it is useful to assume $\phi = \mu t/\hbar$, which gives $\nabla\phi = 0$ and $\partial_t\phi = \mu/\hbar$ (see Refs. [73, 171]). Then, the chemical potential μ is given by Eq. (5.25) as

$$\mu = -(Q+V)\,. \tag{5.26}$$

In addition, the flux $\mathbf{j}$ in Eq. (5.24)) can be defined similar to Eq. (3.2) [73] using $\mathbf{j} = \nabla\mu$. The constant μ assumed before is therefore a consequence of the flux evening it out when evolving towards a steady state. This leads to

$$\partial_t\rho = -\Delta\mu = \Delta\left(Q+V\right)\,. \tag{5.27}$$

As $\nabla\mu = 0$ it follows $\partial_t\rho = 0$ which matches the definition of steady states and keeps it in accordance with the conditions introduced above.

Inserting Q and the standard terms of a GPE for V Eq. (5.27) leads to

$$\partial_t\rho = \Delta\left(-\frac{\hbar^2}{2m}\frac{\Delta\sqrt{\rho}}{\sqrt{\rho}} + V_{\text{ext}} + (U_{\text{eff}} * \rho) + \gamma_{\text{QF}}\sqrt{\rho}^3\right)\,. \tag{5.28}$$

It no longer depends on ϕ and is therefore solely density dependent.

5.4 Simplified Nonlocal Model and its Local Approximations

Though dipolar systems are currently the main focus of studies of the supersolid phase, for simplicity, a commonly adopted prototypical toy model of soft-core bosons, [76, 41, 159, 115, 114, 40], which approximates the interaction potential caused by the so-called Rydberg-blockade effect [112, 76, 123], is used to show the application of methods.

To that end the method explained in Sec. 5.3 is used, leading to a purely density-dependent formulation with long-range interaction. The resulting nonlocal equation can be approximated as a local equation, using an abbreviated interaction potential as detailed in Sec. 3.3 (ϵ-approximation). This approach differs from the one in Ref. [73], where the match between exact model and approximation is determined by the form of $\widehat{U}$, rather than by the threshold of linear stability.

Some of these results, specifically, most of those pertaining to the approximated model have been published in Ref. [171].

5.4.1 Governing Equation and Stability Considerations for General Interactions

Starting from the GPE (5.9) with $V_{\text{ext}} = 0$, but rescaled so $\hbar$ and m vanish, the nonlocal governing equation is

$$i\partial_t\psi = \left[-\frac{1}{2}\Delta + (U * |\psi|^2)\right]\psi\,, \tag{5.29}$$

with $\bar{\rho} = \frac{1}{V}\int |\psi|^2 \mathrm{d}^d r$, where V is the volume of the considered domain and d the spatial dimension.

The stability of the uniform ground state is determined as detailed in Sec. 5.2.2, leading to

$$\omega^2(\mathbf{k}) = \frac{k^2}{2}\left(\frac{k^2}{2} + 2\bar{\rho}\widehat{U}(\mathbf{k})\right)\,, \tag{5.30}$$

where $\widehat{U}(\mathbf{k})$ is the Fourier transform of $U(\mathbf{r})$. All considered cases have radial symmetry, therefore $k = |\mathbf{k}|$ can be used in place of $\mathbf{k}$.

For pattern formation, at the border of linear stability of the uniform state the following requirements must be met: $\omega^2(k = k_c) = 0$ and $\partial\omega^2/\partial k\big|_{k=k_c} = 0$ with the critical values k_c for the wavenumber and $\bar{\rho}_c$ for the density.

Using the hydrodynamic formulation plus steady state considerations as in Sec. 5.3 for the governing equation Eq. (5.29) turns it into

$$\partial_t \rho = \Delta \left[\frac{(\nabla\rho)^2}{8\rho^2} - \frac{\Delta\rho}{4\rho} + (U * \rho) \right] . \tag{5.31}$$

Critical values exactly match the ones obtained with Eq. (5.29). The chemical potential is similarly adapted

$$\mu = -\left[\frac{(\nabla\rho)^2}{8\rho^2} - \frac{\Delta\rho}{4\rho} + (U * \rho) \right] , \tag{5.32}$$

matching Eq. (5.26).

5.4.2 Local Approximation

For the local approximation a Taylor series up to fourth order of the interaction described in Fourier space is used, leading to

$$\hat{U}^{(s)}(k) = g_0 + g_2 k^2 + g_4 k^4 . \tag{5.33}$$

The accompanying dispersion relation

$$\omega^{2(s)} = \frac{k^2}{2} \left(\frac{k^2}{2} + 2\bar{\rho}\hat{U}^{(s)} \right) \tag{5.34}$$

is then adjusted to the dispersion relation of the nonlocal model at $k = k_c$ by choosing the free parameters (g_0, g_2, g_4) such that root and curvature at $k = k_c$ match, i.e.

$$k_c = k_c^{(s)} , \tag{5.35}$$

$$\bar{\rho}_c = \bar{\rho}_c^{(s)} , \tag{5.36}$$

$$\frac{\partial^2 \omega^2}{\partial k^2}\Big|_{k=k_c} = \frac{\partial^2 \omega^{2(s)}}{\partial k^2}\Big|_{k=k_c^{(s)}} . \tag{5.37}$$

Independently of the specific form of the interaction, the solution of this set is given by

$$\begin{aligned} g_0 &= \frac{k_c^2 \partial_{kk}\hat{U}(k_c) - 2\hat{U}(k_c)}{8} , \\ g_2 &= -\frac{2g_0 - \hat{U}(k_c)}{k_c^2} = -\frac{k_c^2 \partial_{kk}\hat{U}(k_c) - 6\hat{U}(k_c)}{4k_c^2} , \\ g_4 &= \frac{g_0}{k_c^4} . \end{aligned} \tag{5.38}$$

The approximated governing equation now has the form

$$\partial_t \rho = -\Delta\mu = \Delta\left[\frac{1}{2}\left(\frac{(\nabla\rho)^2}{4\rho^2} - \frac{\Delta\rho}{2\rho}\right) + \left(g_0\rho - g_2\Delta\rho + g_4\Delta^2\rho\right)\right] . \tag{5.39}$$

with the chemical potential

$$\mu = \left[\frac{\Delta\rho}{4\rho} - \frac{(\nabla\rho)^2}{8\rho^2} - \left(g_0\rho - g_2\Delta\rho + g_4\Delta^2\rho\right)\right] . \tag{5.40}$$

For convenience, the model is rescaled to better match the linear parts of the PFC equation:

$$r \to r' \sqrt{-\frac{g_2}{2g_4}} , \tag{5.41}$$

$$t \to t' \,\frac{4g_4}{g_2^2} , \tag{5.42}$$

$$\rho \to \rho' \,\frac{(-g_2)}{2} . \tag{5.43}$$

Using Eqs. (5.41)-(5.43) and dropping the primes leads to

$$\partial_t \rho = \Delta\left[\frac{(\nabla\rho)^2}{8\rho^2} - \frac{\Delta\rho}{4\rho} + (\alpha_u + 1)\rho + 2\Delta\rho + \Delta^2\rho\right] , \tag{5.44}$$

where

$$\alpha_u = \frac{4g_0 g_4}{g_2^2} - 1 \tag{5.45}$$

as in Ref. [73]. In terms of the interaction and critical values it takes the form

$$\alpha_u(k_c, \bar{\rho}_c) = \frac{\left(k_c^2\partial_{kk}\hat{U}(k_c) - 2\hat{U}(k_c)\right)^2}{\left(k_c^2\partial_{kk}\hat{U}(k_c) - 6\hat{U}(k_c)\right)^2} - 1 . \tag{5.46}$$

For the interactions considered here, $\alpha_u > -1$ follows naturally, while $\alpha_u < 0$ follows due to excessive amplitude growth which invalidates the used approximation.

The energy[2] of the system is given by

$$F[\rho] = \frac{1}{2}\int_V \left[\frac{|\nabla\rho|^2}{4\rho} + (\alpha_u + 1)\rho^2 + 2\rho\Delta\rho + \rho\Delta^2\rho\right] \mathrm{d}^n r , \tag{5.47}$$

---

[2] As this now resembles expressions well known from soft-matter physics the same vocabulary is applied here. This specifically concerns the energy which is called a “free energy functional” even though the considered BEC has constant $T = 0$. See also Ch. 3.

which allows for rewriting the system as gradient dynamics, i.e., the dissipative conserved dynamics take the form:

$$\frac{\partial \rho}{\partial t} = \Delta \mu \,, \tag{5.48}$$

where the chemical potential is defined as the functional derivative

$$\mu = \frac{\delta F}{\delta \rho} \,, \tag{5.49}$$

and the corresponding grand potential density is Ω/V with

$$\Omega = F - \int \mu \rho \mathrm{d}^n r \,. \tag{5.50}$$

Together they can be used to determine coexistence (cf. Ch. 2.4).

5.4.3 Soft-Core Bosons and their Dispersion Relation

From this section onward the interaction of a prototypical model for soft-core bosons is considered. The interaction takes the form of a Heaviside step function $\Theta(1-r)$ with $r = |\mathbf{r}|$ [76, 159, 115]. For s-wave scattering a delta function $\delta(r)$ is added, leading to

$$U(r) = \Theta(1-r) + a\delta(r) \,. \tag{5.51}$$

Both, the range and the strength of this interaction can be absorbed into the mean density by way of rescaling [115], leaving a as the rescaled scattering length, while range and height of the Heaviside step function are one. The practicality of specific values of a (e.g., the collapse for attractive scattering lengths discussed in Ref. [47, 122]) is not considered, as this is a demonstration of method and values not accessible for one specific model might occur for another interaction.

Specific critical values can now be determined from the dispersion relation, both for the nonlocal model (5.30) and the local approximation (5.34). The interaction in Fourier space is given by

$$\hat{U}(k) = \begin{cases} \dfrac{2\sin(k)}{k} + a \,, & 1D \\ 2\pi \dfrac{J_1(k)}{k} + a \,, & 2D \end{cases} \tag{5.52}$$

where $J_1(k)$ is the Bessel function of the first kind.

From Eq. (5.52) it becomes obvious that Eqs. (5.38) give values that depend on a, as do the critical values. Figure 5.4 (a) directly compares the dispersion relations at the

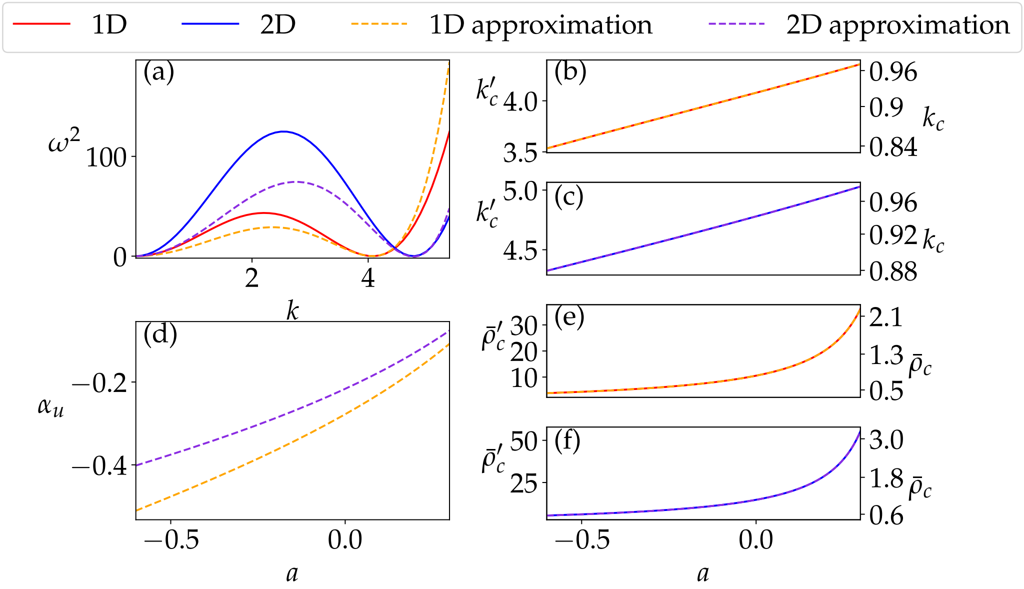

Fig. 5.4: Comparison between the exact nonlocal model (Eq. (5.29)) and its local approximation (Eq. (5.44)). (a) Dispersion relations at the onset of the modulational instability at $a = 0$ given by Eqs. (5.30) (exact, solid lines) and (5.34) (approximation, dashed lines). Therefore it is $\bar{\rho} = \bar{\rho}_c$ and $\bar{\rho}' = \bar{\rho}_c'$. One- and two-dimensional cases are represented in red/orange and blue/purple, respectively. Also given are the dependencies of the (b,c) critical wavenumber k_c and the (e,f) critical density $\bar{\rho}_c$ on the rescaled scattering length a. Panel (d) shows the dependency of α_u on a. The axis on the left and right side of panels (b,c,e,f) correspond to the unscaled and scaled system, respectively. Due to the nonlinear scaling the right axis is nonlinear.

onset of the modulational instability for $a = 0$ for both, the exact and approximated case, meaning $\bar{\rho} = \bar{\rho}_c$ and $\bar{\rho}' = \bar{\rho}_c'$, respectively. Comparisons are made in one (1D) and two dimensions (2D). The results confirm the built-in matching of root and curvature for the critical values, i.e., wavenumber k_c and density $\bar{\rho}_c$ perfectly match. The curvature, while correct at $k = k_c$ differs at $k = 0$ and the position and height of the maximum is changed significantly. In addition, figures 5.4 (b) to (f) show how k_c, $\bar{\rho}_c$ and α_u depend on the rescaled scattering length a.

5.4.4 Comparing the Nonlocal Model and Local Approximation

This section compares results regarding the bifurcation which marks the transition from the uniform to the modulated state for $U(r) = \Theta(1-r)$ (i.e., for $a = 0$) for the nonlocal model (Eq. (5.31) or (5.29)) with that of the local approximation (Eq. (5.44)). The results are depicted in Fig. 5.5 in both, one and two dimensions. The bifurcation diagrams use the mean density $\bar{\rho}$ as the continuation parameter, and the resulting states are characterized by the contrast given in Eq. (5.14).

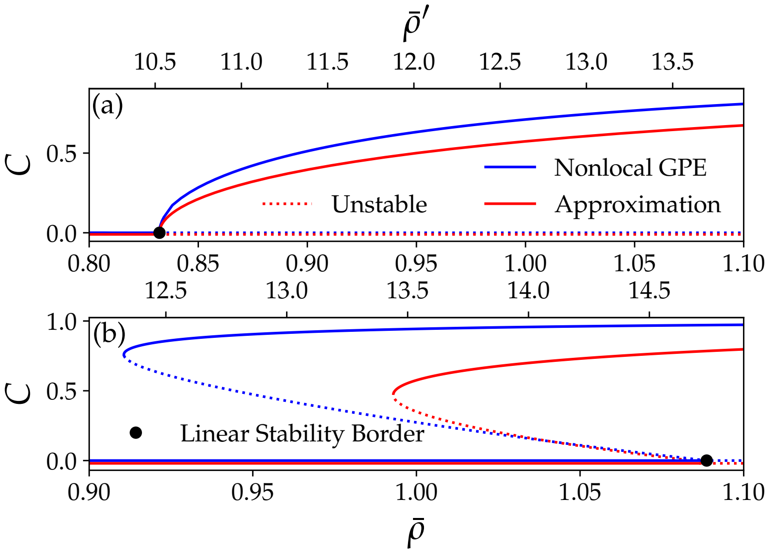

Fig. 5.5: Comparison between steady states of the GPE (Eq. (5.31), blue line) and its approximation (Eq. (5.44), red line), in form of a bifurcation diagram as a function of the mean density $\bar{\rho}$ and $\bar{\rho}'$. Solutions are characterized by the contrast C (Eq. (5.14)) and are depicted for (a) 1D and (b) 2D systems. The domain size corresponds to multiple of $2\pi/k_c$. The black filled circles indicate the linear stability threshold (compare. Fig. 5.4 (b-d)).

As expected, the linear stability thresholds match exactly, i.e., $\bar{\rho}_c' = 10.5$ for the 1D case and $\bar{\rho}_c' = 14.7$ for the 2D case. In addition, the type of the primary bifurcation is identical for full and approximated model, in particular it is supercritical in 1D and subcritical in 2D.

A consequence of these bifurcation types is that in 1D the two curves agree quite well close to the bifurcation and only quantitatively deviate with rising amplitudes further from the threshold. The difference is about 20% at the maximum density depicted in Fig. 5.5 (a).

In 2D the situation is more complicated. The unstable subcritical parts of the branches agree quite well close to the bifurcation point and both branches fold back towards higher densities at saddle-node bifurcations, leading to regions of bistability. The fold points, however, are far from the primary bifurcation and therefore differ significantly (about 10% between its positions in absolute terms), as can be seen in Fig. 5.5 (b).

Additional differences further from the primary bifurcation are detailed in Ref. [11], such as changes to phase boundaries and regions without physical solutions.

5.4.5 Periodic Patterns and Localized States

This section explores different types of periodic patterns as well as localized states supported by either model in the 2D case. However, the section starts with a brief discussion of the 1D case.

Results for One Spatial Dimension

For Eqs. (5.31) and (5.44) the primary bifurcation in systems with only one spatial dimension is always supercritical (see Sec. 5.5.2), with an example displayed in Fig. 5.5 (a). Such a bifurcation does not exclude the option of localized states in systems with mass conservation due to different mean densities of the coexisting states (see, e.g., Refs. [182, 181, 83]).

To ascertain whether localized states appear Fig. 5.6 shows the grand potential density Ω/V plotted over the chemical potential μ for the uniform and patterned states presented in Fig. 5.5 (a). In such a representation a crossing of lines for the uniform and patterned states would indicate coexistence and therefore localized states [181]. As this is not the case, the phase transition is continuous, i.e., a second order phase transition.

Similarly the nonlocal model has no crossing (not shown). Results for a one-mode approximation (also not shown) imply that the patterned branch in the grand potential always points away from the stable uniform branch, meaning that no localized states are possible in one spatial dimension independent of parameter choice.

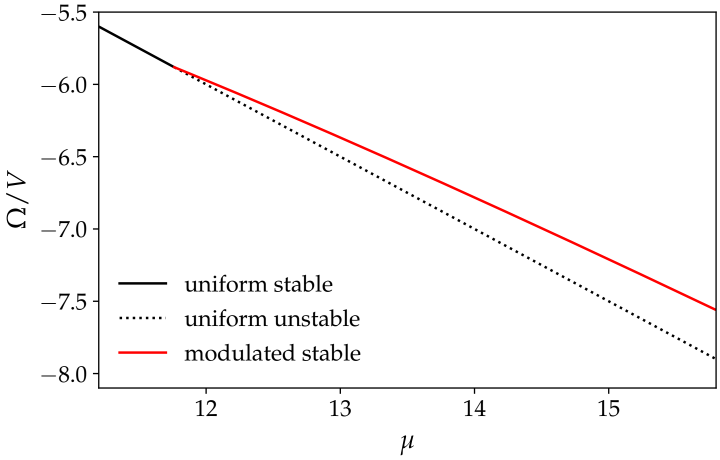

Fig. 5.6: The grand potential density Ω/V is plotted over the chemical potential μ for the patterned and uniform states in the approximated 1D case of Fig. 5.5 (a) (Eq. (5.44)). Lines are red for modulated and black for uniform states, while solid lines correspond to stable and dotted lines to unstable states. At no point do the lines for uniform and modulated states cross, therefore there is no coexistence and no localized states.

Results for Two Spatial Dimensions for the Local Approximation

To determine patterns in two dimensions and their ranges of stability as a function of $\bar{\rho}$, pseudo-arclength continuation is used at different fixed values of α_u and a respectively, with the domain size optimized for a hexagonal pattern, which matches the critical wavenumber k_c. The corresponding length is $L_c = \frac{2\pi}{k_c}$ resulting in the domain size $L_x \times L_y = \frac{2}{\sqrt{3}} L_c \times 2L_c$.

Note that periodic boundary conditions are required, in particular, to accurately predict the stability of the stripe phase and related secondary bifurcations. Neumann boundary conditions do not allow for certain changes of symmetry, resulting in missing unstable modes and therefore missing bifurcations (see, e.g., Fig. 5.18 where the pattern resulting from intermediate hexagon-stripe states is not mirror symmetric with respect to the x-axis, which under Neumann BC leads to the artifact that stripe patterns with reversed maximum and minim positions exhibit different stabilities).

An example of a resulting bifurcation diagram is given in Fig. 5.7 at $\alpha_u = -0.4$ for the approximated system. The solution measure is the contrast C given as a function of the control parameter $\bar{\rho}$. The critical wave vector is $k_c = 0.88$ leading to $L_c = 7.14$.

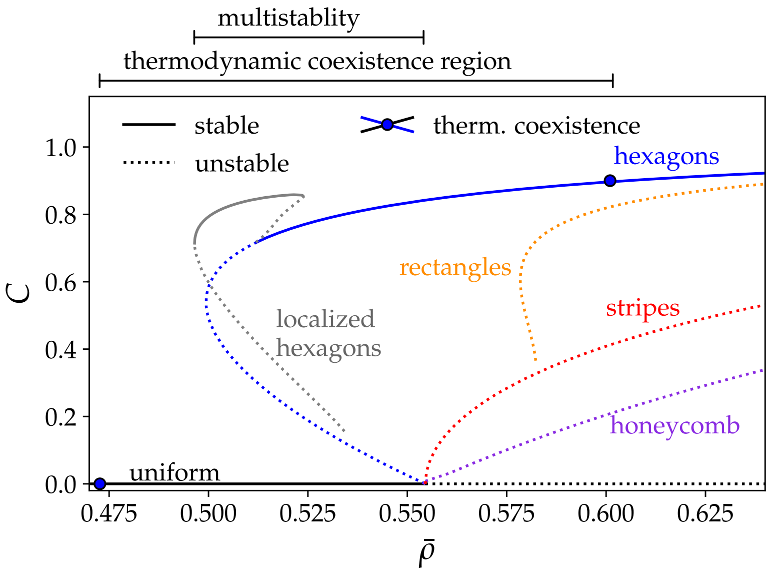

Fig. 5.7: Bifurcation diagram of the steady state solutions in 2D of Eq. 5.44 as a function of $\bar{\rho}$ at fixed $\alpha_u = -0.4$. The domain sizes are as in Fig. 2.1, except for the localized states, which are at a quarter domain size. The solutions are characterized through the contrast C [see Eq. (5.14)]. Solid and dotted lines represent stable and unstable states, respectively. The respective patterns are indicated at the curves. The two filled blue circles represent stable states coexisting in an infinite domain (identical grand potential and chemical potential, see Fig. 5.8). This indicates the range where localized states (grey line) may, in principle, exist.

The figure shows the primary bifurcation at the expected critical value of $\bar{\rho}_c = 0.555$. It is a higher order bifurcation, seemingly consisting of a transcritical bifurcation for hexagon (blue line) and honeycomb (purple line) states, as well as a pitchfork bifurcation for stripe (red line) states. Examples of those patterns can be found in Fig. 2.1 (a), (b) and (c) respectively.

More specifically, at this bifurcation the uniform state (black line) coming from lower densities, loses stability, while unstable branches of honeycomb and stripes move on to higher densities, while the equally unstable hexagon branch moves back towards lower densities. It then passes a saddle-node bifurcation at $\bar{\rho} = 0.498$, where it turns back towards higher densities and also would become stable if it were not for the localized states. Instead, it stabilizes in the following pitchfork bifurcation at $\bar{\rho} = 0.512$, which is still below $\bar{\rho}_c$, forming a multistable region.

This multistability and consequent hysteresis leads to a jump in the amplitude when passing from lower to higher densities, which is typical of a first order phase transition.

In addition, there is a branch of an unstable rectangular pattern (orange line, see Fig. 2.1 (d)) which emerges in a subcritical pitchfork bifurcation from the stripe branch. Note that this state is rectangular only due to the finite rectangular domain. On an infinite domain it would correspond to a branch of square patterns.

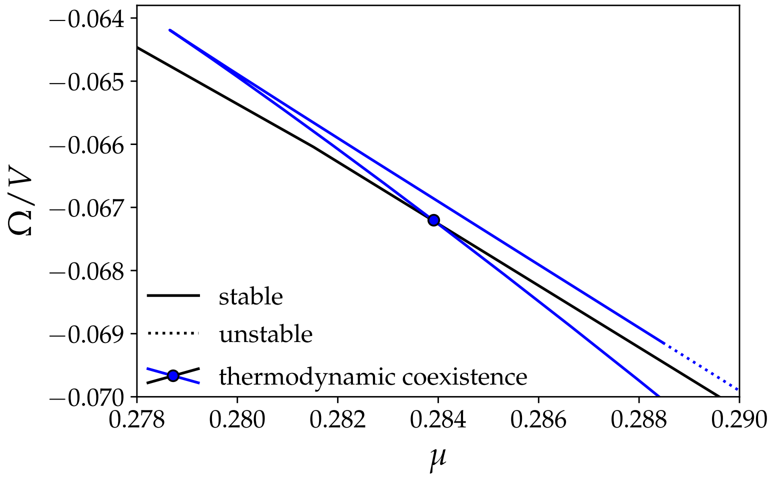

Fig. 5.8: The grand potential density Ω/V as a function of the chemical potential μ for the branches of hexagonal patterns (blue lines) and uniform states (black lines) is shown for the 2D case in Fig. 5.7. The crossing of the lines marked by a filled circle indicates that these states can coexist and localized states may exist. The coexisting states are also marked in Fig. 5.7.

The 2D case, similarly to the 1D case, is tested for thermodynamic coexistence, therefore Fig. 5.8 shows the grand potential density Ω/V as a function of the chemical potential μ for the hexagon and uniform branches. As opposed to the 1D case the branches cross (blue filled circle), indicating that a stable uniform state and a stable hexagonal pattern can coexist on a sufficiently large domain. The respective coexisting states have different densities, which are marked by two filled blue circles in the bifurcation diagram in Fig. 5.7.

Using a domain of size $16L_c/\sqrt{3} \times 2L_c$, a localized states branch (grey line) can be found, with an example of its profile given in Fig. 2.1 (e). Note that this localized state is not fully two-dimensional, as it is only localized in the x-direction.

The localized state branch does not show the typical snaking behavior found in the more standard PFC model[181], which is true even on larger domains up to $24L_c/\sqrt{3} \times 2L_c$ where one would usually find pronounced snaking behavior[81], meaning this corresponds to the small region in the classical PFC model where larger effective temperatures lead to an annihilation of the involved saddle-node bifurcations, even if the number of peaks still changes when going along the branch.

Analogously, one would expect snaking at lower values of α_u which indeed leads to a narrower interface region between the uniform background and the patterned part, however, the system closes in on regions with negative densities and the accompanying numerical instability, before any snaking can occur.

The lack of a second branch of localized states with an even number of lines of peaks (cf. Fig. 15 (d) of Ref. [181]) is due to the numerical limitation of the size of the box in combination with Neumann boundary conditions.

With the exception of small changes to the secondary bifurcation on the stripe branch and subsequent unstable patterns branching off from it, the described bifurcation diagram is typical for the approximated system at other values of α_u. Given a similar domain the primary bifurcation has generally the same form and types of emerging branches, though its position with respect to ρ changes. In addition, the fold bifurcation on the hexagon branch and the width and position of the coexistence region can vary. The bifurcation diagram of the nonlocal system also matches this general form, which includes the existence of localized states. An example for testing the stability of such a localized state for the nonlocal case with complex- and real-time evolution is given in App. A.5.

Fig. 5.9 shows a phase diagram of the local approximation spanned by $\bar{\rho}$ and α_u tracking those very changes. It shows the position of the primary bifurcation, i.e., the linear stability threshold or spinodal (black line) above which uniform states are stable, as well as the fold point on the hexagon branch (blue line), below which a hexagon shaped pattern is stable. Between those lines (light blue region) both are valid solutions, making the region bistable for domains that are small enough to not support localized states. This bistable region grows (shrinks) for higher values of $\bar{\rho}$ when tracking changes in $\bar{\rho}$ (α_u).

In addition, the coexistence region (with its borders given by the coexistence points) is marked by a grey striped region. It is fairly narrow for higher values of α_u and grows progressively wider (with respect to $\bar{\rho}$) towards lower values of α_u. For mean densities above $\bar{\rho} = 1$ (marked by a black circle) the coexistence region lies within the bistable region limited by the fold and the primary bifurcation. Below that, until

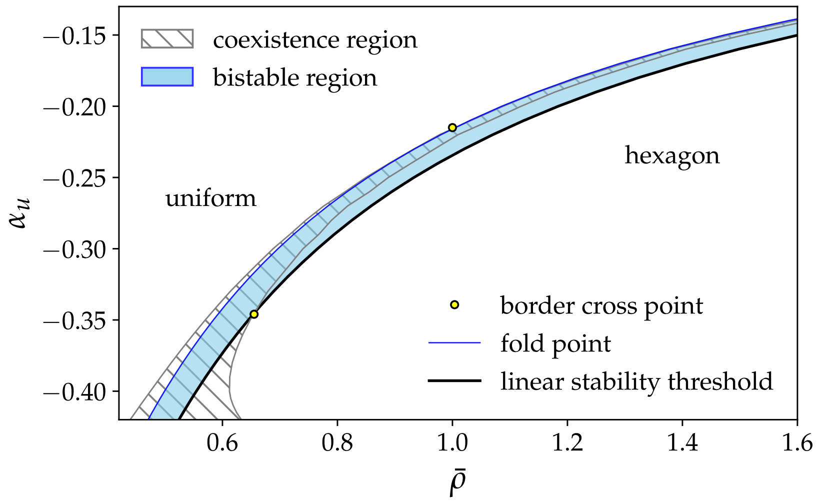

Fig. 5.9: Phase diagram of the local approximation in 2D, spanned by $\bar{\rho}$ and α_u. Every parameter combination above the primary bifurcation (black line) allows for uniform solutions, while any parameters below the hexagon fold bifurcation (blue line) allows for a hexagon pattern. Given a system with no localized states the region between those line (light blue) is bistable. The grey striped region marks the coexistence region within which localized states can be found. This region, at different parameters crosses both the primary bifurcation and the hexagon folds, as marked by a black circle.

roughly $\bar{\rho} = 0.64$ (second black circle) the coexistence region is above the primary bifurcation but reaches beyond the fold bifurcation. Finally, for even smaller mean densities the higher density border of the coexistence region is at higher densities than the primary bifurcation. Eventually, at about $\bar{\rho} = 0.61$ the position of that border of the coexistence region no longer decreases with α_u. Instead, it turns back towards higher densities. As this is at values of α_u close to where negative densities make the system both numerically unstable and physically questionable any consequences should be considered to be potentially suspect.

Fig. 5.10 tracks the same properties as Fig. 5.9, except for the nonlocal and unscaled system, with the bistable region and fold point now marked in red. Most previous observations hold true for this system, with the exception of the coexistence region passing the linear stability threshold or having a turning point towards higher mean densities, which theoretically might still be possible at lower densities, but would require negative values of a. The point where the coexistence region crosses the fold bifurcation line here is at $\bar{\rho} \approx 14.8$

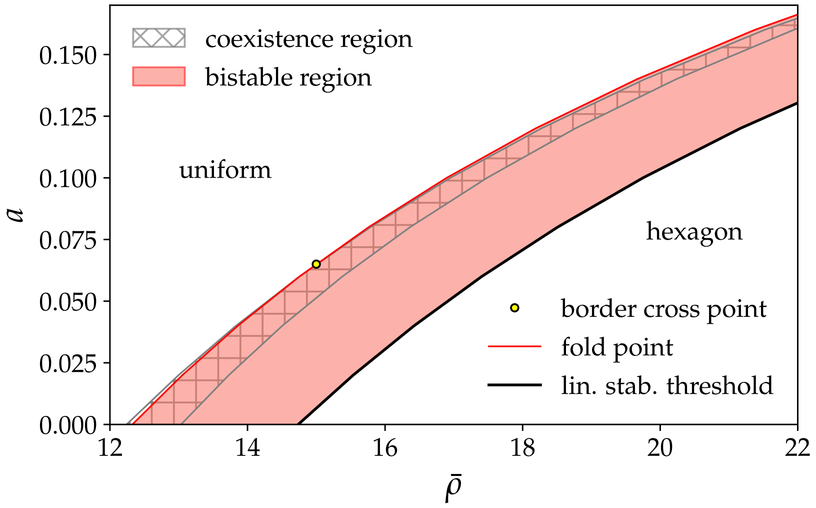

Fig. 5.10: Phase diagram of the nonlocal model in 2D spanned by the unscaled mean density $\bar{\rho}$ and scattering length a. Area and line styles are as in Fig. 5.9, except blue is replaced by red.

For a direct comparison Fig. 5.10 is scaled to match the local approximation, with the results given in Fig. 5.11. The coexistence region, as expected from Fig. 5.5 is wider for the nonlocal model. The points where the fold lines cross the border of the coexistence region are relatively close together at $\bar{\rho} = 1$ (local) vs $\bar{\rho} = 1.04$ (nonlocal).

5.5 Simplified Model with Higher-Order Nonlinearities

As already mentioned in Sec. 5.1, higher-order nonlinearities, specifically in form of the quantum fluctuation term $\gamma_{\mathrm{QF}}|\psi|^3\psi$ introduced in Eq. (5.10), can stabilize otherwise inaccessible patterns, as well as impact the stability region [196, 197, 79] and potentially turn the hexagon phase transition into a second order transition [196].

Such quantum fluctuations appear for dipolar systems, their addition to the present model is therefore purely illustrative, aiming to understand the bifurcations involved in the emergence of new phases, as well as the resulting changes to bifurcation diagrams. Generally, the parameter values for quantum fluctuations are very low and dependent on the scattering length. Neither constraint is considered here, meaning a wider range of phenomena can be analyzed.

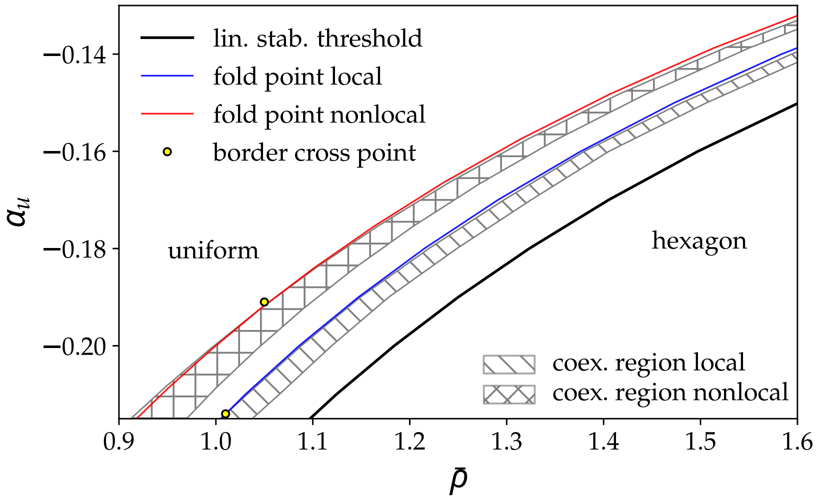

Fig. 5.11: Phase diagram of both the nonlocal model (see Fig. 5.10) and local approximation (see Fig. 5.9) in 2D spanned by the scaled parameters $\bar{\rho}$ and α_u. Again the linear stability border is marked in black, matching for both systems. For the nonlocal model the fold is given in red, with the coexistence region marked by a grey cross pattern. For the local approximation the fold is marked in blue and the coexistence region through grey stripes. Any point where the coexistence region border crosses a fold bifurcation is marked by a black circle.

Following the steps outlined in Sec. 5.3 for the GPE with quantum fluctuations, Eq. (5.10) gives the local approximation with an additional term compared to Eq. (5.31). Consequently, the rescaling has to be extended to that term, leading to

$$b \to \gamma_{\mathrm{QF}} \frac{\alpha_u + 1}{g_0} \sqrt{\frac{2}{-g_2}}\,, \tag{5.53}$$

and therefore the state equation

$$\partial_t \rho = \Delta \left[\frac{(\nabla\rho)^2}{8\rho^2} - \frac{\Delta\rho}{4\rho} + (\alpha_u + 1)\rho + 2\Delta\rho + \Delta^2\rho + b\rho^{3/2} \right]\,, \tag{5.54}$$

with accompanying free energy functional

$$F = \int_V \mathrm{d}^n r \left[\frac{|\nabla\rho|^2}{8\rho} + b\frac{2}{5}\rho^{5/2} + \frac{(\alpha_u + 1)}{2}\rho^2 + \rho\Delta\rho + \frac{\rho}{2}\Delta^2\rho \right]\,. \tag{5.55}$$

To match the border of linear stability of the nonlocal model with critical values k_c and $\bar{\rho}_c$, the specific values for g_0, g_2 and g_4 have to be set to

$$g_0 = \frac{2\hat{U}(k_c) + 4k_c\partial_k\hat{U}(k_c) + k_c^2\partial_{kk}\hat{U}(k_c)}{8} + \frac{3k_c^2}{8\bar{\rho}_c} - \frac{9b\sqrt{\bar{\rho}_c}}{8}\,, \tag{5.56}$$

$$g_2 = -\frac{1}{k_c^2}\left(2g_0 + \frac{k_c^2}{4\bar{\rho}_c} + 3b\sqrt{\bar{\rho}_c}\right)\,, \tag{5.57}$$

$$g_4 = \frac{1}{k_c^4}\left(g_0 + \frac{3}{2}b\sqrt{\bar{\rho}_c}\right)\,. \tag{5.58}$$

$\partial_k\hat{U}$ and $\partial_{kk}\hat{U}$ represent the first and second derivatives of $\hat{U}$ with respect to k.

5.5.1 Influence on Linear Stability

Again, the stability for the nonlocal model is determined according to Sec. 5.2.2, leading to something close to Eq. (5.30), but with an additional term:

$$\omega'^2(k) = \omega^2 + \frac{3}{2}k^2\gamma_{\mathrm{QF}}\sqrt{\bar{\rho}}^3\,. \tag{5.59}$$

From there, using $\omega'^2 = 0$ and $\frac{\partial\omega'^2}{\partial k} = 0$ leads to the critical values, which, for the nonlocal model take the form

$$\bar{\rho}_c = -\frac{k_c}{2\hat{R}_k(k_c)} \tag{5.60}$$

$$\gamma_{\mathrm{QF}c} = -\frac{2}{3\sqrt{\bar{\rho}_c}^3}\left[\frac{k_c^2}{4} + \rho_c(\hat{R}(k_c) + a_c)\right] \tag{5.61}$$

$$a_c = -\left[\frac{k_c^2}{4\bar{\rho}_c} + \frac{3}{2}b_c\sqrt{\bar{\rho}_c} + \hat{R}(k_c)\right] \tag{5.62}$$

$\bar{\rho}_c$ must be set to get k_c from Eq. (5.60). Then either a or γ_{QF} must be set to get $\gamma_{\mathrm{QF}c}$ or a_c, respectively. This results in a border of linear stability as depicted in Figs. 5.12 and 5.13 for one and two dimensions, respectively. The border is indicated by a black line for different values of γ_{QF} indicated by different line styles. Above these curves the uniform state is stable.

For the approximated system the critical wavelength is

$$k_0^2 = 1 - \frac{1}{8\bar{\rho}}\,, \tag{5.63}$$

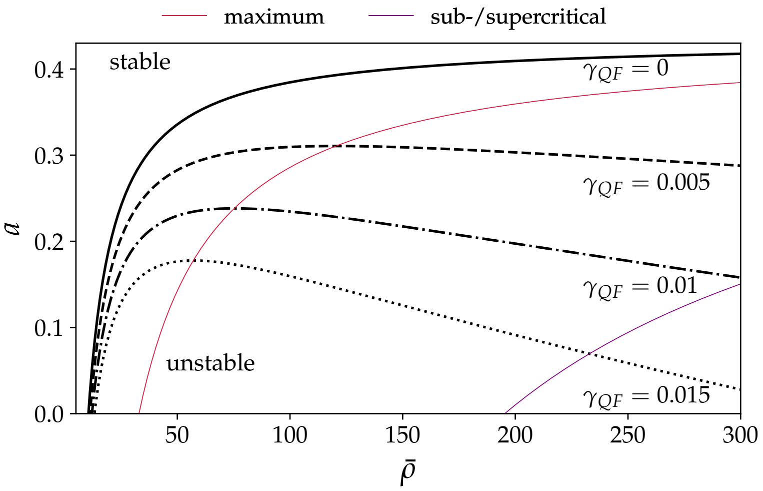

Fig. 5.12: Linear stability region of the uniform (superfluid) state $\rho(x) = \bar{\rho}$ in the $(\bar{\rho},\, a)$-plane in 1D. The stability thresholds according to Eq. (5.62) are given as black lines of various styles representing different values of the strength of the higher-order nonlinearity, as indicated at the curves. The regions above the respective lines correspond to stable uniform states. The thin red line indicates the position of the maximum a_m of the curves when continuously changing γ_{QF}, while a_s indicates the position of the change between sub- and supercritical pitchfork bifurcation. Note that for $b \to 0$ the corresponding $\bar{\rho}$ also diverges. To the left [right] of the purple line the primary bifurcation is a supercritical [subcritical] pitchfork.

with the accompanying border of linear stability

$$\alpha_{uc} = \left(1 - \frac{1}{8\bar{\rho}}\right)^2 - 1 - \frac{3}{2} b\sqrt{\bar{\rho}} \qquad \text{for} \qquad \bar{\rho} \geq \tfrac{1}{8}\,, \tag{5.64}$$

where α_{uc} is the critical value of α_u. It is depicted in Fig. 5.14 for different values of b as black lines of various styles. Again uniform states above those curves are stable.

It is immediately obvious that in all three depictions the addition of the higher-order nonlinearity leads to significant changes in the phase diagram as expected according to Ref. [196]. They add a maximum to the border of linear stability, extending the region of stable uniform states toward smaller values of a and α_u, as well as toward larger values of $\bar{\rho}$. The position of the maximum is indicated by the

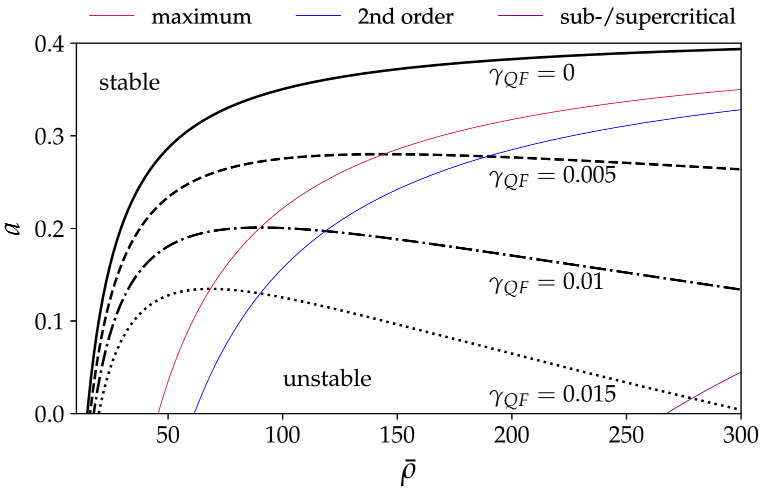

Fig. 5.13: Linear stability region of the uniform (superfluid) state $\rho(x) = \bar{\rho}$ in the $(\bar{\rho},\, a)$-plane in 2D, with line styles as in Fig. 5.12. The purple line is now only applicable to the striped solution. In addition, there is a point where the hexagon/honeycomb branches of the primary bifurcation exchange direction and stability. This 4 phase point a_p is indicated by the crossing of the border of linear stability with the blue curve. To the left [right] of this crossing the first stable pattern is the hexagon [honeycomb]. In both cases the transition is of first order.

crossing of said border with the red line, given by

$$a_m = -\hat{R}(k_c) - \frac{5}{4}\frac{k^2}{\bar{\rho}} \qquad\qquad \alpha_{um} = \frac{5}{64\bar{\rho}^2} - \frac{3}{4\bar{\rho}}\,. \tag{5.65}$$

Without quantum fluctuations the border of linear stability and the red maximum line never cross but converge for $\bar{\rho} \to \infty$.

5.5.2 Changes to Patterns and Phase Transition

From there additional stability regions of different patterns and the order of the phase transitions can be approximated using a one-mode approximation. To do so the patterned state is approximated by harmonics of a single wavelength with small amplitude $\bar{\rho}A$ with $A \ll 1$. This is either

$$\rho = \bar{\rho} + \bar{\rho}A\sum_{i=1}^{3}\cos\left(\mathbf{k}_i\mathbf{r}\right) \tag{5.66}$$

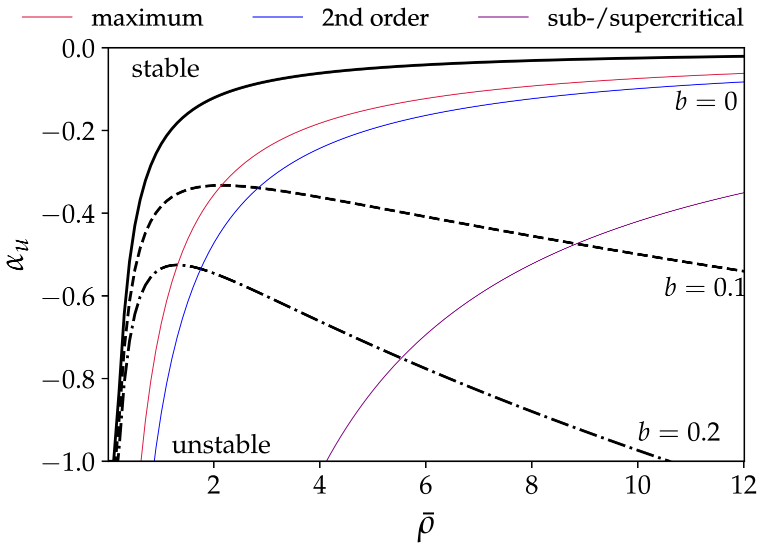

Fig. 5.14: Linear stability region of the uniform (superfluid) state $\rho(x) = \bar{\rho}$ in the $(\bar{\rho},\, \alpha_u)$-plane. The line styles match those of Figs. 5.12 and 5.13, though with different values of b as indicated at the curves.

for hexagons [honeycomb] with $A > 0$ [$A < 0$] or

$$\rho = \bar{\rho} + \bar{\rho} A \cos(\mathbf{k}_1 \mathbf{r}) \tag{5.67}$$

for one dimensional solutions or stripes in two dimensions. The lattice vectors $\mathbf{k}_i$ are $\mathbf{k}_1 = (k, 0)$, $\mathbf{k}_2 = (-k/2, k\sqrt{3}/2)$ and $\mathbf{k}_3 = (-k/2, -k\sqrt{3}/2)$.

This ansatz is then inserted into the free energy and the result approximated by way of a Taylor expansion in $A \ll 1$. This results in an equation of the form

$$F - F_0 = q_2 A^2 + q_3 A^3 + q_4 A^4 + \mathcal{O}(A^5)\,. \tag{5.68}$$

where $F_0 = F(A = 0)$ is the uniform ground state free energy. As the modulation amplitude A is small close to the border of linear stability, this is a reasonable approximation close to the primary bifurcation and any points of interest directly influencing the type of bifurcation should be qualitatively correct, though still deviate quantitatively. As the border of linear stability is also the point where nonlocal model and local approximation agree the one-mode approximation is done only for the local approximation, meaning F has the form given in Eq. (5.55).

From there Eq. (5.68) is minimized with respect to k, i.e., $\partial_k F = 0$, leading to the critical wavenumber k_c, which still depends on A. Inserting k_c into Eq. (5.68) and truncating at $\mathcal{O}(A^5)$ leads to the results in Tab. 5.1.

	hexagons/honeycomb	1D/stripes
q_2	$\frac{192\alpha_u\bar{\rho}^2+48\bar{\rho}+288b\sqrt{\bar{\rho}}^5-3}{256}$	$\frac{64\alpha_u\bar{\rho}^2+16\bar{\rho}+96b\sqrt{\bar{\rho}}^5-1}{256}$
q_3	$\frac{-24\bar{\rho}+48b\sqrt{\bar{\rho}}^5+3}{256}$	0
q_4	$\frac{240\bar{\rho}-90b\sqrt{\bar{\rho}}^5-33}{1024}$	$\frac{8\bar{\rho}-3b\sqrt{\bar{\rho}}^5-1}{512}$

Table 5.1: Prefactors to the amplitudes in the energy equation (Eq. (5.68)) of the one mode approximation up to fourth order, depending only on the model parameters.

For a striped or 1D pattern the sign of the prefactor q_4 distinguishes between super- ($q_4 > 0$) and subcritical ($q_4 < 0$) pitchfork bifurcation. The former is true for all valid densities at $b = 0$ as seen, e.g., in Fig. 5.5 or Fig. 5.7. For $b > 0$ on the other hand this is no longer the case. To find the exact point of change, the border of linear stability equation (Eq. (5.64)) is solved with respect to b and introduced into q_4, leading to $q_4 = \dfrac{64\alpha_u\bar{\rho}^2 + 272\bar{\rho} - 33}{16384}$, meaning anywhere

$$a_s = -\hat{R} - \frac{19}{4}\frac{k^2}{\bar{\rho}} \qquad\qquad \alpha_{us} = \frac{33}{64\bar{\rho}^2} - \frac{17}{4\bar{\rho}} \tag{5.69}$$

crosses the border of linear stability the bifurcation changes.

The resulting information is added as a purple line to the Figs. 5.14, 5.12 and 5.13. To the left of the crossing point the bifurcation is supercritical, to the right, it is subcritcal. It becomes immediately obvious that a minimum density is required for this effect to appear. For the approximated system, e.g., it requires $\bar{\rho} > 4.125$.

In addition there are more expected changes [196, 197, 79] to the phase diagram, as depicted in Fig. 5.15, which gives an overview over the most energetically favorable phases in the $(\bar{\rho}, b)$-plane, given by the one-mode approximation.

Under the limitation that this approximation becomes more inaccurate the further away it is from the primary bifurcation, it is still possible to conclude that the hexagon pattern is the ground state in the lower density region within the black lined region where the uniform ground state is linearly unstable. The honeycomb pattern, however, is dominant in higher density regions, while the stripes occupy a region in between the two.

An important observation is that the hexagon and honeycomb patterns can be the most stable state even outside of the border of linear stability, suggesting a region of bistability between the respective patterns and the uniform state, and therefore a first order phase transition.

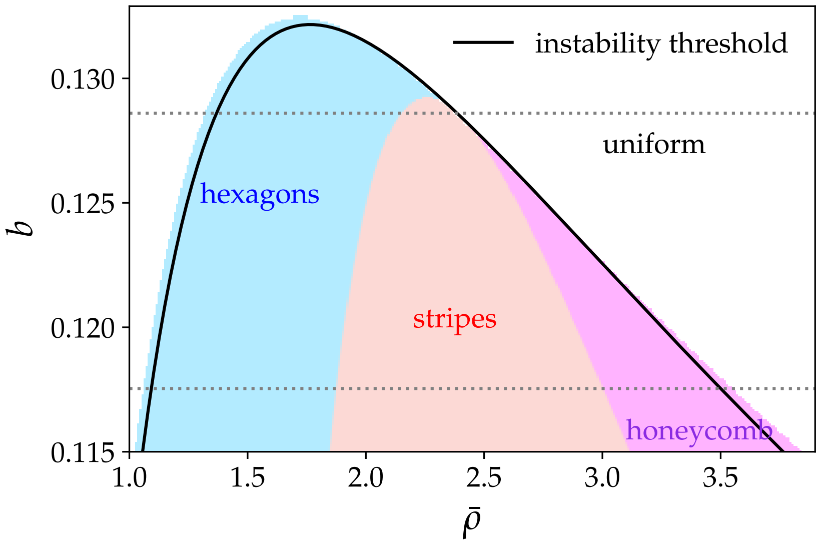

Fig. 5.15: Energetically favored ground states in the $(\bar{\rho}, b)$-plane as obtained in a one-mode approximation at $\alpha_u = -0.4$. The border of stability, Eq. (5.64), is given as black line. The ground states are the uniform state (white region), hexagons (light blue), stripes (light red) and honeycomb (light purple). All four meet in a single point, where no bistability with the uniform state exists. Horizontal dashed lines indicate b-values employed for the bifurcation diagrams in Figs. 5.16 and 5.17.

There is a point where all three patterns as well as the uniform state touch. At this point the bistable region shrinks to zero for both the hexagon and honeycomb pattern, suggesting a second order phase transition. This "four phase point" is indicated in the one-mode approximation via a change of sign of q_3. Similar to the sub-/supercritical pitchfork the intersection of $q_3 = 0$ and Eq. (5.64) gives

$$a_p = -\hat{R} - \frac{3}{2}\frac{k^2}{\bar{\rho}} \qquad\qquad \alpha_{up} = \frac{7}{64\bar{\rho}^2} - \frac{1}{\bar{\rho}}\,. \tag{5.70}$$

In the phase diagrams in Figs. 5.13 and 5.14 this is indicated by a blue line, above [below] which the hexagon [honeycomb] phase is the dominant phase at the primary bifurcation.

To substantiate the results of the one-mode approximation bifurcation diagrams of interesting points in the higher order system are depicted below. The four phase point can be found in the bifurcation diagram in Fig. 5.16 with $\bar{\rho}$ as control parameter of a two-dimensional system at $\alpha_u = -0.4$ at $b = 0.1286$ (along the upper horizontal line in Fig. 5.15). The domain size is again chosen to fit hexagonal states with $2L_c/\sqrt{3} \times 2L_c$.

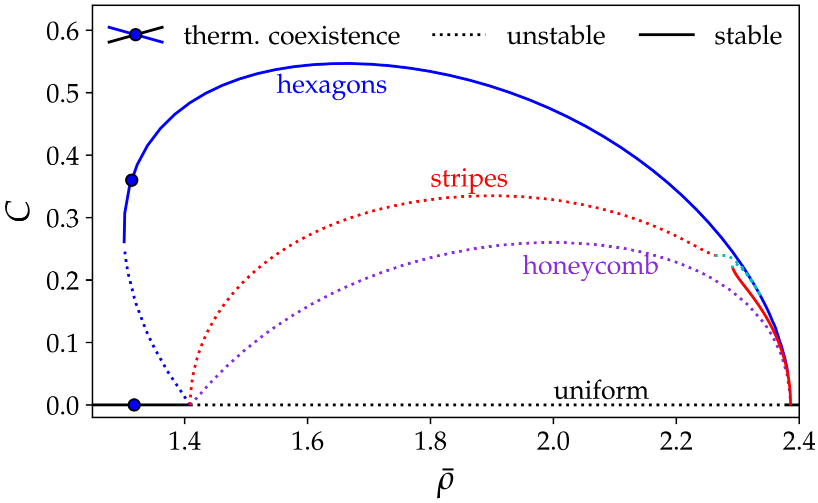

Fig. 5.16: Bifurcation diagram showing branches of steady states of Eq. (5.54) as a function of $\bar{\rho}$ at fixed $\alpha_u = -0.4$ and $b = 0.1286$ (along the upper horizontal line in Fig. 5.15). The considered 2D system has domain size $2L_c/\sqrt(3) \times 2L_c$. The solutions are characterized through the contrast C (see Eq. (5.14)). Line styles are as in Fig. 5.7 with the addition of intermediate states between stripes and hexagons in cyan. The bifurcation at low $\bar{\rho}$ is related to points of thermodynamic coexistence between the uniform and hexagon states (indicated by filled circles). No such coexistence occurs related to the bifurcation at high $\bar{\rho}$ indicating a second order transition.

It shows two bifurcations from uniform to patterned state, one at lower densities and one at higher densities. The lower density bifurcation at $\bar{\rho} \approx 1.35$ retains all the same qualities already seen in the previous sections for $b = 0$, including multistability with the hexagons as well as a small coexistence region, making it a first order phase transition. The new bifurcation is exactly on the predicted four phase point, specifically at $\bar{\rho} \approx 2.4$. At this point both stable hexagons (blue) and stripes (red) as well as the unstable honeycomb state (purple) emerge vertically, leaving no bistable region, i.e., the transcritical hexagon/honeycomb part of the bifurcation is at exactly 90 degree with respect to the uniform state. In addition, there are no points of identical chemical potential and grand potential density and therefore no coexistence, making this a second order phase transition. The stripe state is only stable in a narrow region, after which it exchanges stability with a stripe-hexagon transition state (light blue) which heads back towards the primary bifurcation. The one-mode approximation indicated that the energy of the stripe phase would be lowest, right at the four phase point, however, for the present bifurcation diagram the energy of the stripe and hexagon phase near the higher density bifurcation are practically indistinguishable, making a clear distinction whether the stripe phase really is the first stable phase difficult. For the nonlocal model the results look very similar, while all the bifurcations show the same nature, if not position (not shown).

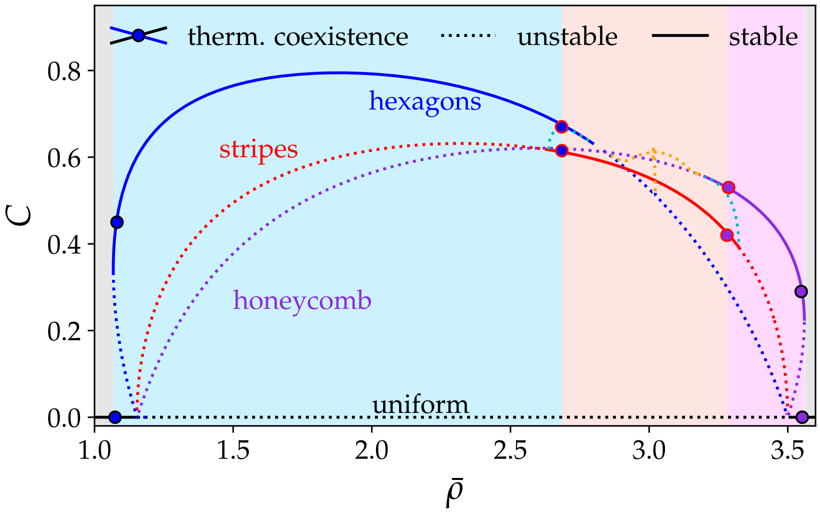

Fig. 5.17: Bifurcation diagram at $\alpha_u = -0.4$ and $b = 0.1175$ (along the lower horizontal line in Fig. 5.15). Domain size, line styles, solution measure and markers are as in Fig. 5.16. The additional dotted orange lines correspond to intermediate states between hexagons and honeycombs. The background shading locally matches the colors of the respective ground state. Thermodynamic coexistence of pairs of states is marked by filled circles: the two colors of filling and edge refer to the respective coexisting states.

Figure 5.17 shows an example bifurcation of a region with a stable honeycomb pattern, specifically at fixed $\alpha_u = -0.4$ and $b = 0.1175$ (along the lower horizontal line in Fig. 5.15). The bifurcation diagram is shaded to specify the regions in which the four possible patterns are globally stable. Starting at low $\bar{\rho}$, the uniform state (black line, grey shading) is energetically favored up to $\bar{\rho} = 1.07$, followed by hexagons (blue line, light blue shading) up to $\bar{\rho} = 2.7$. Then follows the stripe pattern (red line, light red shading) which has the lowest energy until $\bar{\rho} = 3.28$ where honeycombs (purple line, rose shading) take over. Finally, at $\bar{\rho} = 3.56$ the uniform state once again becomes dominant.

All these regions have transitions between them, each with their own set of coexisting states with identical chemical potential and grand potential density. They are marked with circles colored with the branch color of those same coexisting states and are at near identical values of $\bar{\rho}$ with the difference being of order 10^{-2} or lower. Consequently, the coexistence region is too narrow to actually find localized states within the given domain, however, even without them the transitions are of first order.

The first bifurcation at lower densities behaves just like all previously discussed uniform-hexagon transitions. At higher densities are the two transitions which bracket a range of stable stripe pattern, with bifurcations linking it to hexagons (lower density) or honeycomb (higher density). The connecting unstable branches (light blue) consist of intermediate shapes of stripes and hexagons/honeycombs as depicted in Fig. 5.18, starting from a hexagon (leftmost image) passing such an intermediate state before transforming into a stripe (central image), after which it transitions into a honeycomb (rightmost image)[3].

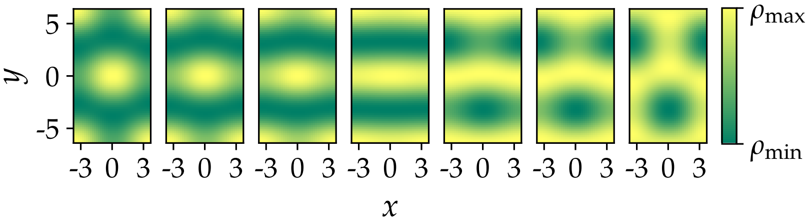

Fig. 5.18: Examples of steady patterns illustrating the change from hexagons to stripes and further to honeycombs in Fig. 5.17 (for parameters see its caption). The sequence is as follows: From left to right there is a stable hexagon at $\bar{\rho} = 2.75$, unstable intermediate states at $\bar{\rho} = 2.7$ and $\bar{\rho} = 2.69$, a stable stripe at $\bar{\rho} = 2.67$, unstable intermediate states at $\bar{\rho} = 3.27$ and $\bar{\rho} = 3.25$, and a stable hexagon at $\bar{\rho} = 3.19$.

Finally, the higher density bifurcation is much like the one for the uniform hexagon transition, i.e., seemingly transcritical with respect to hexagons and honeycomb, except this time it is the honeycomb branch which points towards higher densities, before turning back in a fold.

---

[3] The latter image of a shifted honeycomb explains the necessity of using periodic BCs to find the state and the accompanying bifurcations, as it is impossible to realize with Neumann BCs. The reverse is true when transitioning from a honeycomb back towards hexagon states.

The small gap in the branch connecting stable and unstable hexagons [honeycombs] is due to the numerical grid of the domain not quite matching the corresponding pitchfork bifurcation, meaning the symmetry of the involved pattern is not reflected well enough. It is from here that further unstable intermediate states branch off to connect the hexagon and honeycomb states (orange lines). They form triangles and patchwork quilt patterns (as in Ref. [85], chapter 5.4). Further branches may bifurcate from these states, but they should all be unstable, meaning they only become relevant during time evolution, where unstable states may first attract and then repel the evolution.

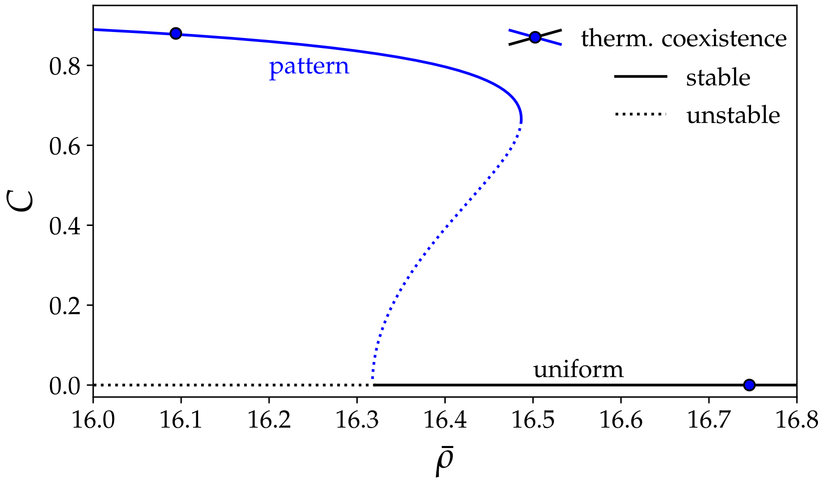

Fig. 5.19: Bifurcation diagram in 1D at $\alpha_u = -0.5$ and $b = 0.08$. Domain size is $L_x = 8L_c$, line styles, solution measure and markers are as in Fig. 5.16. Thermodynamic coexistence of pairs of states is marked by filled circles.

Finally, there is the change in 1D from super- to subcritical pitchfork bifurcation, an example of which is given for the approximated system for $\alpha_u = -0.5$ and $b = 0.08$ in Fig. 5.19, simulated on a domain of size $L_x = 8L_c$. The primary bifurcation is indeed a subcritical pitchfork at the expected value of $\bar{\rho} = 16.317$. It is followed by a saddle-node bifurcation at $\bar{\rho} = 16.48$ on the patterned branch (blue), where the branch turns towards lower densities.

There is also a coexistence of a patterned and a uniform state, as indicated by the blue filled circles, which indicate the existence of localized states. Those states can, however, not be found in the given domain, indicating an interface region of sizes

$> 8L_c$. As simulating bigger systems causes numerical problems their existence here remains theoretical.

5.6 Dipolar BECs in an Infinite Tube

The discovery that dipolar BECs can self-organize into a supersolid or isolated droplets due to stabilizing effects of beyond mean-field contributions [109, 108, 189, 160] led to a variety of experiments, many performed in a tube-like setup [90, 164, 39, 177, 178, 26], i.e., the potential V_{ext} traps the BEC such that the dipoles have a side-by-side orientation along the axial, unconfined direction z and are strongly confined in the polarization direction y of the dipoles and the remaining direction x. In consequence, all pattern formation is along the z-axis, making the system quasi one-dimensional. A schematic is shown in Fig. 5.20.

In such a trap the superfluid-supersolid phase transition can be of first or second order [23, 168, 161], as determined through complex time-evolution and comparison of the energies of the converged states. This is generally done under the assumption of small domains, which do not support localized states. In consequence, the order of the phase transition in those works is determined by only taking the primary bifurcation into account.

The following results are under consideration to be published. A pre-print version can be found in Ref. [172].

5.6.1 Full Three-Dimensional Model

To match the experiments an ensemble of N ^{164}Dy atoms with mass $m = 163.93\,\mathrm{u}$ is considered at zero temperature. The atoms interact via both collisions and dipolar long-range interactions, characterized by a_s and $a_{dd} = m\mu_0\mu_m^2/12\pi\hbar^2 = 130.8\,a_0$, respectively. Here μ_m is the magnetic moment, and μ_0 the magnetic constant, while a_0 is the Bohr radius.

The accompanying interaction is described by

$$U_{\text{eff}}(\mathbf{r}) = \frac{\hbar^2}{m}\left(4\pi a_s\delta(r) + \frac{3a_{dd}}{r^3}\left(1 - 3\frac{y^2}{r^2}\right)\right) \tag{5.71}$$

$$\hat{U}_{\text{eff}}(\mathbf{k}) = 4\pi\frac{\hbar^2}{m}\left(a_s + a_{dd}\left(3\frac{k_y^2}{k^2} - 1\right)\right)\,. \tag{5.72}$$

in real and Fourier space [13]. Finally, the quantum fluctuations are given by [109, 108]

$$\gamma_{QF} = \frac{\hbar^2}{m} 4\sqrt{\pi}\frac{32}{3}\sqrt{a_s}^5 \int_0^1 \mathrm{d}u \left(1 + \frac{a_{dd}}{a_s}(3u^2 - 1)\right)^{5/2} , \tag{5.73}$$

and the trapping potential by

$$V_{\text{ext}}(\mathbf{r}) = V_{\text{ext}}(x, y) = \frac{1}{2}\omega^2(x^2 + y^2) , \tag{5.74}$$

with the trapping frequency $\omega = 150 \cdot 2\pi\,\text{Hz}$. Furthermore, the wave function is normalized to the total particle number $N = \int |\psi|^2 d^3r$, with the mean density $\bar{\rho} = N/L$ and tube length L. The one-dimensional density is $\rho(z) = \int |\psi|^2 dxdy$.

The subsequent dynamics can be approximated by the extended GPE (5.10) with the accompanying energy (5.11).

5.6.2 One-Dimensional Approximation with a Gaussian Profile

To reduce the dimensionality of the problem the profile of the BEC in the $(x, y)-$plane is considered to be Gaussian (see Refs. [22, 23]), i.e., $\psi(\mathbf{r}) = \psi_{\|}(z)\psi_{\perp}(x, y)e^{-it\mu/\hbar}$ with chemical potential μ and

$$\psi_{\perp}(x, y) = \frac{1}{\sqrt{\pi}l} e^{-(\eta x^2 + y^2/\eta)/2l^2} . \tag{5.75}$$

Here l represents the mean width, while η represents the anisotropy, caused by the interaction of the dipoles. Fig. 5.20 illustrates the two parameters as well as the critical length scale in z-direction. As the Gaussian can be integrated out, the one-dimensional density becomes $\rho(z) = |\psi_{\|}(z)|^2$.

After performing the integration in x and y-direction, the BEC can be described by the energy [22, 23]

$$E = E_{\perp} + \frac{\hbar^2}{m}\frac{1}{\bar{\rho}L}\int_{uc} \mathrm{d}z\, \psi_{\|}^* \left(-\frac{1}{2}\frac{d^2}{dz^2} + \frac{1}{2}(U * |\psi_{\|}|^2) + \frac{2}{5}g_{QF}|\psi_{\|}|^3\right)\psi_{\|} \tag{5.76}$$

with uc representing a unit cell. $E_{\perp}$ is the effective energy contribution of the structure in x-y-direction

$$E_{\perp} = \frac{\hbar^2}{m}\frac{1}{4}\left(\eta + \frac{1}{\eta}\right)\left(\frac{l^2 m^2 \omega^2}{\hbar^2} + \frac{1}{l^2}\right) . \tag{5.77}$$

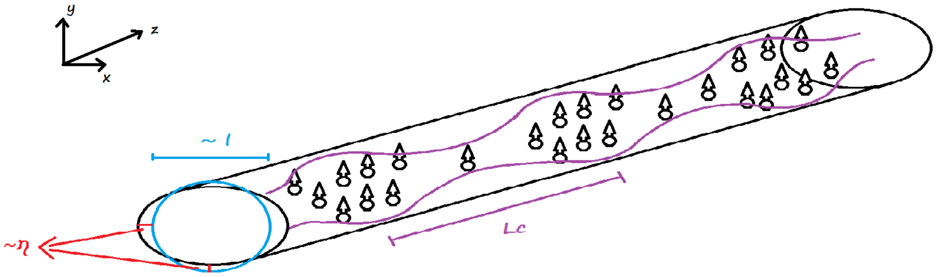

Fig. 5.20: Sketch of the considered geometry, explaining the parameters η, l and L_c. η is a measure of the anisotropy of the profile, while l gives the overall width of the Gaussian. Finally, L_c is the characteristic length of the pattern.

g_{QF} is the coefficient for the quantum fluctuations and takes the form

$$g_{QF} = \frac{256}{15\pi}\frac{a_s^{5/2}}{l^3}\left(1 + \frac{3a_{dd}^2}{2a_s^2}\right) . \tag{5.78}$$

It contains a further approximation [21] of the integral in Eq. (5.73) in addition to the changes due to the Gaussian profile.

The interaction in Fourier space is now described by [22, 23]

$$\hat{U}_{\text{eff}}(k) = \frac{2}{l^2}\left[a_s + a_{dd}\left(\frac{3(Qe^Q\text{Ei}(-Q))}{\eta+1} - 1\right)\right] . \tag{5.79}$$

Here Q represents $Q = \sqrt{\eta}k^2l^2/2$, while $\text{Ei}(x)$ is the exponential integral function, meaning $\text{Ei}(-x) = \int_{-\infty}^{s} e^s/s ds$.

From here the usual GPE (taking the form of Eq. (5.10) with $V_{\text{ext}} = 0$) can be used, under the condition that η, l and L_c are adapted to minimize the energy in Eq. (5.76). The accuracy of such an approximation is fairly good on a qualitative level, but doesn't fit quantitatively, as shown in Ref. [168].

5.6.3 Results

The Gaussian profile approximation facilitates the application of path continuation for the uniform and patterned states, though the patterned results need to be refined with complex-time evolution. Localized states, however, can not be accounted for as the front between uniform and patterned part would require a gradient between the coexisting values of η and l.

To circumvent this the following results are considered at constant η and l, their values chosen to match the primary bifurcation. For $a_s = 98a_0$ they are set to $l = 1.146$ and $\eta = 5.808$. The resulting bifurcation diagram is depicted in Fig. 5.21.

Fig. 5.21 (a) shows the contrast C (Eq. (5.14)) as a function of the one-dimensional mean density $\bar{\rho} - \bar{\rho}_c$ where $\bar{\rho}_c = 6060.49/\mu\text{m}$ is the critical means density of the primary bifurcation. The uniform solution, representing a perfect superfluid (black), is linearly stable (solid lines) for densities higher than the critical density $\bar{\rho}_c$ and unstable (dotted lines) below it, the accompanying primary bifurcation (at expected $\bar{\rho} - \bar{\rho}_c = 0$) is a supercritical pitchfork and marked by a grey dot. From there a new linearly stable supersolid state (solid line, blue) emerges, featuring periodic density modulation.

Previous considerations of the phase transition in a tube shaped dipolar BEC, depending on the parameter region, categorized them as either first or second order, as determined through complex time-evolution on a small domain, therefore making it dependent on the nature of the primary bifurcation, while assuming the local mean density, i.e., the density profile gained when averaging over the individual unit cells, would remain uniformly distributed [23, 168]. Under these assumptions the presented bifurcation would give rise to a second order transition, as no localized states (red line) can develop.

However, when given a sufficiently large domain, localized states with their nonuniform local mean density distributions become possible, which in turn indicate a first order phase transition independent of the type of primary bifurcation.

Here, localized states (red line, example profiles i to iv in top row of Fig. 5.21) branch off from the supersolid branch (blue) in a subcritical bifurcation, which leaves both branches unstable. From there the localized states branch continues towards higher densities while the contrast C increases until it reaches a saddle-node bifurcation (state i). At the saddle-node the branch reaches its maximum density and stabilizes as it turns back towards lower $\bar{\rho}$. From there C plateaus until (at lower $\bar{\rho}$) there is another limiting saddle-node bifurcation (state iv) where the branch turns again, and destabilizes until it ends on the branch of supersolid states thereby stabilizing them.

In consequence there are two bistable regions, one for $\bar{\rho} > \bar{\rho}_c$ between uniform and localized state and another one at lower $\bar{\rho}$ between localized and regular periodic state. They bracket a region where the localized state is the only stable state.

Fig. 5.21 (b) takes a closer look at the bistable region at $\bar{\rho} > \bar{\rho}_c$ with respect to the energy particle density difference $\Delta E/N = (E - E_0)/N$ between the various states and the superfluid. The order of the phase transition now becomes obvious,

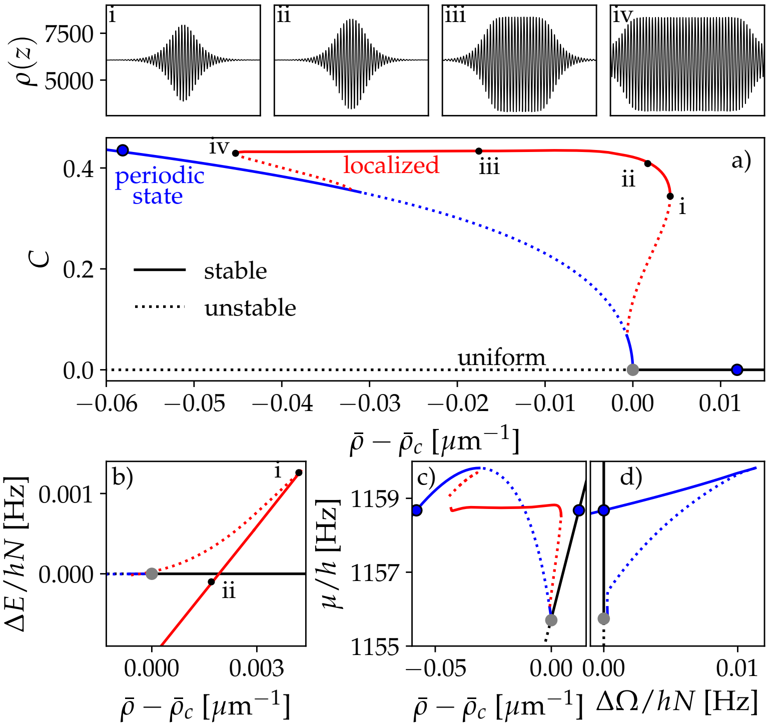

Fig. 5.21: Bifurcation diagram of the effective one-dimensional dipolar BEC model as a function of the mean density $\bar{\rho} - \bar{\rho}_c$ in terms of (a) contrast C, (b) mean energy per particle $\Delta E/N$ and (c) the chemical potential μ. Shown are branches of uniform perfect superfluid states (black), periodic states (blue) and of localized states (red). Solid [dotted] lines denote linearly stable [unstable] states. Profiles $\rho(z)$ of the localized states i-iv (also marked in (a) and (b)) are depicted in the top row. Panel b) shows that the energy of the localized state is lower (e.g., state ii) than the energy of the superfluid even for densities larger than the critical one ($\bar{\rho}_c$, gray circle), marking this as a first order phase transition. Panel c) depicts the chemical potential depending on the density, clearly showing the constant region in the localized states, connecting the two coexisting states. The latter are fully explained in panel d) where the crossing of two stable branches in the $(\Delta\Omega/N, \mu)$-plane ($\Delta\Omega/N$ is the grand potential per particle) gives the exact coexisting states marked in black ringed blue circles both here and in previous panels. The remaining parameters are $a_s = 98a_0$, $l = 1.1456$ and $\eta = 5.8077$.

as $\Delta E/N$ of the localized state crosses zero at a mean density $\bar{\rho} > \bar{\rho}_c$, making state ii more energetically favorable than the superfluid. Consequently, when decreasing the mean density from a sufficiently large value, there is a jump in the contrast when the system relaxes to state ii (under complex time evolution), making it a first-order phase-transition.

In Fig. 5.21 (c) a typical feature of localized states is highlighted. It shows the chemical potential μ as a function of the density, which for the stable parts of the localized branch is largely constant as it follows the Maxwell construction even outside the thermodynamic limit [181].

In Fig. 5.21 (d) the coexistence of states is further highlighted, as now the chemical potential is plotted over the grand potential difference to the superfluid per particle $\Delta\Omega/N = (\Omega - \Omega_0)/N$. The latter is usually only considered for finite T cases for BECs [66, 157, 162], however, this does not exclude the $T = 0$ case considered here.

The grand potential density allows to check for thermodynamic coexistence of the superfluid and patterned state, meaning states with the same $\Delta\Omega/N$ and μ. Such states indeed exists and their crossing is highlighted by a black rimmed blue dot in Fig. 5.21 (a,c,d). The interval of densities spanned by these points marks the area where localized states can exist. As the considered numerical box is finite, the actual existence region of the localized states is slightly smaller.

Given that $\bar{\rho}_c = 6060.49/\mu\text{m}$ the considered values of $\bar{\rho} - \bar{\rho}_c$ are comparatively small, meaning while localized states exist and influence phase transitions, their existence region is very small, making them hard to find in more complicated simulations, but not impossible: Fig. 5.22 shows a localized state for the full 3D model (cf. Sec. 5.6.1) at $a_s = 91a_0$ and $\rho = 5250/\mu\text{m}$.

The state is contextualized in Fig. 5.23[4]. Panel (a) gives the contrast with respect to the mean density for the uniform states (black, example: top row, right) regularly patterned states (blue, example: top row, middle) and a localized state (red, example: top row, left). (b) shows the accompanying energy particle density difference to the uniform state, with the crossing marked by a gray dot, while (c) gives the crossing of the uniform and regularly patterned state in the $(\Omega/N, \mu)$-plane, marked by a black rimmed blue dot. As before these points of thermodynamic coexistence ($\bar{\rho}_{\text{coex periodic}} = 5237/\mu\text{m}$, $\bar{\rho}_{\text{coex superfluid}} = 5259/\mu\text{m}$) limit the interval where localized states can exist.

---

[4] The figure only contains results of complex time-evolution, as full bifurcation analysis in 3D is numerically still too taxing.

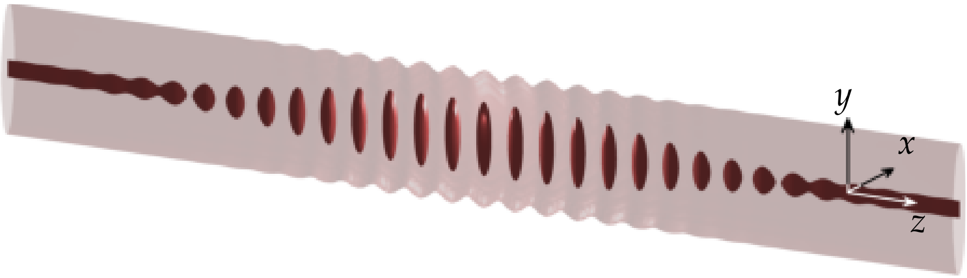

Fig. 5.22: Example of a stable localized state in a three-dimensional dipolar BEC. The dipoles are polarized along the y-direction, the BEC is tightly confined in the transverse direction, but unconfined in the z-direction (axially), leading to a tubular geometry. Even without a trap in z-direction, there exist stable localized states which feature a modulated supersolid in the central region and a perfect superfluid sufficiently far from it, i.e., there is an unequal distribution of the local average density. The parameters are $\bar{\rho} = 5250/\mu\text{m}$ and $a_s = 91a_0$. Contours are given at 1% (light) and 75% (dark) of the peak density. For ease of viewing the z-direction is compressed by a factor 7.

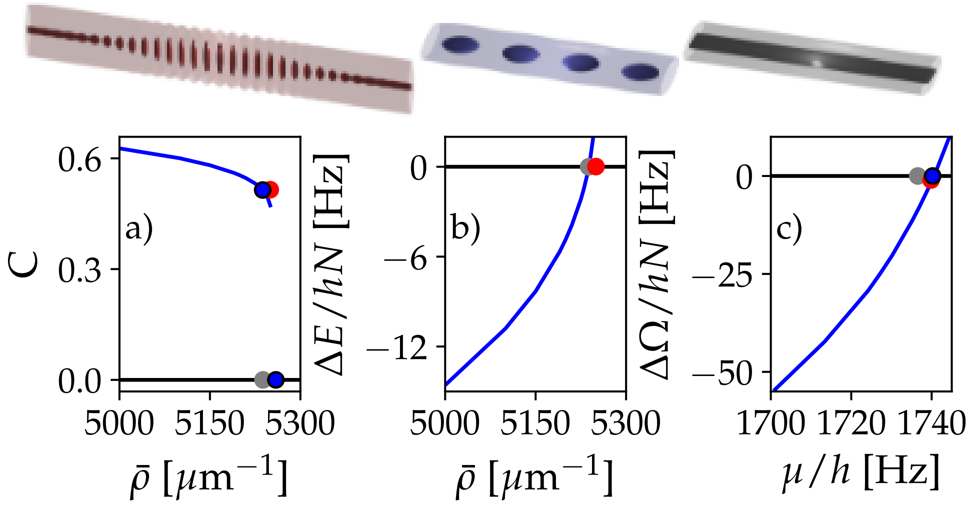

Fig. 5.23: Examples of states for a system of $\bar{\rho} = 5250/\mu\text{m}$ and and $a_s = 91a_0$ in top row: Localized state (left, red), periodic state (middle, blue) and superfluid (right, black) with contours at 1% (light) and 75% (dark) of the peak density. For ease of viewing the z direction is compressed by a factor 7 [2] for the localized state [periodic and superfluid states]. Panel (a) shows the contrast of the flat (black) and patterned (blue) states depending on the mean density, and also situates the localized state (red dot). The grey dot marks the energy cross between the uniform and regularly patterned state, found in panel (b), while panel (c) gives the grand potential density per particle with respect to the chemical potential. The crossing of the uniform and regularly patterned state (black rimmed blue dot) gives the coexistence, according to the Maxwell construction, which is also marked in panel (a).

6 Conclusion and Outlook

In this thesis phase transitions have been analyzed in a variety of systems ranging from passive to active and from classical to quantum level. Effects of different approximations, including dimensional reduction (assuming a profile in $x - y$ plane) and changes from nonlocal to local interactions have been considered. Specifically, their influence on spinodals, binodals, the order of the phase transition, the general existence of localized states and the behavior of their branches in bifurcation diagrams have been discussed.

The GEM-4 model, as an example of a classical, passive soft-matter model with nonlocal interactions has been analyzed specifically with an interest in the snaking behavior of localized state branches [29, 194, 98]. Snaking was expected to appear due to its prevalent existence region in the Phase-Field Crystal (PFC) model [182], which can be derived as a local approximation of the GEM-4 model [11, 86, 179, 50]. In this thesis it has been shown that the snaking of localized state branches in bifurcation diagrams is not part of the original model.

Tests of the different approximations used to get from the GEM-4 to the PFC model have shown that the lack of snaking is inherited by all of them, even the PFC model, as long as all parameters are set to match the original model perfectly. Differences appear only in the width and position of the coexistence region as well as the position of the folds on the localized states branch, which in turn is influenced by changes in the width of the interface between uniform and patterned part of a localized state.

If the approximation parameters do not perfectly match the original model (i.e., if only the original position of the primary bifurcation is maintained), then variation in the freed up parameters can qualitatively influence the behavior of localized state branches. Of the tested approximations the γ approximation, which replaces the Fourier expression of the convolution with a series in k^2 up to order k^4, does not lead to snaking for any parameter configuration, but does influence the width of the coexistence region. The ε approximation, which replaces the logarithm with a Taylor series up to ρ^4, however, influences the width of the interface region between localized pattern and the surrounding background. Consequently, the appearance of snaking and even the overall existence of localized states are subject to changes.

In summary, it has been shown, that the snaking in the PFC model is not a product of approximating the GEM-4, but rather of parameter sets which do not perfectly align with the original model. However, the option that other nonlocal models may produce snaking, e.g., due to a different interaction potential, cannot be ruled out. Consequently, future studies exploring which types of terms and potentials lead to snaking phenomena would prove intriguing.

Overall, the approximations, even when perfectly aligned with the original equation, only match up qualitatively to the full model, i.e., the bifurcation structure, including localized state branches remains unchanged, while showing significant differences on a quantitative level. Therefore, their easier implementation in path- and time-continuation software must be weighted against the need for the accurate results of a full model.

As an example of active soft matter an extended PFC model [190], capable of describing gas, liquid and crystal phases, has been coupled with a polarization field [80]. The result is a model capable of describing not only the previously mentioned phases, but also moving or living crystals and crystallites.

The influence of density-dependent and density-independent activity on phase boundaries and coexistence regions of the system has been of specific interest to this thesis. Of the two suggested kinds of activity the density-independent one was previously shown to destroy motility-induced crystallization (MIC) [124, 135, 134], while Ref. [80] also pointed out the suppression of motility-induced phase-separation (MIPS). Here, building on Ref. [80], it has been shown clearly that adding a density-dependent activity restores the MIPS and also some of the MIC.

In addition, rotating crystallites have been analyzed with respect to their size and angular velocity depending on the mean density $\bar{\rho}$ and temperature T. The crystallites have been shown to move like a rigid body while forming hexagonal or near hexagonal structures. Their behavior can by summarized as follows: Lower T and $\bar{\rho}$ lead to lower radii. The lower the radius the higher the angular velocity. The overall structure of a $R(T)$ diagram for fixed $\bar{\rho}$ has the form of stairs, i.e., plateaus of constant radius solutions, consisting of crystallites in various stages of filling out the outermost layer of peaks.

Very low values of T lead to coexistence between a uniform background and both stripe and hexagon patterns, which show additional types of movement such as shaking or swinging.

For future ventures, additional bifurcation diagrams around interesting points such as points with multiple coexistences could give further insight, especially when augmented with numerical continuation of traveling and rotating states.

Finally, on the quantum level, Bose-Einstein condensates (BECs) and their approximations close to the primary bifurcation have been analyzed.

To start with, tests on a Rydberg dressed nonlocal toy model [76, 41, 159, 115, 114, 40] and its local approximation [73] have proven the general existence of localized states in two dimensions (in accordance with Refs. [73, 5]), though it has been shown that the coexistence region might grow infinitely small depending on the parameter region.

Higher-order nonlinearities are shown to greatly affect the phase diagram in both one and two dimensions. In 1D they allow for first order phase transitions and localized states. In 2D they can stabilize the honeycomb and stripe patterns, as well as lead to a singular point with a second order phase transition, matching results in Ref. [196].

Overall no qualitative difference between nonlocal model and local approximation has been found, nor has there been evidence of snaking.

The more complex and realistic model of a dipolar BEC in an infinite tube [26, 39, 177] has similarly been tested for the existence of localized states. Both the approximated model of a Gaussian profile [23, 22] and the full three dimensional model [168] show localized states.

Additionally, the approximated model demonstrates an intricacy when determining the order of a phase transition (cf., e.g., Ref. [182]). The primary bifurcation is a supercritical pitchfork, which, on a superficial level, would seem to imply a second order phase transition. The existence of localized sates, however, indicates a first order phase transition, but requires a sufficiently large domain to support the interface region between the coexisting phases.

Further tests for regions with a supercritical pitchfork as a primary bifurcation would be interesting to augment the understanding of the phase transition on large domains. Especially helpful would be the realization of a comprehensive bifurcation analysis for the three-dimensional case. In addition, simulations of localized states in finite BECs, i.e., BECs with an additional trap in the z-direction with limited particle number would give a better understanding of situations one might encounter in an experimental setup.

A further step would then be the actual experimental realization, though given the particle numbers required for domains wide enough to encompass a localized state this appears elusive with current experimental capabilities.

Furthermore, one could explore the appearance of localized states in other scenarios which are a current research topic of the BEC community, such as the influence of temperature fluctuations in dipolar BECs [162, 161] or molecular BECs [20].

In summary, the thesis has analyzed phase transitions in a variety of contexts. This has resulted in answers regarding the origin of snaking in the PFC model, influence of different types of activity on phase boundaries and has also clarified both the general existence of localized states in BECs and their influence on the classification of phase transitions.

A Appendix

A.1 Spatial Stability and the Prediction of Localized States

The general idea of testing for spatial stability [98] of the uniform ground state is to add a perturbation $\delta\mathbf{u}$ as in Eq. (2.2), though unlike the test for temporal stability (see Sec. 2.1) the perturbation now takes the form

$$\delta\mathbf{u} = \varepsilon e^{\lambda\mathbf{x}}\,, \tag{A.1}$$

where ϵ is once again a smallness parameter. Unlike for temporal stability the spatial eigenvalues λ can be complex. Therefore, in the following λ^* is the complex conjugated spatial eigenvalue.

Applying the perturbation to an equation gives a solution of the form

$$f(\lambda) + \mathcal{O}(\varepsilon) = 0\,.$$

The solution of that equation with respect to λ should give a number of eigenvalues. As often $f(\lambda) = f(-\lambda) = f(\lambda^*) = f(-\lambda^*)$, there should be at least four eigenvalues.

Four combinations of eigenvalues are likely to appear, their perturbations are depicted in Fig. A.1. An eigenvalue with $\mathrm{Re}(\lambda) = 0$ and $\mathrm{Im}(\lambda) \neq 0$ (middle left panel) corresponds to a perturbation in form of a standard pattern. If $\mathrm{Re}(\lambda) \neq 0$ there is a front between a patterned and a flat state, indicating that localized states might be possible (but are not guaranteed). This corresponds to the middle and left panels.

For purely real eigenvalues other than $\lambda = 0$ which just represents a flat state, we get perturbations as depicted in the two right panels, with an exponential front rising from a flat state. The corresponding solutions might look like plateaus, or rather like coexistence of flat states with different mean densities, though this is not proven.

When passing from one set of eigenvalues, and therefore from one solution type to another, multiplicity ensues, which consequently is an indicator for borders of

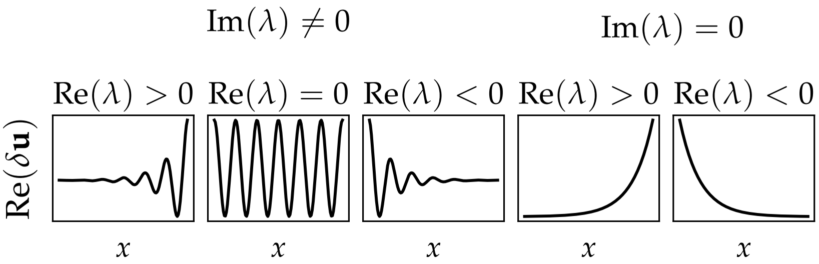
$\mathrm{Im}(\lambda) \neq 0$
$\mathrm{Im}(\lambda) = 0$
$\mathrm{Re}(\lambda) > 0$
$\mathrm{Re}(\lambda) = 0$
$\mathrm{Re}(\lambda) < 0$
$\mathrm{Re}(\lambda) > 0$
$\mathrm{Re}(\lambda) < 0$
$\mathrm{Re}(\delta\mathbf{u})$
x
x
x
x
x

Fig. A.1: Real part of the spatial perturbation $\delta\mathbf{u} = e^{\lambda x}$ for $\mathrm{Im}(\lambda) \neq 0$ with $\mathrm{Re}(\lambda) > 0$ (left), $\mathrm{Re}(\lambda) = 0$ (middle left), $\mathrm{Re}(\lambda) < 0$ (middle), as well as for $\mathrm{Im}(\lambda) = 0$ with $\mathrm{Re}(\lambda) > 0$ (middle right) and $\mathrm{Re}(\lambda) > 0$ (right).

stability. The border of linear stability in particular is given by multiplicity with $\mathrm{Re}(\lambda) = 0$ and $\mathrm{Im}(\lambda) \neq 0$.

The well documented Phase-Field Crystal (PFC) model (see e.g. [182, 83]) will be used to exemplify the stability analysis. Its dynamics are described by

$$\partial_t \rho = \Delta \left[r\rho + (\Delta + 1)^2 \rho + \rho^3 \right] . \tag{A.2}$$

Following the temporal stability analysis leads to

$$\sigma = -k^2 \left[r + (k^2 - 1)^2 + 3\bar{\rho}^2 \right] + \mathcal{O}(\varepsilon) , \tag{A.3}$$

which, using $\sigma = 0$ and $\partial_k \sigma = 0$, gives the following critical values for an infinitely large system:

$$k_c^2 = 0 \quad \text{or} \quad k_c^2 = 1 \pm \sqrt{-r - 3\bar{\rho}^2} \tag{A.4}$$

$$r_c = -3\bar{\rho}^2 . \tag{A.5}$$

This corresponds to the solid black line in Fig. A.2, above which the flat states are stable.

When taking spatial eigenvalues into account the eigenvalues λ take the form

$$\lambda = \pm\sqrt{-1 \pm \sqrt{-r - 3\bar{\rho}^2}} , \tag{A.6}$$

which is also depicted in Fig. A.2. The possibility of localized states is given, branching off in the direction of stable flat states from the border of linear stability, which is indeed indicated through purely linear eigenvalues with multiplicity. Beyond that we find a set of purely imaginary eigenvalues which correspond to a pattern.

A second border with multiplicity appears below the first (dashed black line), which changes the eigenvalue set to two purely real and two purely imaginary eigenvalues, which presumably indicates the appearance of plateau like states.

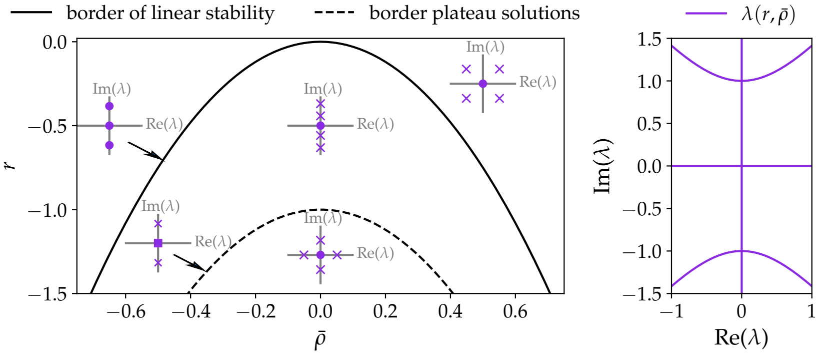

Fig. A.2: Left: Linear stability regions for the PFC model (see Eq. (A.2)) measured through temporal and spatial stability analysis. The solid black line represents the border of linear stability, therefore the flat state is stable above this line and unstable below. The dashed line also has multiplicity, possibly indicating the onset of plateau solutions. Additionally, spatial eigenvalues are indicated through insets to the corresponding regions, which detail the real and imaginary parts. The eigenvalues λ are marked in violet, with crosses representing single eigenvalues while circles and squares represent multiplicity of two and four eigenvalues respectively. Right: The combination of real and imaginary parts of the eigenvalues is limited to the paths traced in violet, depending on all possible combinations of ρ and r.

The right panel in Fig. A.2 also shows the paths the real and imaginary parts of the eigenvalues trace when changing the model parameters $\bar{\rho}$ and r and cements that not every localized state pattern is possible, as wave vector and front width (which depend on the imaginary and real part of λ respectively) are linked through a parabolic dependence.

In the PFC model there are different regions with different types of snaking behavior. Arguments could be made that this behavior is connected to the front width of the localized states.

Assuming the right value of λ a localized state front would be given by the real part of the perturbation $\delta\rho$. Using the Euler equation it takes the form

$$\mathrm{Re}(e^{\lambda x}) = e^{\mathrm{Re}(\lambda)x}\cos(\mathrm{Im}(\lambda)x)\,. \tag{A.7}$$

Rescaling gives two options for measuring the front. $\tilde{x} = x\mathrm{Re}(\lambda)$, leads to

$$e^{\tilde{x}} \cos(\tilde{x}\mathrm{Im}(\lambda)/\mathrm{Re}(\lambda)) \tag{A.8}$$

representing a constant front while b/a gives information about the amount of pattern that fits within that front. Alternatively $\tilde{x} = x\mathrm{Im}(\lambda)$ leads to

$$e^{\tilde{x}\mathrm{Re}(\lambda)/\mathrm{Im}(\lambda)} \cos(\tilde{x}) \tag{A.9}$$

giving a constant pattern with changing front steepness as given by $\mathrm{Re}(\lambda)/\mathrm{Im}(\lambda)$. This is depicted in Fig. A.3 and will be used in the following parts.

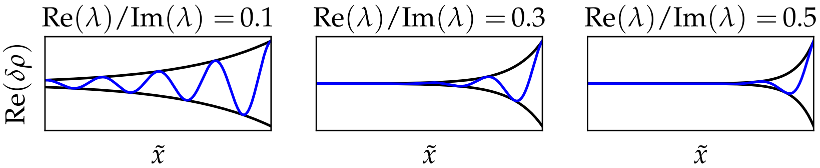

Fig. A.3: Localized state front depending on the ratio of real to imaginary part of the spatial eigenvalue λ, after rescaling so the pattern is constant, while the front varies.

For the PFC model tracking $\mathrm{Re}(\lambda)/\mathrm{Im}(\lambda)$ as a function of the density distance to the border of linear stability $|\rho - \rho_c|$ for different values of r gives the dependence depicted in Fig. A.4. Black lines indicate the onset of localized states (dotted line), wiggling (i.e., snaking without folds, dashed line) and snaking (solid line), neither of which could be guessed at just from looking at the values of $\mathrm{Re}(\lambda)/\mathrm{Im}(\lambda)$.

Considering that localized states are a coexistence of a flat state and a patterned state the value for $\mathrm{Re}(\lambda)/\mathrm{Im}(\lambda)$ which corresponds to that coexisting flat state with the mean density $\bar{\rho}_{cx}$ could be more informative. To test that, $\bar{\rho}_{cx}$ at different r were drawn from Ref. [182] and the corresponding spatial eigenvalues calculated. The results are depicted in the grey line in Fig. A.4. It crosses the snaking onset (solid black line) at a ratio of $\mathrm{Re}(\lambda)/\mathrm{Im}(\lambda) \approx 0.17$ and the wiggling onset (dashed black line) at a ratio of $\mathrm{Re}(\lambda)/\mathrm{Im}(\lambda) \approx 0.1$.

Given that mass conservation is involved, $\bar{\rho}_{cx}$ may not match the mean density of the flat parts of the localized states, due to system size and particle amount constraints. The given values are therefore to be used with caution.

Testing this against the real PFC model at $r = -0.9$ leads to the results depicted in Fig. A.5. The real results show a steeper front than the ones drawn from spatial eigenvalues, therefore exact predictions are likely not possible, though they could be taken as a lower bound.

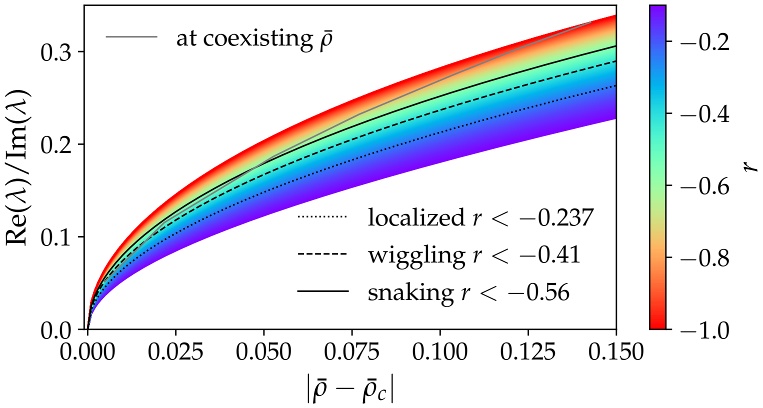

Fig. A.4: Ratio of real to imaginary part of the spatial eigenvalue λ for the PFC model as a function of the density distance to the border of linear stability $|\rho - \rho_c|$ for different values of r, as indicated by the colorbar. The onset of localized states as well as the wiggling and snaking behavior of the localized branch are indicated as dotted, dashed and solid black lines respectively. The grey line gives the results specifically for the flat state which coexists with the pattern to form the localized state.

In the bottom right panel $\mathrm{Re}(\lambda)/\mathrm{Im}(\lambda)$ is once again measured over the mean density distance from the border of linear stability, both for the theoretical values (red) and for the real model (blue). The front steepness is measured through fitting an exponential through the maxima of two neighboring peaks, with λ(1.&2.max) (solid line) corresponding to the fit through the first and second maximum, λ(2.&3.max) (dot-dashed line) and λ(3.&4.max) (dotted line) then match the fit through the second and third, and third and fourth maximum respectively. As expected the fit through the smallest maxima (third and fourth) matches the theoretical curve best, though it still deviates quite far.

Other models which exhibit an onset of snaking have different equations for the spatial eigenvalues and therefore different dependencies for $\mathrm{Re}(\lambda)/\mathrm{Im}(\lambda)$. Such a dependency is depicted in Fig. A.6 for the PFC and the coupled Cahn-Hilliard model (see Ref. [59]) at parameter values which match the onset of snaking of the respective models. The resulting curves have very little in common and show very different values at the density of the uniform coexisting value, both of which are indicators that there is no universality for values of $\mathrm{Re}(\lambda)/\mathrm{Im}(\lambda)$ as an indicator for the onset of snaking.

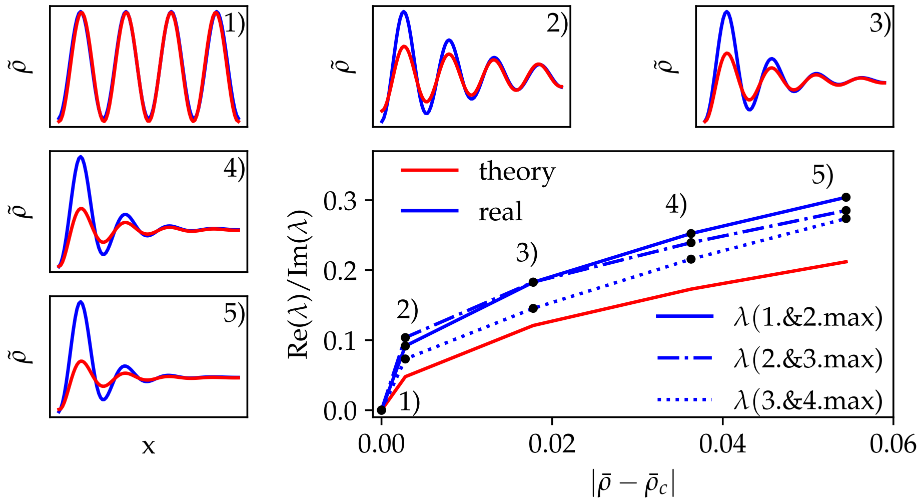

Fig. A.5: Real results (blue) and theoretical prediction (red, rescaled and shifted to match the lowest maximum of the blue curve) for a localized state front in the PFC model at $r = -0.9$, depicted in the numbered windows 1) to 5). The corresponding real to imaginary ratio of the eigenvalues can be found the the lower right figure in red for the theory and blue for the real values, with different line styles, depending on whether the eigenvalue λ was calculated using the first and second maximum (solid), second and third maximum (dot dashed) or third and fourth maximum (dotted).

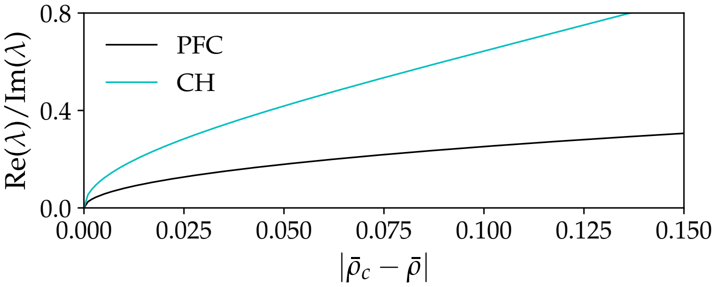

Fig. A.6: Snaking onset as indicated by the ratio of real to imaginary part of the spatial eigenvalue λ for the PFC and coupled Cahn-Hilliard (CH) model (light blue).

A.2 Rescaling of the DDFT Equation with GEM-4 Potential

When rescaling Eq. (3.7), i.e.,

$$\partial_t \rho = \nabla[(1+\rho)\nabla[\log(1+\rho) + \rho_0 \beta (U * \rho)]] \tag{A.10}$$

with the characteristic dimensionless length scale R the new parameters (denoted with subscript s) connect to the original ones as follows:

$$\begin{aligned} x &= Rx_s\,, \\ y &= Ry_s\,, \\ r = \sqrt{x^2+y^2} &= R\sqrt{x_s^2+y_s^2} = Rr_s\,. \end{aligned}$$

In consequence

$$\begin{aligned} \rho(x,y) &= \rho(x_s R, y_s R) = \rho_s(x_s, y_s)\,, \\ \nabla &= R^{-1}\nabla_s\,, \\ U(x,y) &= U(x_s R, y_s R) = U_s(x_s, y_s) \quad \text{with} \quad U_s(r) = \varepsilon e^{-r^4}\,, \\ (U * \rho)(x,y) &= R^d (U_s * \rho_s)(x_s, y_s)\,, \end{aligned}$$

where d is the dimension. The latter is due to

$$\begin{aligned} (U * \rho)(x,y) &= \int \mathrm{d}r'^d U(r - r')\rho(r') \\ &= R^d \int \mathrm{d}r_s'^d U(r_s R - r_s' R)\rho(r_s' R) \\ &= R^d \int \mathrm{d}r_s'^d U_s(r_s - r_s')\rho_s(r_s') \\ &= R^d (U_s * \rho_s)(x_s, y_s)\,. \end{aligned}$$

If furthermore introducing the (dimensionless) energy scale ε by writing $U_s = \varepsilon u_s$ the equation takes the form

$$\partial_t \rho_s = R^{-2}\nabla_s[(1+\rho_s)\nabla_s[\log(1+\rho_s) + R^d \rho_0 \beta \varepsilon (u_s * \rho_s)]\,.$$

Rescaling t using $t = R^2 t_s$ and combining the remaining parameters into $\alpha = R^d \varepsilon \rho_0 \beta$ finally leads to:

$$\partial_{t_s} \rho_s = \nabla_s[(1+\rho_s)\nabla_s[\log(1+\rho_s) + \alpha(u_s * \rho_s)]\,. \tag{A.11}$$

A.3 GEM-4 Results in One Spatial Dimension

The results in one spatial dimension are calculated on a domain of length $L = 3L_c$ with $L_c = 2\pi/k_c$ and $N = 128$ discretization points. The mean density modulation $\bar{\rho}$ is set as the continuation parameter, while α is set to $\alpha = 5.34$, so that the transition between uniform fluid and pattern is at $\bar{\rho} = 0$. This transition is depicted in Fig. A.7 a) and takes the form of a supercritical pitchfork bifurcation.

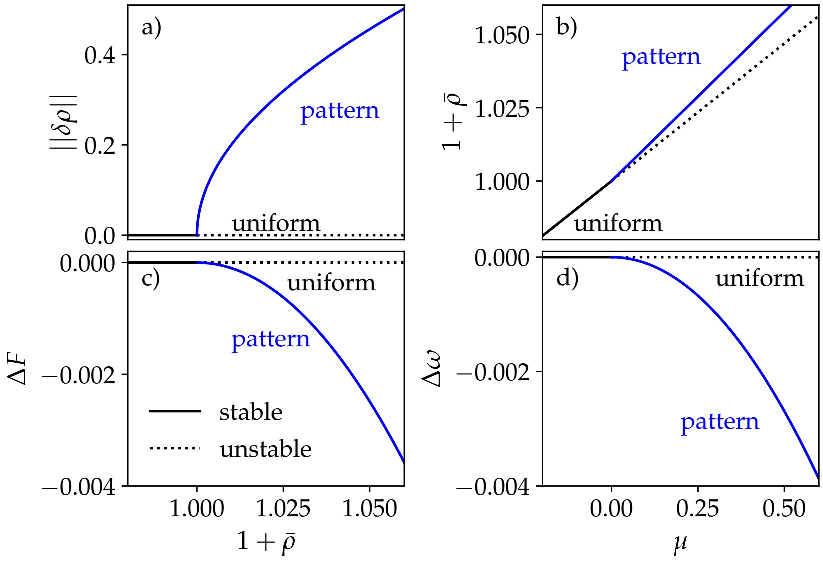

Fig. A.7: Bifurcation diagram of the steady state solutions in 1D of Eq. 3.10 as a function of $1 + \bar{\rho}$ (panels a and c) or μ (panels b and d) at fixed $\alpha = (\alpha(1 + \bar{\rho}))_c$. Stable and unstable states are marked by continuous and dotted lines respectively, while the pattern (or lack thereof) is indicated at the branch. The solution measure is a) the L_2 norm $||\delta\rho||$, b) the mean density $1 + \bar{\rho}$, c) the energy difference to the uniform state $\Delta F = F - F_0$ and d) the grand potential density difference to the uniform state $\Delta\omega$. As the patterned and uniform state branches in the latter do not cross, coexistence is not possible. The domain size is $L = 3L_c$ with $L_c = 2\pi/k_c$ and $N = 128$ discretization points are used.

Fig. A.7 b) depicts the dependence of $1 + \bar{\rho}$ on μ, which easily shows only a near linear dependency between between a system with or without mass conversation ($\bar{\rho}$ or μ as continuation parameter). The former case is discussed in panel a), while the latter requires re-evaluation of stability and saddle-node bifurcations. As the system does not contain those, however, there is no qualitative difference between both considered systems (also see, e.g., Ref. [52] (sections 3.2 and 3.3), Ref. [182] (conclusion) or Ref. [83] (end of section 2) for detailed discussions).

In addition, Fig. A.7 c) depicts the energy difference to the uniform state, showing that the pattern becomes the favorable state once it emerges from the uniform state.

Finally, Fig. A.7 d) shows the grand potential density difference to the uniform state. As the lines only cross or rather touch at the primary bifurcation, there is no indication for localized states.

In addition to the shown bifurcation diagrams the parameter regions around $\alpha = 5.34/5$ and $\alpha = 5.34 \cdot 5$ were tested, confirming that the discussed behavior occurs independent of the choice of α.

A.4 Localized State Interface in the PFC-γ Approximation

To further understand the onset of snaking, changes in the interface between uniform and patterned part of the localized state are tracked for the the PFC-γ approximation while changing s or t and keeping the other parameter at its optimal value of $s = 1/2$ or $t = 1/3$. Specifically, the front in the left primary localized state fold is tracked from its first appearance until the start of full snaking behavior. This is equivalent to following the left most black lines in Fig. 3.8 b) and c).

For ease of viewing, a slice of the density field $\tilde{\rho} = \rho(x = 0.7)$ is prepared by using $\tilde{\rho} \to \frac{\tilde{\rho}-\bar{\tilde{\rho}}}{\max(\tilde{\rho}-\bar{\tilde{\rho}})}$ with $\bar{\tilde{\rho}}$ being the mean of $\tilde{\rho}$. The slice $\tilde{\rho}(y)$ is depicted in Fig. A.8 for the lowest and highest value of s and t respectively. The fronts are depicted for all states in between using the maxima to fit to $f(\tilde{\rho}_{\text{max}}) = e^{-(\tilde{\rho}^2_{\text{max}}/f_1^2)^{f_2}}$, where f_1 is the radius and f_2 represents the steepness of the front. The respective values of s and t can be taken from matching the lines to the colorbar.

It can be seen that the closer the parameters s and t come to the snaking region the steeper the front becomes. However, the increase of steepness slows down until it seems near constant at the snaking onset.

A.5 Stability of Localized States in the Nonlocal BEC

Complex time evolution is used to substantiate the existence and stability of the localized state in a nonlocal Rydberg-dressed toy model of a BEC, i.e., the nonlocal

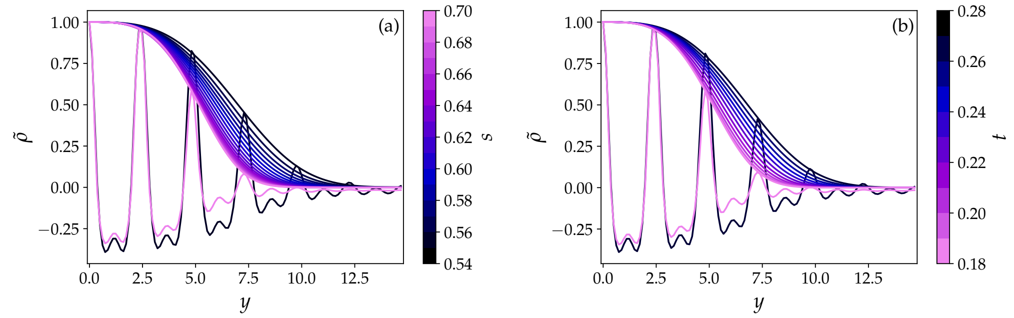

Fig. A.8: Front of the localized states depending on s (a) and t (b) depicted through a rescaled (with respect to the first maximum) density modulation field slice $\tilde{\rho}$ taken at the first fold of the localized states branch (the left black line in Fig. 3.8 b) and c)). The fronts are fitted to the maxima through an equation visualizing the front $f(\tilde{\rho}_{\text{max}}) = e^{-(\tilde{\rho}^2_{\text{max}}/f_1^2)^{f_2}}$. The fronts are depicted for all values of s and t for which there is both a fold and no snaking. The exact values of s and t are indicated by the color. In addition, $\tilde{\rho}$ is depicted for the lowest and highest value of s and t, matching those colors.

GPE (5.29) with the interaction potential from Eq. (5.51). In particular, a two-dimensional domain is considered with $a = 0$ at $\bar{\rho}' = 12.625$ using a uniform state with randomly perturbed phase as initial condition. The domain size is $L_x \times L_y$ with $L_x = 48L_c'/\sqrt{3}$ and $L_y = 2L_c'$. The time step is of size $dt = 10^{-3}$. This results in the localized state displayed in Fig. A.9 (a), which represents the ground state of the system. The relaxation of the amplitude during the complex time evolution is shown in Fig. A.9 (b). Finally, to probe the robustness of the result, this ground state was evolved using real-time evolution, i.e., by employing a dissipative pseudo dynamics. The resulting small numerical fluctuations of the amplitude are illustrated in Fig. A.9 (c) clarifying that the pattern is preserved.

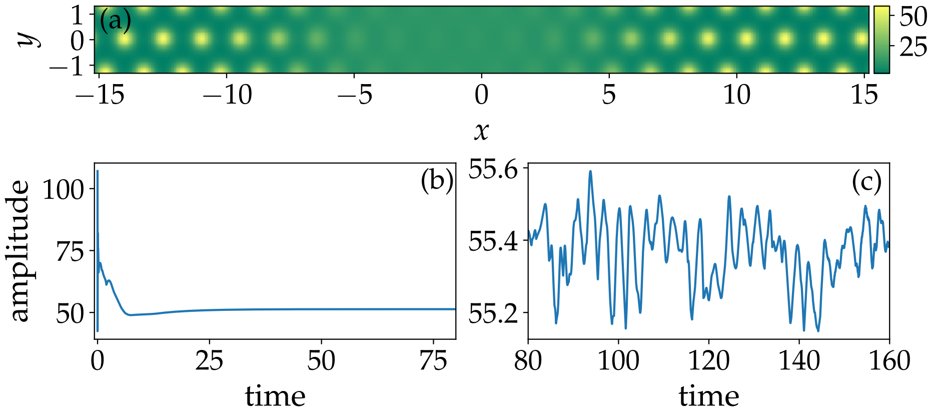

Fig. A.9: (a) Localized ground state for a two-dimensional domain as obtained by complex time evolution of Eq. (5.29), i.e., the nonlocal GPE with the interaction potential from Eq. (5.51). (b) Relaxation of the amplitude during the complex time evolution. (c) Real-time evolution of the amplitude of previously relaxed state, indicating its robustness. The parameters are $a = 0$ and $\bar{\rho}' = 12.625$ with a time step of $dt = 10^{-3}$. The domain size is $L_x \times L_y$ with $L_x = 48L_c'/\sqrt{3}$ and $L_y = 2L_c'$.

Bibliography

[1] G. P. Agrawal. “Chapter 2 - Pulse Propagation in Fibers.” In: *Nonlinear Fiber Optics (Fourth Edition)*. Ed. by G. P. Agrawal. Fourth Edition. Optics and Photonics. San Diego: Academic Press, 2006, pp. 25–50. DOI: `10.1016/B978-012369516-1/50002-9`.

[2] F. Alaimo, S. Praetorius, and A. Voigt. “A microscopic field theoretical approach for active systems.” In: *New J. Phys.* 18 (2016), p. 083008. DOI: `10.1088/1367-2630/18/8/083008`.

[3] J. F. Allen and A. D. Misener. “Flow of Liquid Helium II.” In: *Nature* 141 (1938), pp. 75–75. DOI: `10.1038/141075a0`.

[4] S. Alwyn. *Encyclopedia of Nonlinear Science*. Routledge, Taylor & Francis Group, 2005. ISBN: 978-1-57958-385-9.

[5] F. Ancilotto, M. Rossi, and F. Toigo. “Supersolid structure and excitation spectrum of soft-core bosons in three dimensions.” In: *Phys. Rev. A* 88 (2013), p. 033618. DOI: `10.1103/PhysRevA.88.033618`.

[6] M. H. Anderson et al. “Observation of Bose-Einstein Condensation in a Dilute Atomic Vapor.” In: *Science* 269 (1995), pp. 198–201. DOI: `10.1126/science.269.5221.198`.

[7] A. F Andreev and I. M. Lifshitz. “Quantum theory of defects in crystals.” In: *Sov. Phys. JETP* 29 (1969), pp. 1107–1113.

[8] A. Archer and A. Malijevsky. “Crystallization of soft matter under confinement at interfaces and in wedges.” In: *J. Phys.: Condens. Matter* 28 (2016), p. 244017. DOI: `10.1088/0953-8984/28/24/244017`.

[9] A. J. Archer and R. Evans. “Dynamical density functional theory and its application to spinodal decomposition.” In: *J. Chem. Phys.* 121 (2004), pp. 4246–4254. DOI: `10.1063/1.1778374`.

[10] A. J. Archer and M. Rauscher. “Dynamical density functional theory for interacting Brownian particles: stochastic or deterministic?” In: *J. Phys. A* 37 (2004), p. 9325. DOI: `10.1088/0305-4470/37/40/001`.

[11] A. J. Archer et al. “Deriving phase field crystal theory from dynamical density functional theory: Consequences of the approximations.” In: *Phys. Rev. E* 100 (2019), p. 022140. DOI: `10.1103/PhysRevE.100.022140`.

[12] P. Attard. *Non-equilibrium Thermodynamics and Statistical Mechanics: Foundations and Applications.* Oxford University Press, 2012. ISBN: 978-0-19-966276-0. DOI: `10.1093/acprof:oso/9780199662760.001.0001`.

[13] W. Bao, Y. Cai, and H. Wang. "Efficient numerical methods for computing ground states and dynamics of dipolar Bose–Einstein condensates." In: *J. Comput. Phys.* 229 (2010), pp. 7874–7892. DOI: `10.1016/j.jcp.2010.07.001`.

[14] D. Bauer et al. *Computational Strong-Field Quantum Dynamics.* Berlin: De Gruyter, 2017. ISBN: 3-11-041934-3.

[15] C. Bechinger et al. "Active particles in complex and crowded environments." In: *Rev. Mod. Phys.* 88 (2016), p. 045006. DOI: `10.1103/RevModPhys.88.045006`.

[16] M. Bestehorn. *Hydrodynamik und Strukturbildung.* Springer-Lehrbuch. Berlin, Heidelberg: Springer-Verlag Berlin Heidelberg, 2006. ISBN: 978-3-540-33797-3.

[17] G. Biagioni et al. "Measurement of the superfluid fraction of a supersolid by Josephson effect." In: *Nature* 629 (2024), pp. 773–777. DOI: `10.1038/s41586-024-07361-9`.

[18] J. Bickmann and R. Wittkowski. "Collective dynamics of active Brownian particles in three spatial dimensions: A predictive field theory." In: *Phys. Rev. Res.* 2 (2020), p. 033241. DOI: `10.1103/PhysRevResearch.2.033241`.

[19] J. Bickmann and R. Wittkowski. "Predictive local field theory for interacting active Brownian spheres in two spatial dimensions." In: *J. Phys.: Condens. Matter* 32 (2020), p. 214001. DOI: `10.1088/1361-648x/ab5e0e`.

[20] N. Bigagli et al. "Observation of Bose–Einstein condensation of dipolar molecules." In: *Nature* (2024). DOI: `10.1038/s41586-024-07492-z`.

[21] R. N. Bisset et al. "Ground-state phase diagram of a dipolar condensate with quantum fluctuations." In: *Phys. Rev. A* 94 (2016), p. 033619. DOI: `10.1103/PhysRevA.94.033619`.

[22] P. B. Blakie, D. Baillie, and S. Pal. "Variational theory for the ground state and collective excitations of an elongated dipolar condensate." In: *Commun. Theor. Phys.* 72 (2020), p. 085501. DOI: `10.1088/1572-9494/ab95fa`.

[23] P. B. Blakie et al. "Supersolidity in an elongated dipolar condensate." In: *Phys. Rev. Res.* 2 (2020). DOI: `10.1103/PhysRevResearch.2.043318`.

[24] N. Bogoliubov. "On the theory of superfluidity." In: *J. Phys. USSR* 11 (1947).

[25] S. N. Bose. "Plancks Gesetz und Lichtquantenhypothese." In: *Z. Phys.* 26 (1924), pp. 178–181. DOI: `10.1007/BF01327326`.

[26] F. Böttcher et al. "Transient Supersolid Properties in an Array of Dipolar Quantum Droplets." In: *Phys. Rev. X* 9 (2019), p. 011051. DOI: `10.1103/PhysRevX.9.011051`.

[27] J. P. Boyd. *Chebyshev and Fourier spectral methods.* 2. ed. (rev.) Mineola, NY: Dover Publ., 2001. ISBN: 0-486-41183-4.

[28] A. J. Bray. "Theory of phase-ordering kinetics." In: *Adv. Phys.* 43 (1994), pp. 357–459. DOI: `10.1080/00018739400101505`.

[29] J. Burke and E. Knobloch. "Localized states in the generalized Swift-Hohenberg equation." In: *Phys. Rev. E* 73 (2006), p. 056211. DOI: `10.1103/PhysRevE.73.056211`.

[30] I. Buttinoni et al. "Dynamical clustering and phase separation in suspensions of self-propelled colloidal particles." In: *Phys. Rev. Lett.* 110 (2013), p. 238301. DOI: `10.1103/PhysRevLett.110.238301`.

[31] H. B. Callen. *Thermodynamics. an introduction to the physical theories of equilibrium thermostatics and irreversible thermodynamics.* New York, London: John Wiley & Sons, Inc, 1960. ISBN: 978-0-471-13035-2.

[32] J. E. Campbell. "On a Law of Combination of Operators (Second Paper)*." In: *Proc. London Math. Soc.* s1-29 (1897), pp. 14–32. DOI: `10.1112/plms/s1-29.1.14`.

[33] L. Caprini, U. M. B. Marconi, and A. Puglisi. "Spontaneous Velocity Alignment in Motility-Induced Phase Separation." In: *Phys. Rev. Lett.* 124 (2020), p. 078001. DOI: `10.1103/PhysRevLett.124.078001`.

[34] Y. Castin. "Bose-Einstein Condensates in Atomic Gases: Simple Theoretical Results." In: *Coherent atomic matter waves.* Ed. by R. Kaiser, C. Westbrook, and F. David. Berlin, Heidelberg: Springer Berlin Heidelberg, 2001, pp. 1–136. ISBN: 978-3-540-45338-3.

[35] M. E. Cates and J. Tailleur. "Motility-induced phase separation." In: *Annu. Rev. Condens. Matter Phys.* 6 (2015), pp. 219–244. DOI: `10.1146/annurev-conmatphys-031214-014710`.

[36] A. I. Chervanyov, H. Gomez, and U. Thiele. "Effect of the orientational relaxation on the collective motion of patterns formed by self-propelled particles." In: *Europhys. Lett.* 115 (2016), p. 68001. DOI: `10.1209/0295-5075/115/68001`.

[37] G. V. Chester. "Speculations on Bose-Einstein Condensation and Quantum Crystals." In: *Phys. Rev. A* 2 (1970), pp. 256–258. DOI: `10.1103/PhysRevA.2.256`.

[38] L. Chomaz. “Probing the supersolid order via high-energy scattering: Analytical relations among the response, density modulation, and superfluid fraction.” In: *Phys. Rev. A* 102 (2020), p. 023333. DOI: `10.1103/PhysRevA.102.023333`.

[39] L. Chomaz et al. “Long-Lived and Transient Supersolid Behaviors in Dipolar Quantum Gases.” In: *Phys. Rev. X* 9 (2019), p. 021012. DOI: `10.1103/PhysRevX.9.021012`.

[40] F. Cinti, M. Boninsegni, and T. Pohl. “Exchange-induced crystallization of soft-core bosons.” In: *New J. Phys.* 16 (2014), p. 033038. DOI: `10.1088/1367-2630/16/3/033038`.

[41] F. Cinti et al. “Supersolid Droplet Crystal in a Dipole-Blockaded Gas.” In: *Phys. Rev. Lett.* 105 (2010), p. 135301. DOI: `10.1103/PhysRevLett.105.135301`.

[42] Ariz. Coconino National Forest. *Strawberry Crater Trail.* Cropped from original. This work is part of the public domain. 2017. URL: `https://www.flickr.com/photos/coconinonationalforest/25021222158/`.

[43] E. Crosato, M. Prokopenko, and R. E. Spinney. “Irreversibility and emergent structure in active matter.” In: *Phys. Rev. E* 100 (2019), p. 042613. DOI: `10.1103/PhysRevE.100.042613`.

[44] K. B. Davis et al. “Bose-Einstein Condensation in a Gas of Sodium Atoms.” In: *Phys. Rev. Lett.* 75 (1995), pp. 3969–3973. DOI: `10.1103/PhysRevLett.75.3969`.

[45] M. Doi. “Onsager’s Variational Principle in Soft Matter Dynamics.” In: *Non-equilibrium soft matter physics.* Ed. by S. Komura and T. Ohta. Series in soft condensed matter, v. 4. Singapore: World Scientific Pub. Co., 2012. ISBN: 1-280-66957-8.

[46] M. Doi. “What is soft matter?” In: *Soft Matter Physics.* Oxford University Press, 2013. ISBN: 978-0-19-965295-2. DOI: `10.1093/acprof:oso/9780199652952.003.0001`.

[47] E. A. Donley et al. “Dynamics of collapsing and exploding Bose-Einstein condensates.” In: *Nature* 412 (2001), pp. 295–299. DOI: `10.1038/35085500`.

[48] A. Einstein. “Quantentheorie des einatomigen idealen Gases. Zweite Abhandlung.” In: *Albert Einstein: Akademie-Vorträge.* John Wiley & Sons, Ltd, 2005, pp. 245–257. ISBN: 978-3-527-60895-9. DOI: `10.1002/3527608958.ch28`.

[49] K. R. Elder et al. “Modeling Elasticity in Crystal Growth.” In: *Phys. Rev. Lett.* 88 (2002), p. 245701. DOI: `10.1103/PhysRevLett.88.245701`.

[50] K. R. Elder et al. “Phase-field crystal modeling and classical density functional theory of freezing.” In: *Phys. Rev. B* 75 (2007), p. 064107. DOI: `10.1103/PhysRevB.75.064107`.

[51] H. Emmerich et al. “Phase-field-crystal models for condensed matter dynamics on atomic length and diffusive time scales: an overview.” In: *Adv. Phys.* 61 (2012), pp. 665–743. DOI: `10.1080/00018732.2012.737555`.

[52] S. Engelnkemper et al. “Continuation for thin film hydrodynamics and related scalar problems.” In: *Computational Modeling of Bifurcations and Instabilities in Fluid Mechanics*. Ed. by A. Gelfgat. Computational Methods in Applied Sciences, vol 50. Cham: Springer, 2019, pp. 459–501. DOI: `10.1007/978-3-319-91494-7_13`.

[53] F. D. C. Farrell et al. “Pattern formation in self-propelled particles with density-dependent motility.” In: *Phys. Rev. Lett.* 108 (2012), p. 248101. DOI: `10.1103/PhysRevLett.108.248101`.

[54] P. O. Fedichev, M. W. Reynolds, and G. V. Shlyapnikov. “Three-Body Recombination of Ultracold Atoms to a Weakly Bound *s* Level.” In: *Phys. Rev. Lett.* 77 (1996), pp. 2921–2924. DOI: `10.1103/PhysRevLett.77.2921`.

[55] E. Ferrante et al. “Elasticity-Based Mechanism for the Collective Motion of Self-Propelled Particles with Springlike Interactions: A Model System for Natural and Artificial Swarms.” In: *Phys. Rev. Lett.* 111 (2013), p. 268302. DOI: `10.1103/PhysRevLett.111.268302`.

[56] I. Ferrier-Barbut et al. “Observation of Quantum Droplets in a Strongly Dipolar Bose Gas.” In: *Phys. Rev. Lett.* 116 (2016), p. 215301. DOI: `10.1103/PhysRevLett.116.215301`.

[57] A. Fick. “Ueber Diffusion.” In: *Ann. Phys. (Berl.)* 170 (1855), pp. 59–86. DOI: `https://doi.org/10.1002/andp.18551700105`.

[58] J. A. Fleck, J. R. Morris, and M. D. Feit. “Time-dependent propagation of high energy laser beams through the atmosphere.” In: *Appl. Phys.* 10 (1976), pp. 129–160. DOI: `10.1007/BF00896333`.

[59] T. Frohoff-Hülsmann and U. Thiele. “Localized states in coupled Cahn–Hilliard equations.” In: *IMA J. Appl. Math.* (2020).

[60] T. Frohoff-Hülsmann, U. Thiele, and L. M. Pismen. “Non-reciprocity induces resonances in a two-field Cahn–Hilliard model.” In: *Philos. Trans. Royal Soc. A* 381 (2023), p. 20220087. DOI: `10.1098/rsta.2022.0087`.

[61] F. Ginot et al. “Aggregation-fragmentation and individual dynamics of active clusters.” In: *Nat. Commun.* 9 (2018), p. 696. DOI: `10.1038/s41467-017-02625-7`.

[62] P. Goldbart, N. Goldenfeld, and D. Sherrington. *Stealing the Gold: A celebration of the pioneering physics of Sam Edwards.* Oxford University Press, 2004. ISBN: 978-0-19-852853-1. DOI: `10.1093/acprof:oso/9780198528531.001.0001`.

[63] G. Gompper et al. "The 2020 motile active matter roadmap." In: *J Phys: Condens Matter* 32 (2020). DOI: `10.1088/1361-648X/ab6348`.

[64] G. Gompper et al. "The 2020 motile active matter roadmap." In: *J. Phys.: Condens. Matter* 32 (2020), p. 193001. DOI: `10.1088/1361-648x/ab6348`.

[65] H. Göring, H.-G. Roos, and L. Tobiska. *Finite-Element-Methode. Eine Einführung.* Berlin, Boston: De Gruyter, 1985. ISBN: 978-3-11-264440-9. DOI: `10.1515/9783112644409`.

[66] A. Griffin. "Conserving and gapless approximations for an inhomogeneous Bose gas at finite temperatures." In: *Phys. Rev. B* 53 (1996), pp. 9341–9347. DOI: `10.1103/PhysRevB.53.9341`.

[67] E. P. Gross. "Structure of a quantized vortex in boson systems." In: *Nuovo Cim.* 20 (1961), pp. 454–477.

[68] E. P. Gross. "Unified Theory of Interacting Bosons." In: *Phys. Rev.* 106 (1957), pp. 161–162. DOI: `10.1103/PhysRev.106.161`.

[69] M. Gwyther-Jones. *Cheetah.* Cropped from original. This work is licensed under the Creative Commons Attribution 2.0 International License. To view a copy of this license, visit `https://creativecommons.org/licenses/by/2.0/`. 2013. URL: `https://www.flickr.com/photos/12587661@N06/8455886239`.

[70] H. Haken. *Synergetics: introduction and advanced topics.* Springer Series in Synergetics. Springer, 2012. ISBN: 3-642-96469-9.

[71] R. J. Hawkins and T. B. Liverpool. "Stress Reorganization and Response in Active Solids." In: *Phys. Rev. Lett.* 113 (2014), p. 028102. DOI: `10.1103/PhysRevLett.113.028102`.

[72] L.-J. He, F. Maucher, and Y.-C. Zhang. *On the infrared cutoff for dipolar droplets.* 2024. arXiv: `2406.19609`.

[73] V. Heinonen, K. J. Burns, and J. Dunkel. "Quantum hydrodynamics for supersolid crystals and quasicrystals." In: *Phys. Rev. A* 99 (2019), p. 063621. DOI: `10.1103/PhysRevA.99.063621`.

[74] D. Helbing. "Pattern formation, social forces, and diffusion instability in games with success-driven motion." In: *The European Physical Journal B* 67 (2009), pp. 345–356. DOI: `10.1140/epjb/e2009-00025-7`.

[75] N. Henkel. *Rydberg-dressed Bose-Einstein condensates.* Dissertation. Dresden, 2013.

[76] N. Henkel, R. Nath, and T. Pohl. "Three-Dimensional Roton Excitations and Supersolid Formation in Rydberg-Excited Bose-Einstein Condensates." In: *Phys. Rev. Lett.* 104 (2010), p. 195302. DOI: `10.1103/PhysRevLett.104.195302`.

[77] C. Hernández-López et al. "Model of Active Solids: Rigid Body Motion and Shape-Changing Mechanisms." In: *Phys. Rev. Lett.* 132 (2024), p. 238303. DOI: `10.1103/PhysRevLett.132.238303`.

[78] J. Hertkorn. *Self-organized Structures and Excitations in Dipolar Quantum Fluids.* Dissertation. Stuttgart, 2024.

[79] J. Hertkorn et al. "Pattern formation in quantum ferrofluids: From supersolids to superglasses." In: *Phys. Rev. Research* 3 (2021), p. 033125. DOI: `10.1103/PhysRevResearch.3.033125`.

[80] M. P. Holl. *Analysis of passive and active phase-field-crystal models for colloidal mixtures.* Dissertation. Münster, 2022.

[81] M. P. Holl, A. J. Archer, and U. Thiele. "Efficient calculation of phase coexistence and phase diagrams: Application to a binary phase-field crystal model." In: *J. Phys.: Condens. Matter* 33 (2021), p. 115401. DOI: `10.1088/1361-648X/abce6e`.

[82] M. P. Holl, A. B. Steinberg, and U. Thiele. *Motility-induced crystallization and rotating crystallites.* 2024. arXiv: `2408.06114`.

[83] M. P. Holl et al. "Localized states in passive and active phase-field-crystal models." In: *IMA J. Appl. Math.* 86 (2021), pp. 896–923. DOI: `10.1093/imamat/hxab025`.

[84] J. Houghton. *The physics of atmospheres.* 3. ed. Cambridge Univ. Press, 2002. ISBN: 0-521-01122-1.

[85] R. Hoyle. *Pattern Formation: An Introduction to Methods.* Cambridge Univ. Press, 2007. ISBN: 978-0-521-81750-9.

[86] Z.-F. Huang, K. R. Elder, and N. Provatas. "Phase-field-crystal dynamics for binary systems: Derivation from dynamical density functional theory, amplitude equation formalism, and applications to alloy heterostructures." In: *Phys. Rev. E* 82 (2010), p. 021605. DOI: `10.1103/PhysRevE.82.021605`.

[87] P. Hunter. "Of Turing and zebras: Turing diffusion inspires applications in nature and beyond." In: *EMBO Rep.* 24 (2023). DOI: `10.15252/embr.202357405`.

[88] A. Hutt and H. Haken. *Synergetics.* 1st ed. 2020. Encyclopedia of Complexity and Systems Science Series. New York, NY: Springer US, 2020. ISBN: 978-1-0716-0421-2.

[89] S. Inouye et al. “Observation of Feshbach resonances in a Bose-Einstein condensate.” In: *Nature* 392 (1998), pp. 151–154. DOI: `10.1038/32354`.

[90] H. Kadau et al. “Observing the Rosensweig instability of a quantum ferrofluid.” In: *Nature* 530 (2016), pp. 194–197. DOI: `10.1038/nature16485`.

[91] P. Kapitza. “Viscosity of Liquid Helium below the λ-Point.” In: *Nature* 141 (1938), pp. 74–74. DOI: `10.1038/141074a0`.

[92] S. Karthika, T. K. Radhakrishnan, and P. Kalaichelvi. “A Review of Classical and Nonclassical Nucleation Theories.” In: *Cryst. Growth Des.* 16 (2016), pp. 6663–6681. DOI: `10.1021/acs.cgd.6b00794`.

[93] E. F. Keller. “Active matter, then and now.” In: *Hist. Philos. Life Sci.* 38 (2016), p. 11. DOI: `10.1007/s40656-016-0112-3`.

[94] W. Ketterle. “Nobel lecture: When atoms behave as waves: Bose-Einstein condensation and the atom laser.” In: *Rev. Mod. Phys.* 74 (2002), pp. 1131–1151. DOI: `10.1103/RevModPhys.74.1131`.

[95] I. M. Khalatnikov. *An introduction to the theory of superfluidity.* Frontiers in physics [23]. New York, Amsterdam: W. A. Benjamin, inc., 1965.

[96] D. Y. Kim and M. H. W. Chan. “Absence of Supersolidity in Solid Helium in Porous Vycor Glass.” In: *Phys. Rev. Lett.* 109 (2012), p. 155301. DOI: `10.1103/PhysRevLett.109.155301`.

[97] E. Knobloch. “Localized structures and front propagation in systems with a conservation law.” In: *IMA J. Appl. Math.* 81 (2016), pp. 457–487. DOI: `10.1093/imamat/hxw029`.

[98] E. Knobloch. “Spatial Localization in Dissipative Systems.” In: *Annu. Rev. Condens. Matter Phys.* 6 (2015), pp. 325–359. DOI: `10.1146/annurev-conmatphys-031214-014514`.

[99] S. Komura and T. Ohta. *Non-equilibrium soft matter physics.* 1st ed. Vol. 4. Series in soft condensed matter. Singapore: World Scientific Publishing Co. Pte. Ltd, 2012. ISBN: 978-981-4360-62-3.

[100] C. T. Lane. *Superfluid Physics.* Intern. Series in pure and applied Physics. New York [u.a: McGraw-Hill, 1962.

[101] T. D. Lee, K. Huang, and C. N. Yang. “Eigenvalues and Eigenfunctions of a Bose System of Hard Spheres and Its Low-Temperature Properties.” In: *Phys. Rev.* 106 (1957), pp. 1135–1145. DOI: `10.1103/PhysRev.106.1135`.

[102] R. Lefever et al. “Deeply gapped vegetation patterns: On crown/root allometry, criticality and desertification.” In: *J. Theor. Biol.* 261 (2009), pp. 194–209. DOI: `10.1016/j.jtbi.2009.07.030`.

[103] A. J. Leggett. “Can a Solid Be ”Superfluid”?” In: *Phys. Rev. Lett.* 25 (1970), pp. 1543–1546. DOI: `10.1103/PhysRevLett.25.1543`.

[104] A. J. Leggett. “On the superfluid fraction of an arbitrary many-body system at T = 0.” In: *J. Stat. Phys.* 93 (1998), pp. 927–941. DOI: `10.1023/b:joss.0000033170.38619.6c`.

[105] J. Léonard et al. “Supersolid formation in a quantum gas breaking a continuous translational symmetry.” In: *Nature* 543 (2017), pp. 87–90. DOI: `10.1038/nature21067`.

[106] J.-R. Li et al. “A stripe phase with supersolid properties in spin–orbit-coupled Bose-Einstein condensates.” In: *Nature* 543 (2017), pp. 91–94. DOI: `10.1038/nature21431`.

[107] C. N. Likos et al. “Criterion for determining clustering versus reentrant melting behavior for bounded interaction potentials.” In: *Phys. Rev. E* 63 (2001), p. 031206. DOI: `10.1103/PhysRevE.63.031206`.

[108] A. R. P. Lima and A. Pelster. “Beyond mean-field low-lying excitations of dipolar Bose gases.” In: *Phys. Rev. A* 86 (2012), p. 063609. DOI: `10.1103/PhysRevA.86.063609`.

[109] A. R. P. Lima and A. Pelster. “Quantum fluctuations in dipolar Bose gases.” In: *Phys. Rev. A* 84 (2011), p. 041604. DOI: `10.1103/PhysRevA.84.041604`.

[110] D. J. B. Lloyd et al. “Homoclinic snaking near the surface instability of a polarisable fluid.” In: *J. Fluid Mech.* 783 (2015). Picture by Achim Beetz. Cropped from original. This work is licensed under the Creative Commons Attribution 4.0 International License. To view a copy of this license, visit `https://creativecommons.org/licenses/by/4.0/.`, pp. 283–305. DOI: `10.1017/jfm.2015.565`.

[111] F. London. “On the Bose-Einstein Condensation.” In: *Phys. Rev.* 54 (1938), pp. 947–954. DOI: `10.1103/PhysRev.54.947`.

[112] M. D. Lukin et al. “Dipole Blockade and Quantum Information Processing in Mesoscopic Atomic Ensembles.” In: *Phys. Rev. Lett.* 87 (2001), p. 037901. DOI: `10.1103/PhysRevLett.87.037901`.

[113] T. Ma and S. Wang. *Phase Transition Dynamics.* eng. 2nd ed. 2019. Cham: Springer International Publishing, 2019. ISBN: 978-3-030-29260-7.

[114] T. Macrı̀, S. Saccani, and F. Cinti. “Ground State and Excitation Properties of Soft-Core Bosons.” In: *J. Low Temp. Phys.* 177 (2014), p. 59.

[115] T. Macrì et al. “Elementary excitations of ultracold soft-core bosons across the superfluid-supersolid phase transition.” In: *Phys. Rev. A* 87 (2013), p. 061602.

[116] E. Madelung. “Quantentheorie in hydrodynamischer Form.” In: *Z. Physik* 40 (1927), pp. 322–326. DOI: `10.1007/bf01400372`.

[117] A. Maitra and S. Ramaswamy. “Oriented Active Solids.” In: *Phys. Rev. Lett.* 123 (2019), p. 238001. DOI: `10.1103/physrevlett.123.238001`.

[118] M. C. Marchetti et al. “Hydrodynamics of soft active matter.” In: *Rev. Mod. Phys.* 85 (2013), pp. 1143–1189. DOI: `10.1103/RevModPhys.85.1143`.

[119] U. M. B. Marconi and P. Tarazona. “Dynamic density functional theory of fluids.” In: *J. Chem. Phys.* 110 (1999), pp. 8032–8044. DOI: `10.1063/1.478705`.

[120] U. M. B. Marconi and P. Tarazona. “Dynamic density functional theory of fluids.” In: *J. Phys. Condens. Matter* 12 (2000), A413. DOI: `10.1088/0953-8984/12/8A/356`.

[121] D. Marenduzzo. “An introduction to the statistical physics of active matter: Motility-induced phase separation and the “generic instability” of active gels.” In: *Eur. Phys. J.-Spec. Top.* 225 (2016), pp. 2065–2077. DOI: `10.1140/epjst/e2016-60084-6`.

[122] F. Maucher, S. Skupin, and W. Krolikowski. “Collapse in the nonlocal nonlinear Schrödinger equation.” In: *Nonlinearity* 24 (2011), pp. 1987–2001. DOI: `10.1088/0951-7715/24/7/005`.

[123] F. Maucher et al. “Rydberg-Induced Solitons: Three-Dimensional Self-Trapping of Matter Waves.” In: *Phys. Rev. Lett.* 106 (2011), p. 170401.

[124] A. M. Menzel and H. Löwen. “Traveling and Resting Crystals in Active Systems.” In: *Phys. Rev. Lett.* 110 (2013), p. 055702. DOI: `10.1103/PhysRevLett.110.055702`.

[125] A. M. Menzel, T. Ohta, and H. Löwen. “Active crystals and their stability.” In: *Phys. Rev. E* 89 (2014), p. 022301. DOI: `10.1103/PhysRevE.89.022301`.

[126] H. J. Metcalf and P. van der Straten. *Laser cooling and trapping.* Graduate texts in contemporary physics. Springer, 1999. ISBN: 0-387-98728-2. DOI: `10.1007/978-1-4612-1470-0`.

[127] S. Miller. *Image: School of Fish.* Cropped from original. This work is licensed under the Creative Commons Attribution 2.0 International License. To view a copy of this license, visit `https://creativecommons.org/licenses/by/2.0/`. 2013. URL: `https://www.flickr.com/photos/12508217@N08/10118765555`.

[128] B. M. Mognetti et al. “Living clusters and crystals from low-density suspensions of active colloids.” In: *Phys. Rev. Lett.* 111 (2013), p. 245702. DOI: `10.1103/PhysRevLett.111.245702`.

[129] NASA. *Image: NASA’s Best-Observed X-Class Flare of All Time*. Cropped from original. This work is part of the public domain. 2017. URL: `https://images.nasa.gov/details/GSFC_20171208_Archive_e001135`.

[130] P. Natarajan. *The shapes of galaxies and their dark halos*. River Edge, N. J.: World Scientific, 2002.

[131] G. Nicolis. *Introduction to nonlinear science*. eng. Cambridge: Cambridge University Press, 1995. ISBN: 978-1-139-17080-2.

[132] H. Nishimori and G. Ortiz. *Elements of phase transitions and critical phenomena*. Oxford graduate texts. Oxford: Oxford University Press, 2011. ISBN: 0-19-172294-4.

[133] L. Ophaus, S. V. Gurevich, and U. Thiele. “Resting and traveling localized states in an active phase-field-crystal model.” In: *Phys. Rev. E* 98 (2018), p. 022608. DOI: `10.1103/PhysRevE.98.022608`.

[134] L. Ophaus et al. “Phase-field-crystal description of active crystallites: Elastic and inelastic collisions.” In: *Chaos* 30 (2020), p. 123149. DOI: `10.1063/5.0019426`.

[135] L. Ophaus et al. “Two-dimensional localized states in an active phase-field-crystal model.” In: *Phys. Rev. E* 103 (2021), p. 032601. DOI: `10.1103/PhysRevE.103.032601`.

[136] D. W. Oxtoby. “Nucleation of Crystals From the Melt.” In: *Advances in Chemical Physics*. John Wiley & Sons, Ltd, 1988, pp. 263–296. ISBN: 978-0-470-12269-3. DOI: `10.1002/9780470122693.ch7`.

[137] D. W. Oxtoby and R. Evans. “Nonclassical nucleation theory for the gas–liquid transition.” In: *The Journal of Chemical Physics* 89 (1988), pp. 7521–7530. DOI: `10.1063/1.455285`.

[138] J. Palacci et al. “Living Crystals of Light-Activated Colloidal Surfers.” In: *Science* 339 (2013), pp. 936–940. DOI: `10.1126/science.1230020`.

[139] B. L. Partridge. “The Structure and Function of Fish Schools.” In: *Sci. Am.* 246 (1982), pp. 114–123. DOI: `10.1038/scientificamerican0682-114`.

[140] A. Patch, D. Yllanes, and M. C. Marchetti. “Kinetics of motility-induced phase separation and swim pressure.” In: *Phys. Rev. E* 95 (2017), p. 012601. DOI: `10.1103/PhysRevE.95.012601`.

[141] C. J. Pethick and H. Smith. *Bose-Einstein Condensation in Dilute Gases.* 2nd ed. Cambridge University Press, 2008. DOI: `10.1017/CBO9780511802850`.

[142] A. P. Petroff and A. Libchaber. “Nucleation of rotating crystals by Thiovulum majus bacteria.” In: *New J. Phys.* 20 (2018), p. 015007. DOI: `10.1088/1367-2630/aa9d58`.

[143] A. P. Petroff, X.-L. Wu, and A. Libchaber. “Fast-Moving Bacteria Self-Organize into Active Two-Dimensional Crystals of Rotating Cells.” In: *Phys. Rev. Lett.* 114 (2015), p. 158102. DOI: `10.1103/PhysRevLett.114.158102`.

[144] D. S. Petrov. “Quantum Mechanical Stabilization of a Collapsing Bose-Bose Mixture.” In: *Phys. Rev. Lett.* 115 (2015), p. 155302. DOI: `10.1103/PhysRevLett.115.155302`.

[145] L. Pismen. *Active Matter Within and Around Us.* The Frontiers Collection. Cham: Springer Nature Switzerland AG, 2021. ISBN: 978-3-030-68420-4.

[146] L. P. Pitaevskii. “Vortex lines in an imperfect Bose gas.” In: *Sov. Phys. JETP* 13 (1961), p. 451.

[147] L. P. Pitaevskii and S. Stringari. *Bose-Einstein Condensation and Superfluidity.* Oxford University Press, 2016. ISBN: 978-0-19-875888-4. DOI: `10.1093/acprof:oso/9780198758884.001.0001`.

[148] G. Plonka et al. *Numerical Fourier Analysis.* Second edition. Applied and Numerical Harmonic Analysis. Cham: Springer International Publishing AG, 2023. ISBN: 978-3-031-35004-7.

[149] S. Praetorius et al. “Active crystals on a sphere.” In: *Phys. Rev. E* 97 (2018), p. 052615. DOI: `10.1103/PhysRevE.97.052615`.

[150] S. Prestipino. “Cluster phases of penetrable rods on a line.” In: *Phys. Rev. E* 90 (2014). DOI: `10.1103/PhysRevE.90.042306`.

[151] S. Prestipino and F. Saija. “Hexatic phase and cluster crystals of two-dimensional GEM4 spheres.” In: *J Chem Phys* 141 (2014), p. 184502. DOI: `10.1063/1.4901302`.

[152] S. Ramaswamy. “The mechanics and statistics of active matter.” In: *Annu. Rev. Condens. Matter Phys.* 1 (2010), pp. 323–345. DOI: `10.1146/annurev-conmatphys-070909-104101`.

[153] S. Ramaswamy and R. A. Simha. “The mechanics of active matter: Broken-symmetry hydrodynamics of motile particles and granular layers.” In: *Solid State Commun.* 139 (2006). Soft Condensed Matter, pp. 617–622. DOI: `10.1016/j.ssc.2006.05.042`.

[154] L. Rapp, F. Bergmann, and W. Zimmermann. "Systematic extension of the Cahn-Hilliard model for motility-induced phase separation." In: *Eur. Phys. J. E* 42 (2019), p. 57. DOI: `10.1140/epje/i2019-11825-8`.

[155] C. W. Reynolds. "Flocks, herds and schools: A distributed behavioral model." In: *Proceedings of the 14th Annual Conference on Computer Graphics and Interactive Techniques.* SIGGRAPH '87. New York, NY, USA: Association for Computing Machinery, 1987, pp. 25–34. ISBN: 0-89791-227-6. DOI: `10.1145/37401.37406`.

[156] P. Romanczuk et al. "Active Brownian particles from individual to collective stochastic dynamics." In: *Eur. Phys. J.-Spec. Top.* 202 (2012), pp. 1–162. DOI: `10.1140/epjst/e2012-01529-y`.

[157] S. Ronen and J. L. Bohn. "Dipolar Bose-Einstein condensates at finite temperature." In: *Phys. Rev. A* 76 (2007), p. 043607. DOI: `10.1103/PhysRevA.76.043607`.

[158] S. Ronen, D. C. E. Bortolotti, and J. L. Bohn. "Bogoliubov modes of a dipolar condensate in a cylindrical trap." In: *Phys Rev A* 74 (2006), p. 013623. DOI: `10.1103/PhysRevA.74.013623`.

[159] S. Saccani, S. Moroni, and M. Boninsegni. "Excitation Spectrum of a Supersolid." In: *Phys. Rev. Lett.* 108 (2012), p. 175301. DOI: `10.1103/PhysRevLett.108.175301`.

[160] H. Saito. "Path-Integral Monte Carlo Study on a Droplet of a Dipolar Bose–Einstein Condensate Stabilized by Quantum Fluctuation." In: *J. Phys. Soc. Jpn.* 85 (2016), p. 053001. DOI: `10.7566/JPSJ.85.053001`.

[161] J. Sánchez-Baena, T. Pohl, and F. Maucher. "Superfluid-supersolid phase transition of elongated dipolar Bose-Einstein condensates at finite temperatures." In: *Phys. Rev. Res.* 6 (2024), p. 023183. DOI: `10.1103/PhysRevResearch.6.023183`.

[162] J. Sánchez-Baena et al. "Heating a dipolar quantum fluid into a solid." In: *Nat. Commun.* 14 (2023), p. 1868. DOI: `10.1038/s41467-023-37207-3`.

[163] A. Sandberg. *Image: Striped Cirrocumulus Undulatus Clouds.* Cropped from original. This work is licensed under the Creative Commons Attribution 2.0 International License. To view a copy of this license, visit `https://creativecommons.org/licenses/by/2.0/`. 2007. URL: `https://www.flickr.com/photos/87547772@N00/1252651164`.

[164] M. Schmitt et al. "Self-bound droplets of a dilute magnetic quantum liquid." In: *Nature* 539 (2016), pp. 259–262.

[165] F. Schwabl. *Quantenmechanik für Fortgeschrittene (QM II).* Berlin, Heidelberg, 2005.

[166] R. Seydel. *Practical bifurcation and stability analysis.* 3. ed. Interdisciplinary applied mathematics 5. New York, NY [u.a: Springer, 2010. ISBN: 978-1-4419-1739-3.

[167] M. R. Shaebani et al. “Computational models for active matter.” In: *Nat. Rev. Phys.* 2 (2020), pp. 181–199. DOI: `10.1038/s42254-020-0152-1`.

[168] J. C. Smith, D. Baillie, and P. B. Blakie. “Supersolidity and crystallization of a dipolar Bose gas in an infinite tube.” In: *Phys. Rev. A* 107 (2023), p. 033301. DOI: `10.1103/PhysRevA.107.033301`.

[169] T. Speck et al. “Dynamical mean-field theory and weakly non-linear analysis for the phase separation of active Brownian particles.” In: *J. Chem. Phys.* 142 (2015), p. 224109. DOI: `10.1063/1.4922324`.

[170] T. Speck et al. “Effective Cahn-Hilliard equation for the phase separation of active brownian particles.” In: *Phys. Rev. Lett.* 111 (2014), p. 218304. DOI: `10.1103/PhysRevLett.112.218304`.

[171] A. B. Steinberg et al. “Exploring bifurcations in Bose-Einstein condensates via phase field crystal models.” In: *Chaos* 32 (2022), p. 113112. DOI: `10.1063/5.0101401`.

[172] A. B. Steinberg et al. *Localized States in Dipolar Bose-Einstein Condensates: To be or not to be of second order.* 2024. arXiv: `2407.09177`.

[173] S. Strogatz. *Nonlinear dynamics and chaos.* 2nd edition. Boca Raton; London; New York: CRC Press, Taylor & Francis Group, 2018. ISBN: 978-0-429-49256-3.

[174] P. Subramanian et al. “Spatially localized quasicrystalline structures.” In: *New J. Phys.* 20 (2018), p. 122002. DOI: `10.1088/1367-2630/aaf3bd`.

[175] T. H. Tan et al. “Odd dynamics of living chiral crystals.” In: *Nature* 607 (2022), pp. 287–293. DOI: `10.1038/s41586-022-04889-6`.

[176] L. Tanzi et al. “Evidence of superfluidity in a dipolar supersolid from non-classical rotational inertia.” In: *Science* 371 (2021), pp. 1162–1165. DOI: `10.1126/science.aba4309`.

[177] L. Tanzi et al. “Observation of a Dipolar Quantum Gas with Metastable Supersolid Properties.” In: *Phys. Rev. Lett.* 122 (2019), p. 130405. DOI: `10.1103/PhysRevLett.122.130405`.

[178] L. Tanzi et al. “Supersolid symmetry breaking from compressional oscillations in a dipolar quantum gas.” In: *Nature* 574 (2019), pp. 382–385. DOI: `10.1038/s41586-019-1568-6`.

[179] S. van Teeffelen et al. “Derivation of the phase-field-crystal model for colloidal solidification.” In: *Phys. Rev. E* 79 (2009), p. 051404. DOI: `10.1103/PhysRevE.79.051404`.

[180] I. Theurkauff et al. “Dynamic clustering in active colloidal suspensions with chemical signaling.” In: *Phys. Rev. Lett.* 108 (2012), p. 268303. DOI: `10.1103/PhysRevLett.108.268303`.

[181] U. Thiele et al. “First order phase transitions and the thermodynamic limit.” In: *New J. Phys.* 21 (2019), p. 123021. DOI: `10.1088/1367-2630/ab5caf`.

[182] U. Thiele et al. “Localized states in the conserved Swift-Hohenberg equation with cubic nonlinearity.” In: *Phys. Rev. E* 87 (2013), p. 042915. DOI: `10.1103/PhysRevE.87.042915`.

[183] J. Toner and Y. Tu. “Flocks, herds, and schools: A quantitative theory of flocking.” In: *Phys. Rev. E* 58 (1998), pp. 4828–4858. DOI: `10.1103/PhysRevE.58.4828`.

[184] A. M. Turing. “The Chemical Basis of Morphogenesis.” In: *Philos. Trans. R. Soc. Lond. Ser. B-Biol. Sci.* 23 (1952), p. 237.

[185] H. Uecker. *Numerical Continuation and Bifurcation in Nonlinear PDEs.* Philadelphia, PA: Society for Industrial and Applied Mathematics, 2021. DOI: `10.1137/1.9781611976618`.

[186] H. Uecker. *pde2path without finite elements.* URL: `https://www.staff.uni-oldenburg.de/hannes.uecker/pde2path/tuts/modtut.pdf`.

[187] T. Vicsek et al. “Novel Type of Phase Transition in a System of Self-Driven Particles.” In: *Phys. Rev. Lett.* 75 (1995), pp. 1226–1229. DOI: `10.1103/PhysRevLett.75.1226`.

[188] M. te Vrugt, H. Löwen, and R. Wittkowski. “Classical dynamical density functional theory: From fundamentals to applications.” In: *Adv. Phys.* 69 (2020), pp. 121–247. DOI: `10.1080/00018732.2020.1854965`.

[189] F. Wächtler and L. Santos. “Quantum filaments in dipolar Bose-Einstein condensates.” In: *Phys. Rev. A* 93 (2016), p. 061603. DOI: `10.1103/PhysRevA.93.061603`.

[190] Z.-L. Wang et al. “Minimal phase-field crystal modeling of vapor-liquid-solid coexistence and transitions.” In: *Phys. Rev. Mater.* 4 (2020), p. 103802. DOI: `10.1103/PhysRevMaterials.4.103802`.

[191] J. A. C. Weideman and B. M. Herbst. “Split-Step Methods for the Solution of the Nonlinear Schrödinger Equation.” In: *SIAM Journal on Numerical Analysis* 23 (1986), pp. 485–507. DOI: `10.1137/0723033`.

[192] A. T. Winfree. *The geometry of biological time.* 2. ed. Interdisciplinary applied mathematics 12. New York [u.a: Springer, 2001. ISBN: 0-387-98992-7.

[193] R. Wittkowski et al. "Scalar ϕ^4 field theory for active-particle phase separation." In: *Nat. Commun.* 5 (2014), p. 4351. DOI: `10.1038/ncomms5351`.

[194] P. D. Woods and A. R. Champneys. "Heteroclinic tangles and homoclinic snaking in the unfolding of a degenerate reversible Hamiltonian–Hopf bifurcation." In: *Phys. D Nonlinear Phenom.* 129 (1999), pp. 147–170. DOI: `10.1016/S0167-2789(98)00309-1`.

[195] J. Yan, S. C. Bae, and S. Granick. "Rotating crystals of magnetic Janus colloids." In: *Soft Matter* 11 (2015), pp. 147–153. DOI: `10.1039/C4SM01962H`.

[196] Y.-C. Zhang, F. Maucher, and T. Pohl. "Supersolidity around a Critical Point in Dipolar Bose-Einstein Condensates." In: *Phys. Rev. Lett.* 123 (2019), p. 015301. DOI: `10.1103/PhysRevLett.123.015301`.

[197] Y.-C. Zhang, T. Pohl, and F. Maucher. "Phases of supersolids in confined dipolar Bose-Einstein condensates." In: *Phys. Rev. A* 104 (2021), p. 013310. DOI: `10.1103/PhysRevA.104.013310`.

[198] L. Zhou. "Characteristics of Soft Matters." In: *Introduction to Soft Matter Physics.* 2019. Chap. Chapter 1, pp. 1–34. DOI: `10.1142/9789813275102_0001`.

[199] A. Zöttl and H. Stark. "Emergent behavior in active colloids." In: *J. Phys.: Condens. Matter* 28 (2016), p. 253001. DOI: `10.1088/0953-8984/28/25/253001`.

Danksagung

Zum Schluss möchte ich bei allen bedanken, die mir während meiner Promotion und beim Verfassen dieser Arbeit zur Seite standen.

Besonderer Dank gilt dabei:

- Prof. Dr. Uwe Thiele, für die entspannte Betreuung, gute Diskussionen mit neuen Perspektiven und hilfreiche Verbesserungsvorschläge
- Prof. Fabian Maucher, für die Zweitbetreuung, bei der er mir mit immer neuen Ideen und endlosem Enthusiasmus weiter geholfen hat
- Prof. Svetlana Gurevich, für weitere Betreuung, ein offenes Ohr und Hilfe bei allen Numerik Fragen
- meinen verbliebenen Korrekturlesern Daniel Greve, Tristan Schwenk, Michael Steinberg und Philip Sudhaus für konstruktive Kritik und Verbesserungsvorschläge
- Andrew Archer, Danielle Avitabile, Daniel Greve, Elias Koch, Jonas Mayer Martins, Tobias Frohoff-Hülsmann, Max Holl und Simon Hartmann für aufschlussreiche Gespräche rund um das GEM-4 Modell, Bifurkationen, Computerprobleme, Numerik, Bürogestaltung und vieles mehr
- allen Mitarbeitern der AGs Thiele und Gurevich für eine wunderbare Arbeitsatmosphäre und hilfreichen Austausch wann immer man es braucht
- meinen Großeltern, die unbedingt zum Drucken der Arbeit beisteuern wollten
- meiner Familie, meinen Freunden und ganz besonders meinen Eltern, die mir während meines Studiums und besonders während dieser Arbeit, den Rücken frei gehalten haben

Lebenslauf

Name	Alina Barbara Steinberg
Geburtsdatum	8.10.1992
Geburtsort	Bochum
Staatsangehörigkeit	deutsch

Schulausbildung

1999 - 2003	**Brunogrundschule**, Soest
2003 - 2012	**Aldegrevergymnasium**, Soest Abschluss: Allgemeine Hochschulreife, Note: 2,0

Studium

2012 - 2016	**Bachelor Physik** an der Technischen Universität Dortmund Abschluss: B.Sc., Note: 1,6
2016 - 2018	**Bachelor Grundschullehramt** an der Universität Münster
2018 - 2020	**Master Physik** an der Universität Münster Abschluss: M.Sc., Note: 1,1
seit 2020	**Promotion** am Institut für theoretische Physik der Universität Münster Unter der Betreuung von Prof. Dr. U. Thiele

Berufstätigkeit

seit 1.10.2020	**Wissenschaftliche Mitarbeiterin** am Institut für theoretische Physik der Universität Münster